Structure and Ferroelectric Properties of $BiFeO_3$-Based Thin Films

Author: Jingdan Yan

Supervisor: Prof. Manabu Gomi

Department of Materials Science and Engineering
Nagoya Institute of Technology, Japan
June 2013

Acknowledgements

I am very grateful for the international program between Nagoya Institute of Technology (NIT, Japan) and Beijing University of Chemical Technology (BUCT, China) funded by Japan MEXT, which gives me a chance to come to Japan. All what had happened during my period of staying in Japan would be wonderful memories.

I would like to extend my thanks to number of people who have contributed so much to my study at NIT. First of all, I would like to express my sincere gratitude to my supervisors Prof. Manabu Gomi. I have been in his lab for 5 years, from a master student to doctor student. He offers me the precious opportunity to conduct research in such an amazing field. My thesis is finished under his guidance and encouragement. His kindness impresses me a lot and his earnest in science greatly influences me which will benefit me in future.

Secondly, I would like to express my heartfelt gratitude to our assistant teacher Dr. Yokota. I get a lot benefit from his generous assistance and invaluable advice. And I sincerely thank Prof. Hayakawa, who gave comprehensive guidance on Raman spectra measurement. I also really appreciate Dr. Asaka, who taught me a lot in TEM and EDAX measurement. I feel grateful for Prof. Fukuda, who supported the analysis of XRD curves in time.

I sincerely thank Prof. Kakimoto, Prof. Hayakawa and Prof. Song for reviewing the doctor thesis and giving some very useful suggestions.

I would like to thank all the members in our lab, especially Mr. Matsuyama who is my tutor, and Mr. Hattori who helps me a lot in my experiment. They have been teaching me so much since the time when I came here. I really appreciate their selfless assistance. Moreover, I sincerely thank all my dear friends.

Last but not least, I would like to give my special appreciation to my beloved family, my parents and grandparents, for the education and edification they gave me during the past years. Finally, I want to dedicate this paper for my dear father in heaven.

Contents

Chapter 1

General Introduction 1

1.1 Introduction of $BiFeO_3$ 1

1.1.1 Introduction of structure and polarization 1

1.1.2 Phase transition of $BiFeO_3$ 4

1.2 Structure modified for $BiFeO_3$ 9

1.2.1 Major problems of $BiFeO_3$ 9

1.2.2 Solution 9

1.3 Bi*M*O_3 compound 10

1.4 Chemical solution deposition method 12

1.4.1 Introduction of film deposition process 12

1.4.2 Precursor solution 13

1.4.3 Film deposition 14

1.5 Object of this work 15

1.6 Synopsis of the dissertation 15

References 16

Chapter 2

Effect of Excess Bi on $BiFeO_3$ Structure and Ferroelectric Properties 24

2.1 Introduction 24

2.2 Experiment 25

2.2.1 Precursor solution 25

2.2.2 Film deposition 26

2.2.3 Measurement 26

2.3 Results and discussion 26

2.3.1 Structural and morphology properties 26

2.3.2 Electric properties 36

2.4 Conclusions 42

References 42

Chapter 3

$LaNiO_3$ Bottom Electrode and Its Influence on $BiFeO_3$ Structure and Electrical Properties 45

3.1 Introduction 45

3.2 Experiment 46

3.2.1 Fabrication of $LaNiO_3$ layer on glass 46

3.2.2 Deposition of $BiFeO_3$ on $LaNiO_3$/glass 46

3.2.3 Measurement 47

3.3 Results and discussion 47

3.3.1 Structure and morphology of $LaNiO_3$ bottom electrodes 47

3.3.2 Stoichiometric $BiFeO_3$ on $LaNiO_3$ bottom electrodes 49

3.3.3 $BiFeO_3$ with excess Bi on $LaNiO_3$ bottom electrodes 54

3.4 Conclusions 59

References 59

Chapter 4

Phase Transition and Electrical Properties of $BiFe_{1-x}Al_xO_3$ Thin Films.....61

4.1 Introduction 61

4.2 Experiment 62

4.2.1 Precursor solution 62

4.2.2 Films deposition 63

4.2.3 Measurement 63

4.3 Results and Discussion 64

4.3.1 Phase transition of $BiFe_{1-x}Al_xO_3$ films 64

4.3.2 Structure and morphology of $BFe_{1-x}Al_xO_3$/$LaNiO_3$/glass 73

4.3.3 Electrical properties of BFAO thin films 77

4.4 Conclusions 83

References 84

Chapter 5

Phase Transition and Electrical Properties of $BiFe_{1-x}Ga_xO_3$ Thin Films 87

5.1 Introduction 87

5.2 Experiment 88

5.2.1 Precursor solution 88
5.2.2 Film deposition 88
5.2.3 Measurement 88
5.3 Results and discussion 89
5.3.1 Structure and phase transition of $BiFe_{1-x}Ga_xO_3$ films 89
5.3.2 Structure and ferroelectric properties of BFGO/LNO 95
5.4 Conclusions 105
References 105

Chapter 6
Conclusions 107

Symbol List 109

Publications 110

Academic Conferences 110

Chapter 1

General Introduction

During the past few years, an important interest has raised towards multiferroic materials. Multiferroics are compounds in which several ferroic orders coexist and can be simultaneously ferro-or antiferroelectric as well as ferro-or antiferromagnetic (AF). This multifunctional character may open the way toward other applications in storage media and represent a viable approach to the design of logic architectures. [1-3]

However, the choice of multiferroic from natural seems very limited, since hardly any material exhibits the coexistence of ferroelectric and ferromagnetic properties at room temperature, except $BiFeO_3$. [4]

1.1 Introduction of $BiFeO_3$

1.1.1 Introduction of structure and polarization

$BiFeO_3$ (BFO) is perhaps the only material that is both magnetic and a strong ferroelectric at room temperature. [5] The recorded FE (ferroelectric) Curie temperature for BFO is 1043 K[6], and the AFM (anti-ferromagnetic) Neel temperature is 647 K[7]. $BiFeO_3$ is usually prepared from equal parts of Bi_2O_3 and Fe_2O_3, the phase diagram for the system Bi_2O_3/Fe_2O_3 has been mapped out and is shown in Figure 1.1. [5, 8] There are many other phases in this phase diagram of $BiFeO_3$, such as Bi_2O_3, $Bi_{25}FeO_{39}$ and $Bi_2Fe_4O_9$, which makes it difficult to get pure phase BFO.

$BiFeO_3$ is a typical perovskite compound. The sketch of perovskite structure is shown in Figure 1.2. The structure contains two cation sites in the crystal lattice: the

larger cation A (Bi in BFO) resides on the corners of the unit cell, and the smaller cation B (Fe in BFO) is in the center of the unit cell. The oxygen ions (O) are on the centers of the faces, and the structure is formed via a network of corner-linked oxygen octahedra, with the larger cation (A) filling the dodecahedral holes and the smaller cation (B) filling the octahedral sites. [9]

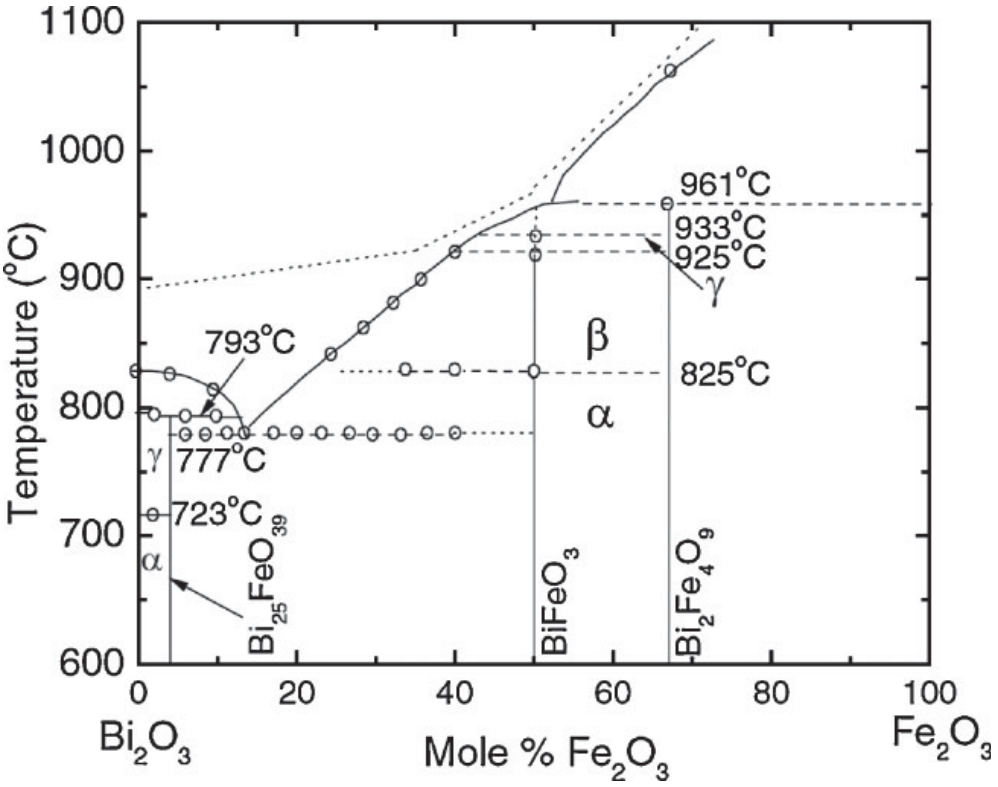

Figure 1.1 Compositional phase diagram of $BiFeO_3$. [8]

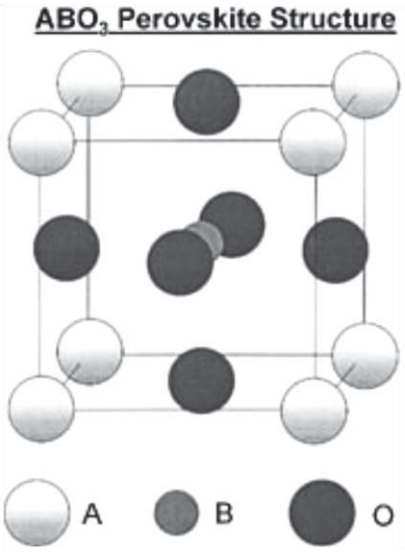

Figure 1.2 Crystal structure for the ABO_3 perovskite. [9]

Bulk single crystal BFO show a rhombohedrally distorted perovskite structure with space group *R*3*c* (*a*=3.96 Å and *α*=89.4º) at room temperature. [10, 11] *R*3*c* is the ground state for BFO [12] (Figure 1.3(a)), while there are many other structure symmetries can be obtained, depending on production process. Tetragonal phase (Figure 1.3(b)) shows an extremely high *c/a* ratio (1.2-1.3), while it is the most widely investigated BFO structure due to the outstanding ferroelectric behaviors.

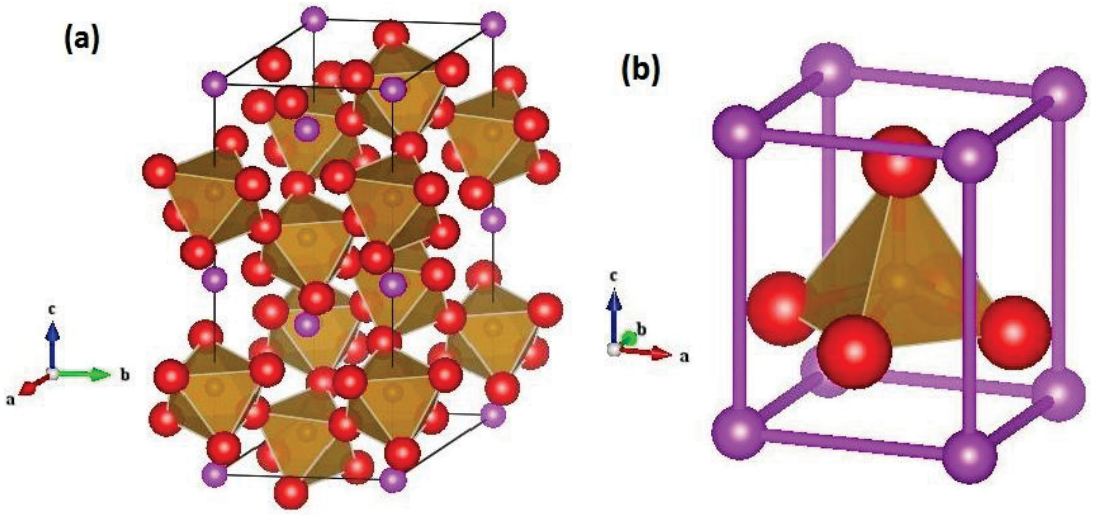

Figure 1.3 Crystal structure for the **(a)** rhombohedral BFO and **(b)** tetragonal BFO.

The presence of multiferroic property in $BiFeO_3$ can be simply described by its crystal structure. The polarization is mostly caused by the stereochemically active lone pair (s^2 orbital) of Bi^{3+}, while the magnetization mostly comes from Fe^{3+}. It is a perovskite with A-site ferroelectricity and B-site magnetism. [5]

From first-principles density functional calculations, the most natural value of the polarization for rhombohedral BFO is 90-100 μC cm^{-2} along the [111] direction [12], while tetragonal BFO (*P*4*mm*) which keeps a giant axial ratio (*a*=3.67 Å, *c*=4.65 Å and *c/a*=1.27) is predicted a large polarization (151 μC cm^{-2}) [13, 14]. But the polarization actually measured in a bulk single crystal BFO was only 3.5 μC cm^{-2} and 6.1 μC cm^{-2} along the (001) and (111) axis, respectively. [15] In 2003, Wang *et al*.[16] reported the tetragonal film on $SrTiO_3$ substrate showed huge P_r value of 50-60 μC cm^{-2}, which was one order of magnitude higher than that of bulk BFO. They pointed that strain effect was one of the reasons that there was a large difference between properties of bulk and thin film $BiFeO_3$. Then most of researches focused on the high quality BFO thin films, prepared by pulse laser deposition (PLD), sputtering,

and so on. Some of the reported data are listed in Table 1.1.

Table 1.1 Various measured values for the polarization of $BiFeO_3$ thin films

First Author	Preparation	Structure symmetry	P_r ($\mu C\ cm^{-2}$)	E_c ($kV\ cm^{-1}$)
Wang [16]	PLD	Epitaxial (001), tetragonal	60	200
Shuai [18]	PLD	Rhombohedral	65	250
Ricinschi [19]	PLD	Oriented (001), tetragonal	131 (90K)	180
Li [17]	PLD	(001), monoclinic	55	-
		(110), monoclinic	80	-
		(111), rhombohedral	100	-
Wu [20]	Rf-sputtering	*R*3*c*	49	400
Singh [21]	CSD	Oriented (001), rhombohedral	50 (80K)	100
Hong [22]	Sol-gel	Polycrystalline, *R*3*m*	0.418	21
Wang [23]	Sol-gel	*R3m*	0.69	100

The polarization results from Li *et al.*[17] were consistent well with calculated values. But it can be noticed that the P_r value is spread by changing preparation method, substrate, and so on. Furthermore, some of the BFO samples don't show saturated hysteresis loop, which is imputed to the leakage current generally.

1.1.2 Phase transition of $BiFeO_3$

Recently, there are many researches focus on the phase transition of BFO, from rhombohedral to monoclinic or tetragonal or further orthorhombic. For bulk BFO, in Figure 1.4 [5], the transition is under high pressure and/or high temperature. The ground state is rhombohedral, which turns to orthorhombic at higher temperature. The transition at 370 ºC, reported by Polomska [24], is caused by magnetoelectric coupling to the antiferromagnetic Neel temperature. It is possible that the phase transition reported at 458 K and ambient pressure could be the same as that observed at room temperature and ca. 4 GPa. With increasing temperature, there are orthorhombic-cubic transition and finally, the decomposition.

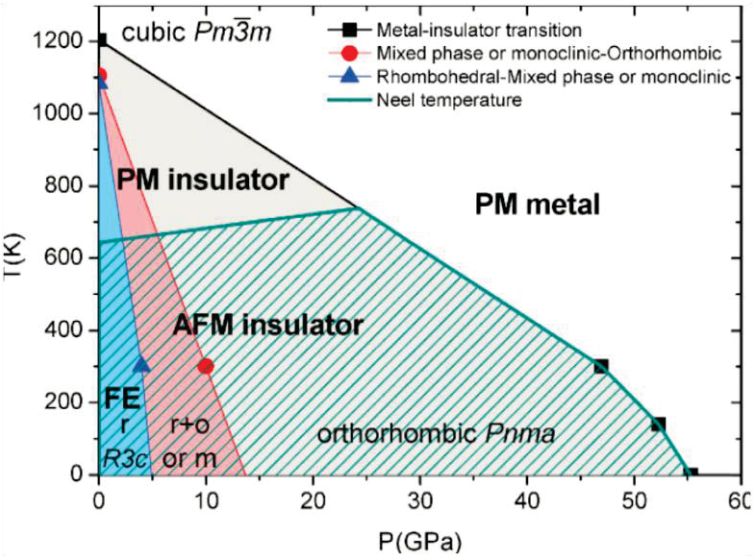

Figure 1.4 Sketch of possible phase diagram as function of pressure and temperature. [5]

While for film BFO, strain which is an alternative way of inducing ‘‘pressure’’ in crystal, plays an important role in the transition of structure symmetry.[25-28] As shown in Figure 1.5 [26], phase transition carries out with increment of misfit strain. The appearance of “*aa* phase” results from the positive misfit (i.e. tensile stress), while the “*c* phase” results from the negative misfit strain (i.e. compressive stress).

Moreover, there is another kind of pressure considered contributing for phase transition, as called “chemical pressure”, arisen from chemical substitution. [5]

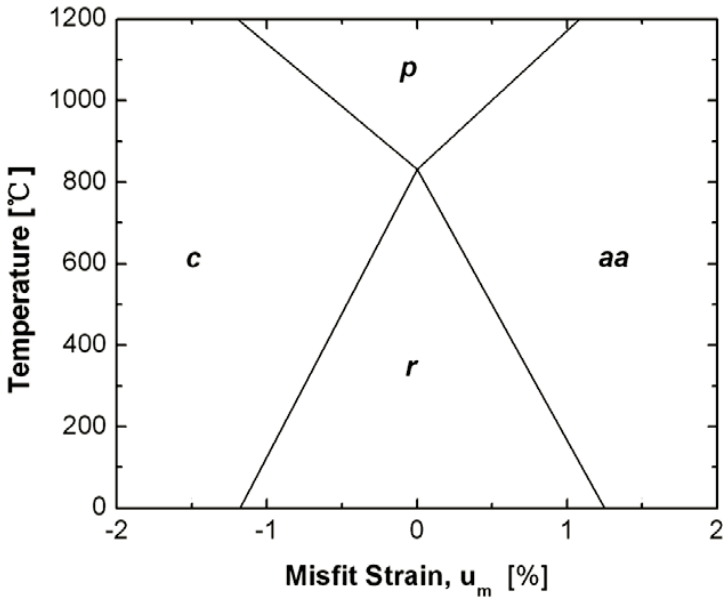

Figure 1.5 Misfit-temperature phase diagram of (001) single domain BFO thin film grown on the cubic substrate.[26]

Chaigneau et al. [29] reported the phase transition in $Bi_{1-x}Pb_xFeO_3$ system. In Figure 1.6, with increasing Pb concentration, the structure becomes cubic from rhombohedral. It is reported that addition of x in $Bi_{1-x}Pb_xFeO_3$ progressively breaks the ferroelectric ordering up to the point where the structure becomes cubic on average. The decreasing of *Tc* with increasing Pb content also confirms that adding of Pb atoms destabilizes the ferroelectric rhombohedral order and stabilizes the cubic phase via a complex texture of mixed phases. In the light of the literature, they suggest that this mechanism can be generalized to other (Bi*A*)FeO_3 solid solutions (*A*=Sr, La, Ca, Ba,…). With increasing *A* content, the rhombohedral $BiFeO_3$ distortion decreases up to reach a pseudocubic cell.[30-32]

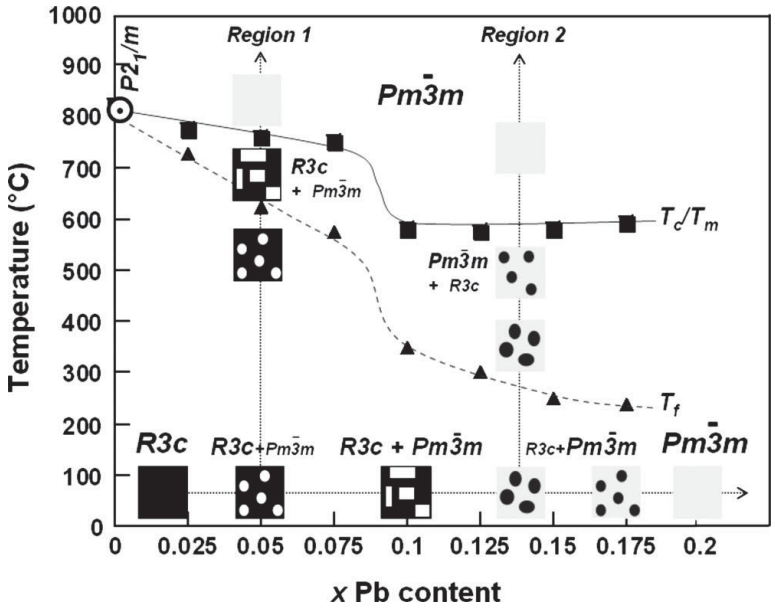

Figure 1.6 Phases diagram of $Bi_{1-x}Pb_xFeO_3$. [29]

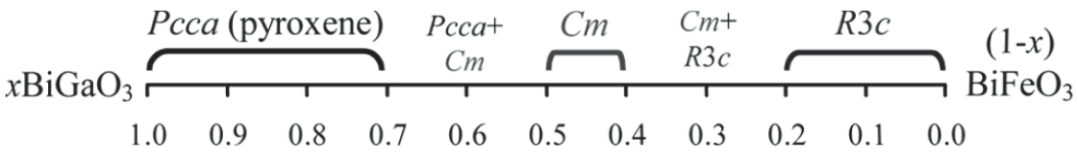

Figure 1.7 Schematic phase diagrams of the $BiGa_xFe_{1-x}O_3$

Belik et al. [33] reported the phase transition of "*R*3*c* to *Cm* to *Pcca*" in $BiFe_{1-x}Ga_xO_3$ system (Figure 1.7) under high-temperature and high-pressure, which can be considered as B-site substitution for BFO. The (almost pure) *R*3*c* phase was

found at $0 \leq x \leq 0.2$; the *Cm* phase at $0.4 \leq x \leq 0.5$, and the pyroxene phase at $0.7 \leq x \leq 1$. $BiGa_{0.3}Fe_{0.7}O_3$ was a mixture of the *Cm* phase (~85%) and the *R*3*c* phase (~15%). $BiGa_{0.6}Fe_{0.4}O_3$ was a mixture of the pyroxene phase (~75%) and the *Cm* phase (~25%). Application of moderate pressure stabilizes perovskite-type modifications of $BiGaO_3$, and the first perovskite phase of $BiGaO_3$ has the *Cm* symmetry.[34]

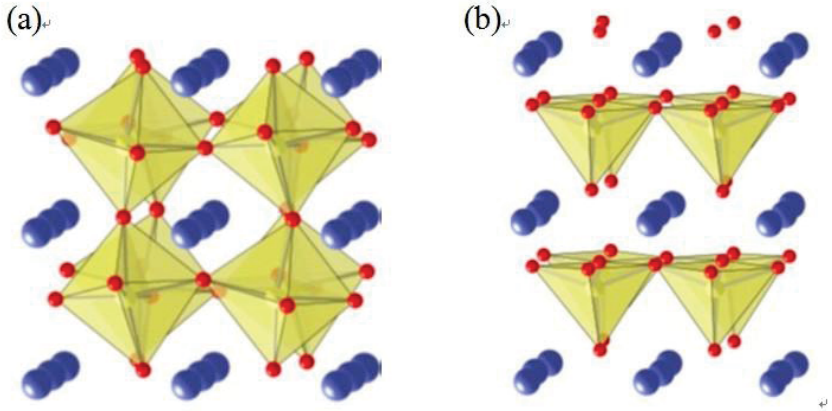

Figure 1.8 Symmetric phases of monoclinic BFO, **(a)** rhombohedral-like phase; **(b)** tetragonal-like phase.[38]

Monoclinic phase represents the nearly vertical limit between the rhombohedral and the tetragonal phases (Figure 1.8). Previous first-principles calculation found the monoclinic structure to be the ground state for *T*-like $BiFeO_3$. [35] Three types of ferroelectric monoclinic phases are known, namely, M_A, M_B and M_C. The M_A and M_B belong to the space group *Cm* while the M_C belongs to *Pm*. For the M_A/M_B phases, the unit cell is double and rotated by 45 º about the *c* axis with respect to the pseudocubic cell and the polarization is confined to the $(1\bar{1}0)$ plane. The M_A and M_B unit cells are similar but their magnitudes of the polarization components in the three axes directions corresponding to the pseudocubic unit cell are different. For the M_C phase, the polarization is constrained to lie within the (010) plane. [13] The standard notation [36] are used to distinguish these three monoclinic cases based on the orientation of *P* with respect to the pseudocubic coordinates: M_A and M_B for $P\|[uuv]_{pc}$, with $u<v$ and $u>v$, respectively; and M_C for $P\|[u0v]$pc. The tetragonal (*T*), rhombohedral (*R*), and orthorhombic (*O*) phases correspond to a constraint of *P* to a symmetry axis along $[001]_{pc}$, $[111]_{pc}$, or $[011]_{pc}$, respectively; see Figure 1.9.[28] For instance, BFO films grown on low misfit substrates reportedly adopt a monoclinic

structure of the M_A phase for compressive strain and the M_B phase for tensile strain (space group *Cm* or *Cc*, depending on whether the oxygen octahdra rotations are suppressed by the substrate or not, respectively).[37-40] It is reported that the stress-induced phase transitions in $BiFeO_3$ follow the path of rhombohedral to monoclinic to tetragonal.[28]

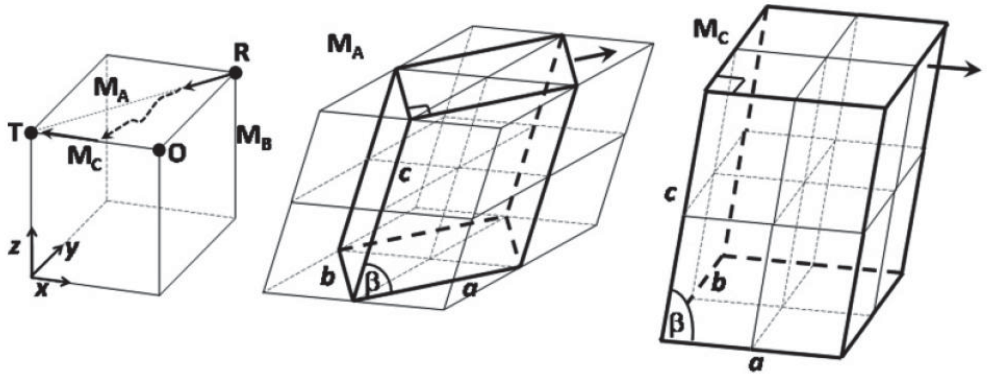

Figure 1.9 Schematic comparison of monoclinic structures. Polarization direction in differently distorted perovskite structures: The polarization points in a direction parallel to that connecting the origin with the indicated dots for *R*, *O*, and *T*, or with any point on the lines labeled M_A, M_B, and M_C. The path *R*-M_A-M_C-*T* observed here and in relaxer ferroelectrics is indicated by arrows.

In the group of the lead-based perovskites, such as PZT, PZN-PT, and PMN-PT, the existence of such a monoclinic phase, which is stability limited around a narrow region near morphotropic phase boundary (MPB), is crucial in explaining the outstanding properties of these materials. [41-43] The large piezoelectric response around MPB is driven by the electric-field induced rotation of the electrical polarization *P*, supported by theoretical [44] and experimental [45] studies. For example, applying an electric field along the pseudocubic [001] direction in rhombohedral PZN-PT induces a rotation of the polarization occurring along the rhombohedral-tetragonal path (i. e., *P* continuously rotates from the [111] to [001] direction), and a large piezoelectric response can result from such a path switch. [46]

However, there is few reported about the practical and technological implications of phase coexistence and morphotropic phase boundary like behavior in BFO system. Moreover, the mechanism of the chemical substitution induced phase transition is still an open question.

1.2 Structure modified for $BiFeO_3$

1.2.1 Major problems of $BiFeO_3$

In the earlier years of BFO's birth, it failed to make any remarkable impact on electronic industries due to problem of leakage current. The main reason is that the BFO synthesized by even established methods are generally plagued by impure phases. [47] In its bulk form, measurements of the ferroelectric and transport properties in BFO have been limited by the problem of leakage, mainly due to low resistivity [10], lattice defects and nonstoichiometry.

Recently, advanced thin film preparation technologies make it is possible to obtain high quality thin film $BiFeO_3$, without impurity phase detected. However, there is an instinct fact that the electronegativity of Bi (2.02) is larger than that of Fe (1.83), where the electronegativity is 3.44 for O. According to the Pauling electronegativity theory, the higher the difference of electronegativity between two elements is, the stronger the bond energy is. Accordingly, the bond energy of Fe-O is stronger than that of Bi-O. [48] The evaporable Bi is easily lost during process of vacuum or heat treatment, resulting in vacancy-defects.

On the other hand, the valence of Fe is variable that both Fe^{2+} and Fe^{3+} occupy the octahedral site in perovskite structure. The octahedrons are connected by vertices, so that there is one O^{2-} between Fe^{2+} and Fe^{3+}, which blocks the direct hopping of electrons from Fe^{2+} to Fe^{3+}. Nevertheless, the hopping of electrons becomes possible in these materials when oxygen vacancies are present, which act as "bridge" between Fe^{2+} and Fe^{3+}. The oxygen vacancies carrying positive charge attract electrons from Fe^{2+}, but they are not effective electron traps even at room temperature, so electrons can easily escape from the oxygen vacancies traps and hop to Fe^{3+}. Based on this consideration, it is reasonable to believe that the hopping of electrons from Fe^{2+} to Fe^{3+} plays an important role in the electronic conduction. [49]

1.2.2 Solution

The theoretical feasible way to reduce leakage current is to control the formation of vacancies and/or prevent the Fe^{2+}. It is well known that many physical properties of materials may vary significantly with a small change of chemical composition

through doping or substitution of impurities. The chemical substitution for BFO has been widely investigated to deal with the major problems of BFO.

Bi site doping with La, Nd, Sm or Ce atoms have been attempted in suppressing the generation of oxygen vacancies during the preparation process of BFO film by controlling the volatilization of Bi. [50-53] And Fe-site doping with Cr, Mn or Ti atoms has been documented of successfully reducing the formation of Fe^{2+}. [54-57] To further improve the ferroelectricity of BFO films, co-substitution strategy has been adopted. [22] Some reported experimental results for leakage current and polarization properties of doped BFO are shown in Table 1.2. The leakage current of BFO thin films can be significantly reduced by 1-3 orders of magnitude via chemical substitution. [18]

Table 1.2 Various measured values for the electric properties of doped-$BiFeO_3$

First Author	Compound	Leakage at 100 kV cm^{-1} (A cm^{-2})	P_r (μC cm^{-2})	E_c (kV cm^{-1})
Singh [58]	$BiFe_{0.5}Cr_{0.5}O_3$	10^{-7}	30	370
Wu [59]	$BiFe_{0.95}Mn_{0.05}O_3$/ $BiFe_{0.95}Zn_{0.05}O_3$	10^{-7}	80	350
Hong[22]	$BiFe_{0.95}Ti_{0.05}O_3$	10^{-7}	3.948	181
Chishima[60]	$BiFe_{0.996}Zn_{0.001}Mn_{0.003}O_3$	10^{-7}	40	25
Kim [54]	$BiFe_{0.97}Cr_{0.03}O_3$	9.2×10^{-7}	61	290

1.3 Bi*M*O_3 compound

A number of strategies have been proposed to prepare noncentrosymmetric materials, for example, utilizing cations with a lone pair of electrons, such as Bi^{3+} and Pb^{2+} usually have asymmetric coordination environments. Bi- and Pb-based perovskite have received renewal attention in recent years due to the great interest in multiferroic materials. Bi-based materials are considered as good alternatives to Pb-based system, due to the similar ion off-centering reduced ferroelectric polarization, and nontoxic of Bi-based oxide. [61, 62]

In Bi-based system, $BiMnO_3$ and $BiFeO_3$ are multiferroic. Moreover, there are

group of BiMO$_3$ with nonmagnetic ions (M=Al, Sc, Ga and In). BiAlO$_3$ crystallizes in a noncentrosymmetric structure and is isotypic with the well-known BiFeO$_3$. [63] BiScO$_3$ crystallizes in centrosymmetric structure. [64] BiGaO$_3$ has a centrosymmetric pyroxene-type structure, [33, 63] while BiInO$_3$ has orthorhombically distorted GdFeO$_3$-type structure. [61]

The stability and distortions of perovskite-type oxides (ABO$_3$) can be qualified using the tolerance factor:

$$t = \frac{r_A + r_O}{\sqrt{2}(r_B + r_O)} \quad (1.1)$$

where r_A, r_B and r_O are the ionic radii of the A, B, and oxygen ions, respectively. [65, 66] For A-site driven ferroelectricity, the ferroelectric distortions of the perovskite are mainly described as a shift of the A-site cation with respect to the surrounding oxygen ions with smaller accompanying shifts of the B-site ions. We use the r values of six-fold coordination, and the stability of the perovskite structure is expected within the limits $0.77 < t < 0.99$ in this case. For BFO (r_{Bi}=1.03Å, r_{Fe}= 0.645Å, and r_O=1.4Å [67]), t=0.84, located in the stability region. The BiAlO$_3$ with t=0.888 shows larger ferroelectric distortion. While BiInO$_3$ with t=0.78 suggest rotational instability.

From the equation of tolerance factor, it is easy to find that smaller B-site ions are helpful to enhance ferroelectric distortion. Under the case of six-fold coordination, the ionic radii for Al, Ga, Sc and In are 0.535, 0.62, 0.745 and 0.8 Å, [67] respectively, while that of Fe is 0.645 Å. The theoretical studies give some evidences for the relationship between B-site ions and ferroelectric properties. From first principle calculation, the ferroelectric polarization for BiAlO$_3$ should be 75.6 μC cm^{-2} along [111] direction, and BiGaO$_3$ is 151.9 μC cm^{-2} along the [100] direction. They are predicted to be high-performance ferroelectrics. [68] While for BiInO$_3$, the calculated spontaneous polarization is as small as 18 μC cm^{-2}. [61] It means that not only the stereochemically active 6s^2 lone pair electrons of Bi^{3+} but also the M-ion displacement can affect the polarization behavior in BiMO$_3$ compounds. Study from Zhang *et al*. [69] supported this opinion. They found that the Fe-O off-centering in the T phase contributed to the large ferroelectric polarization in the T-phase BiFeO$_3$.

However, there are few reports on BiMO$_3$ compounds, perhaps due to the extreme productive condition, such as high-temperature (>1000 ºC) and high-temperature (~6

GPa). [70] As introduced in section 1.2.2 that B-site substitution in $BiFeO_3$ is generally carried out to deal with leakage current. But there is no study focus on the relationship between B-site substitution induced structure distortion and ferroelectric properties. It is reasonable to expect that the B-site substitution will bring some interesting changes into $BiFeO_3$ structure and further influence the ferroelectric properties.

1.4 Chemical solution deposition method

1.4.1 Introduction of film deposition process

The deposition process plays an important role in determining the crystal structure of BFO thin films, which in further influence ferroelectric properties of BFO. [21]

Pulsed laser deposition (PLD) is a widely used technique for the preparation of complicated oxide thin films. It is reported that thin films prepared by PLD keep high quality and excellent properties. However, for pure BFO, it was reported that the ambient (oxygen) pressure and substrate temperature should be addressed, in order to obtain pure perovskite phase. [71] Moreover, excess Bi is needed to prevent Bi deficiency due to the volatility of Bi, which makes it difficult to control chemical composition. Thus an optimization of the deposition conditions is extremely important. Molecular-beam epitaxy (MBE) method is another way to deposit BFO films. Comparing with PLD, the growth condition of MBE is more convenient to be controlled, due to the Bi partial pressure can be set independently. [72] Besides these, metal organic chemical vapor deposition (MOCVD) [73], magnetron sputtering [74], and RF-sputtering [75] were also used to prepare BFO thin films. However, these methods are carried out under vacuum condition and greatly depended on instrument, which is disadvantageous for real device application.

From mid 1980s, chemical solution deposition (CSD) for preparing perovskite thin films has been investigated. [76] CSD has an advantage in exact control of stoichiometry composition. Meanwhile, it is particularly important from an industrial aspect because of its suitability for large-area deposition and mass production. [21]

The general principle involved in the solution deposition of films is to prepare a “homogeneous” solution of the necessary cation species that may later be coated to a

substrate. The fabrication of thin films by this approach involves four basic steps: (1) synthesis of the precursor solution; (2) deposition by spin-coating or dip-coating, where drying processes usually begin depending on the solvent, (3) low-temperature heat treatment for drying, pyrolysis of organic species (typically 300-400 ºC), and formation of an amorphous film; (4) higher temperature heat treatment for densification and crystallization of the coating into the desired oxide phase. [9, 77]

1.4.2 Precursor solution

Solution preparation generally involves the use of metal organic compounds that are dissolved in the common solvent. The most frequently used CSD approaches can be grouped into three categories: (1) Sol-gel processes that use 2-methoxyethanol as a reactant and solvent. (2) Chelate processes that use modifying ligands, such as acetic acid. [78, 79] (3) Metal organic decomposition (MOD) routes that use water insensitive metal carboxylate compounds. Among these routes, chelate process is relative simple, as the distillation and refluxing strategies are not required with comparison with sol-gel method. Besides some acceptable disadvantages, such as the complex composition in prepared solution due to continued reactivity, a number of research groups routinely use it as their primary method of film fabrication.

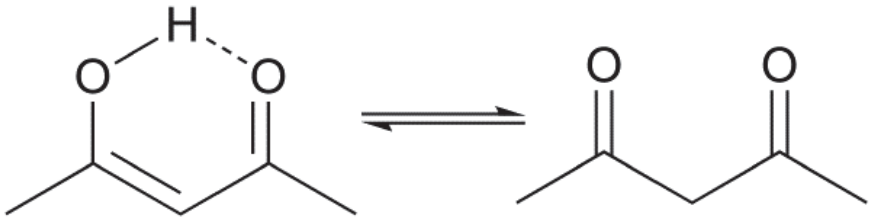

Figure 1.10 Tautomerism of 2, 4-pentanedione.

The chelate process relies heavily on the molecular modification of the alkoxide compounds through reactions with other reagents, namely chelating ligand, such as acetic acid, acetylacetone, or amine compounds. The molecular structure of acetylacetone is shown in Figure 1.10. Acetylacetone is an organic compound with molecular formula $C_5H_8O_2$. This diketone is formally named 2, 4-pentanedione. It is a precursor to acetylacetonate (acac), a common bidentate ligand. It is also a building

block for the synthesis of heterocyclic compounds. The structure sketch for chelate compounds by using acac as chelating ligand is shown in Figure 1.11. [80] The small oligomeric species will form during solution synthesis.

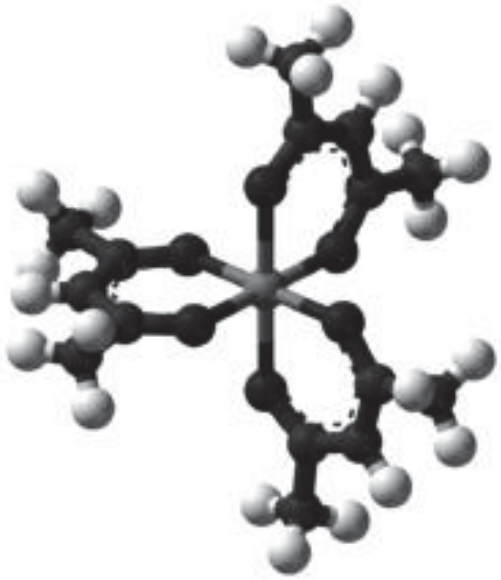

Figure 1.11 Atomic structure of $M(C_5H_7O_2)_3$ (M=Bi, Fe, Al, Ga *et al*.)

1.4.3 Film deposition

To optimize film properties for specific applications, the structural evolution of the as-deposited film to the crystalline ceramic state is important. In the deposition process, the oligomeric solution precursor species containing an organic fraction is converted to the desired crystalline ceramic. For example, for crystallization to occur, M-O-C (or M-O-H) bonds must be broken and M-O-M bonds are formed. Some of the processes involved in the transformation are (1) continued condensation reactions, (2) organic pyrolysis and concomitant M-O-M bond formation, (3) elimination of structural free volume through relaxation, and (4) crystallization. To control the properties of the final ceramic film, an understanding of the thermodynamics and kinetics of the processes is required. Generally, the film is heated rapidly to the crystallization temperature, which results in the formation of crystalline phase. Rapid thermal heat treatment has the potential advantage of being an “isothermal” process, making simple route and effectively balances the competing kinetics which is arisen

from various processes that take place during the conventional transformation.

1.5 Object of this work

In this study, we focus on the structure and electrical properties of $BiFeO_3$-based thin films, where chemical solution deposition method is chosen as preparation method. The main object of this work is as below.

(1) In most of studies on $BiFeO_3$, Bi is overdosed to compensate Bi-evaporation. The changes of ferroelectric behavior are conventionally attributed to excess Bi, lacking the detailed discussion on why overdosed Bi influences the structure and properties of the $BiFeO_3$ films. Thus we would like to search the optimal route to crystallize pure $BiFeO_3$ thin films by CSD method. Via doping excess Bi, find the relationship among defects, strain, structure distortion and electric properties. These results will offer better understanding of the contribution of excess Bi on properties of $BiFeO_3$.

(2) For thin films, strain from substrate plays an important role in crystal structure. For further ferroelectric measurement, the electrode is also important. In our study, $LaNiO_3$ is chosen as bottom electrode. We would like to discuss the influence of $LaNiO_3$ electrode on the structure and electrical properties of top $BiFeO_3$ films. By simply altering annealing temperature to control structure of $LaNiO_3$ layers, which are able to provide support for ferroelectric properties of top $BiFeO_3$ films.

(3) Considering that the physical properties of materials may vary significantly with a small change of chemical composition through doping or substitution, substitution on Fe-site by Al or Ga are carried out. Al and Ga keep smaller ionic radii than Fe, which is considered to enlarge tolerance factor after doping. The point for substitution is to alter the Fe environment, which plays an important role in electric conduction and polarization. Via systematic studies on $BiFe_{1-x}Al_xO_3$ (BFAO) and $BiFe_{1-x}Ga_xO_3$ (BFGO) systems, to get information of phase transition and variation of electrical properties arising from substitution.

1.6 Synopsis of the dissertation

Chapter 1 introduces the basic performance of $BiFeO_3$, focusing on various phases

and structure modification. Chemical solution deposition (CSD) process is described and chosen as film fabricated method in our study.

Chapter 2 presents the effect of excess Bi on $BiFeO_3$ structure and ferroelectric properties. The overdosed Bi takes influence on in-plane stress and further effects electric behavior.

Chapter 3 describes the role of $LaNiO_3$ bottom layers on contribution of electric properties of top $BiFeO_3$ films. Excellent polarization properties can be obtained by improving quality of $LaNiO_3$ bottom layers.

Chapter 4 presents a systematic study on Al doped $BiFeO_3$ thin films. The rough phase diagram of $BiFe_{1-x}Al_xO_3$ is obtained based on various annealing temperatures. Polarization property is found to be enhanced around morphotropic phase boundary (MPB). It offers new understandings about the relationship between structural instability, symmetry and ferroelectric properties

Chapter 5 describes the research on Ga doped $BiFeO_3$ thin films. The stable monoclinic phase is obtained in $BiFe_{1-x}Ga_xO_3$ system. The polarization value of 230 $\mu C\ cm^{-2}$ is detected around MPB.

Chapter 6 is the overall discussion and conclusions. The effect factors for ferroelectric properties are discussed, including both of stress induced strain and B-site displacement.

References

[1] M. Gajek, M. Bibes, F. Wyczisk, M. Varela, J. Fontcuberta, and A. Barthelemy. Growth and magnetic properties of multiferroic $La_xBi_{1-x}MnO_3$ thin films. Phys. Rev. B 75, 174417 (2007).

[2] N. Hur, S. Park, P. A. Sharma, J. S. Ahn, S. Guha, and S. W. Cheong. Electric polarization reversal and memory in a multiferroic material induced by magnetic fields. Nature 429, 392-395 (2004).

[3] T. Kimura, S. Kawamoto, I. Yamada, M. Azuma, M. Takano, and Y. Tokura. Magnetocapacitance effect in multiferroic $BiMnO_3$. Phys. Rev. B 67, 180401 (2003).

[4] F. Gao, X. Qiu, Y. Yuan, B. Xu, Y. Wen, F. Yuan, L. Lv, and J. Liu. Effects of substrate temperature on $Bi_{0.8}La_{0.2}FeO_3$ thin films prepared by pulsed laser deposition. Thin Solid Films 515, 5366-5373 (2007).

[5] G. Catalan and J. F. Scott. Physics and applications of bismuth ferrite. Adv. Mater. 21, 2463-2485 (2009).

[6] G. Smolenskii, V. Isupov, A. Agranovskaya, and N. Krainik. New ferroelectrics of complex composition. Sov. Phys.-Solid State 2, 2651-2654 (1961).

[7] P. Fischer, M. Polomska, I. Sosnowska, and M. Szymanksi. Temperature dependence of the crystal and magnetic structure of $BiFeO_3$. J. Phys. C 13, 1931-1940 (1980).

[8] R. Palai, R. S. Katiyar, H. Schmid, P. Tissot, S. J. Clark, J. Robertson, S. A. T. Redfern, G. Catalan, and J. F. Scott. B phase and γ-β metal-insulator transition in multiferroic $BiFeO_3$. Phys. Rev. B 77, 014110 (2008).

[9] R. W. Schwartz. Chemial solution deposition of perovskite thin films. Chem. Mater. 9, 2325-2340 (1997).

[10] H. Liu and X. Wang. Study on the Ce substitution effects of $BiFeO_3$ films prepared by a sol-gel process. Solid State Commun. 148, 203-205 (2008).

[11] F. Jubel and H. Schmid. Structure of a ferroelectric and ferroelastic monodomain crystal of the perovskite $BiFeO_3$. Acta. Cryst. 466, 698-792 (1990).

[12] J. B. Neaton, C. Ederer, U. V. Waghmare, N. A. Spaldin, and K. M. Rabe. First-principles study of spontaneous polarization in multiferroic $BiFeO_3$. Phys. Rev. B 71, 014113 (2005).

[13] Z. Chen, Z. Luo, C. Huang, Y. Qi, P. Yang, L. You, C. Hu, T. Wu, J. Wang, C. Gao, T. Sritharan, and L. Chen. Low-symmetry monoclinic phases and polarization rotation path mediated by epitaxial strain in multiferroic $BiFeO_3$ thin films. Adv. Funct. Mater. 21, 133 (2011).

[14] C. Ederer and N. A. Spaldin. Effect of epitaxial strain on the spontaneous polarization of thin films ferroelectrics. Phys. Rev. Lett. 95, 257602 (2005).

[15] J. R. Teague, R. Gerson, and W. J. James. Dielectric hysteresis in single crystal $BiFeO_3$. Solid State Commun. 8, 1073-1073 (1970).

[16] J. Wang, J. B. Neaton, H. Zheng, V. Nagarajan, S. B. Ogale, B. Liu, D. Viehland, V. Vaithyanathan, D. G. Schlom, U. V. Waghmare, N. A. Spaldin, K. M. Rabe, M. Wuttig, and R. Ramesh. Epitaxial $BiFeO_3$ multiferroic thin film heterostructres. Science 299, 1719-1722 (2003).

[17] J. Li, J. Wang, M. Wuttig, R. Ramesh, N. Wang, B. Ruette, A. P. Pyatakov, A. K. Zvezdin, and D. Viehland. Bramatically enhanced polarization in (001), (101), and

(111) $BiFeO_3$ thin films due to epitiaxial-induced transitions. Appl. Phys. Lett. 84, 5261 (2004).

[18] Y. Shuai, S. Zhou, S. Streit, H. Reuther, and D. Burger. Reduced leakage current in $BiFeO_3$ thin films with rectifying contacts. Appl. Phys. Lett. 98, 232901 (2011).

[19] D. Ricinschi, K. Yuan, and M. Okuyama. A mechanism for the 150 μC cm^{-2} polarization of $BiFeO_3$ films based on first-principles calculations and new structural data. J. Phys.:Condens. Matter 18, L97-L105 (2006).

[20] J. Wu and J. Wang. Mutiferroic behavior and electrical conduction of $BiFeO_3$ thin film deposited on quartz substrate. J. Alloys Compd. 507, L4-L7 (2010).

[21] S. Singh, Y. Kim, H. Funakubo, and H. Ishiwara. Epitaxial $BiFeO_3$ thin films fabricated by chemical solution deposition. Appl. Phys. Lett. 88, 162904 (2006).

[22] D. Hong, S. Yu, and J. Cheng. Sm-Ti co-substituted $BiFeO_3$ thin films prepared by sol-gel technique. Curr. Appl. Phys. 11, s255-s259 (2011)

[23] Y. Wang, Q. Jiang, H. He, and C. Nan. Mutiferroic $BiFeO_3$ thin films prepared via a simple sol-gel method. Appl. Phys. Lett. 88, 142503 (2006).

[24] M. Polomska, W. Kaczmarek, and Z. Pajak. Electric and magnetic properties of $(Bi_{1-x}La_x)FeO_3$ solid solutions. Phys. Stat. Sol. 23, 567-574 (1974).

[25] M. N. Iliev, M. V. Abrashev, D. Mazumdar, V. Shelke, and A. Gupta. Polarized Raman spectroscopy of nearly tetragonal $BiFeO_3$ thin films. Phys. Rev. B 82, 014107 (2010).

[26] H. Ma and L. Chen. Construction of the misfit strain-temperature phase diagrams of epitaxial $BiFeO_3$ thin film. Comput. Mater. Sci. 44, 82-85 (2008).

[27] W. Eerenstein, F. D. Morrison, J. Dho, M, G. Blamire, J. F. Scott, and N. D. Mathur. Comment on "Epitaxial $BiFeO_3$ multiferroic thin film heterostructures". Science 307, 1203 (2005).

[28] H. M. Christen, J. H. Nam, H. S. Kim, A. J. Hatt, and N. A. Spaldin. Stress-induced R-MA-MC-T symmetry changes in $BiFeO_3$ films. Phys. Rev. B 83, 144107 (2011).

[29] J. Chaigneau, R. Haumont, and J. M. Kiat. Ferroelectric order stability in the $Bi_{1-x}Pb_xFeO_3$ solid solution. Phys. Rev. B 80, 184107 (2009).

[30] V. A. Khomchenko, D. A. Kiselev, E. K. Selezneva, J. M. Vieira, A. M. L. Lopes, Y. G. Pogorelov, J. P. Araujo, and A. L. Kholkin. Weak ferromagnetism in

diamagnetically-doped $Bi_{1-x}A_xFeO_3$ (A=Ca, Sr, Pb, Ba) multiferroics. Mater. Lett. 62, 1927-1929 (2008).

[31] D. H. Wang, W. C. Goh, M. Ning, and C. K. Ong. Effect of Ba doping on magnetic, ferroelectric, and magnetroelectric properties in multiferroic $BiFeO_3$ at room temperature. Appl. Phys. Lett. 88, 212907 (2006).

[32] I. Sosnowska, P. Przenioslo, P. Fischer, and V. A. Murashow. Neutron diffraction studies of the crystal and magnetic structures of $BiFeO_3$ and $Bi_{0.93}La_{0.07}FeO_3$. J. Magn. Magn. Mater. 160, 384-385 (1996).

[33] A. A. Belik, D. A. Rusakov, T. Furubayashi, and E. Takayama-Muromachi. $BiGaO_3$-based perovskites: a large family of polar materials. Chem. Mater. 24, 3056-3064 (2012).

[34] H. Yusa, A. A. Belik, E. Takayama-Muromachi, N. Hirao, and Y. Ohishi. High-pressure phase transitions in $BiMO_3$ (M=Al, Ga, and In): in situ x-ray diffraction and raman scattering experiments. Phys. Rev. B 80, 214103 (2009).

[35] A. J. Hatt, N. A. Spaldin, and C. Ederer. Strain-induced isosymmetric phase transition in $BiFeO_3$. Phys. Rev. B 81, 054109 (2010).

[36] D. Vanderbilt and M. H. Cohen. Monoclinic and triclinic phases in higher-order Devonshire theory. Phys. Rev. B 63, 094108 (2001).

[37] G. Xu, H. Hiraka, G. Shirane, J. Li, J. Wang, and D. Viehland. Low symmetry phase in (001) $BiFeO_3$ epitaxial constrained thin films. Appl. Phys. Lett. 86, 182905 (2005).

[38] H. W. Jang, S. H. Baek, D. Ortiz, C. M. Folkman, R. R. Das, Y. H. Chu, P. Shafer, J. X. Zhang, S. Choudhury, V. Vaithyanathan, Y. B. Chen, D. A. Felker, M. D. Biegalshi, M. S. Rzchowski, X. Q. Pan, D. G. Schlom, L. Q. Chen, R. Ramesh, and C. B. Eom. Strain-induced polarization rotation in epitaxial (001) $BiFeO_3$ thin films. Phys. Rev. Lett. 101, 107602 (2008).

[39] H. Toupet, F. L. Marrec, C. Lichtensteiger, B. Dkhil, and M. G. Karkut. Evidence for a first-order transition from monoclinic to monoclinic phase in $BiFeO_3$ thin films. Phys. Rev. B 81, 140101(R) (2010).

[40] C. J. M. Daumont, S. Farokhipoor, A. Ferri, J. C. Wojdel, J. Iniguez, B. J. Kooi, and B. Noheda. Tuning the atomic and domain structure of epitaxial films of multiferroic $BiFeO_3$. Phys. Rev. B 81, 144115 (2010).

[41] B. Noheda, Z. Zhong, D. E. Cox, G. Shirane, S. E. Park, and P. Rehrig.

Electric- field- induced phase transitions in rhombohedral $Pb(Zn_{1/3}Nb_{2/3})_{1-x}Ti_xO_3$. Phys. Rev. B 65, 224101 (2002).

[42] M. Davis, D. Damjanovic, and N. Setter. Electric-field-, temperature-, and stress- induced phase transitions in relaxor ferroelectric single crystals. Phys. Rev. B 73, 014115 (2006).

[43] F. Bai, N. Wang, J. Li, D. Viehland, P. M. Gehring, G. Xu, and G. Shirane. X-ray and neutron diffraction investigations of the structural phase transformation sequence under electric field in $0.7Pb(Mg_{1/3}Nb_{2/3})$-$0.3PbTiO_3$ crystal. J. Appl. Phys. 96, 1620 (2004).

[44] H. Fu and R. E. Cohen. Polarization rotation mechanism for ultrahigh electromechanical response in single-crystal piezoelectrics. Nature 403, 281 (2000).

[45] B. Noheda, D. E. Cox, G. Shirane, S. E. Park, L. E. Cross, and Z. Zhong. Polarization rotation via a monoclinic phase in the piezoelectric $92\%PbZn_{1/3}Nb_{2/3}O_3$-$8\%PbTiO_3$. Phys. Rev. Lett. 86, 3891 (2001).

[46] L. Bellaiche, A. Garcia, and D. Vanderbilt. Electric-field polarization paths in $Pb(Zr_{1-x}Ti_x)O_3$ allys. Phys. Rev. B 64, 060103(r) (2001).

[47] A. Azam, A. Jawad, A. S. Ahmed, M. Chaman, and A. H. Naqvi. Structural , optical and transport properties of Al^{3+} doped $BiFeO_3$ nanopowder synthesized by solution combustion method. J. Alloys Compd. 509, 2909-2913 (2011).

[48] http://en.wikipedia.org/wiki/Electronegativity

[49] W. Zhu and Z. Ye. Effects of chemical modification on the electrical properties of $0.67BiFeO_3$-$0.33PbTiO_3$ ferroelectric ceramics. Ceram. Int. 30, 1435-1442 (2004).

[50] H. Uchida, R. Ueno, H. Funakubo, and S. Koda. Crystal structure and ferroelectric properties of rare-earth substituted $BiFeO_3$ thin films. J. Appl. Phys. 100, 014105 (2006).

[51] F. Gao, C. Cai, Y. Wang, S. Dong, X. Qui, G. Yuan, Z. Liu, and J. Liu. Preparation of La-doped $BiFeO_3$ thin films with Fe^{2+} ions on Si substrates. J. Appl. Phys. 99, 094105 (2006).

[52] N. Huang, L. Zhao, J. Xu, J. Chen, and Y. Zhao. Effects of substitution of Sm for Bi in $BiFeO_3$ thin films prepared by the sol-gel method. Chin. Phys. Lett. 27, 027704 (2010).

[53] J. Liu, M. Li, L. Per,B. Yu, D. Guo, and X. Zhao. Effect of Ce doping on the microstructure and electrical properties of $BiFeO_3$ thin films prepared by chemical

solution deposition. J. Phys. D. Appl. Phys. 42, 115409 (2009).

[54] J. Kim, S. Kim, W. Kim, A. S. Bhalla, and R. Guo. Enhanced ferroelectric properties of Cr-doped $BiFeO_3$ thin films grown by chemical solution deposition. Appl. Phys. Lett. 88, 132901 (2006).

[55] X. Qi, J. Dho, R. Tomov, M. G. Blamire, and J. L. MacManus-Driscoll. Greatly reduced leakage current and conduction mechanism in aliovalent-ion-doped $BiFeO_3$. Appl. Phys. Lett. 86, 062903 (2005).

[56] M. Kumar and K. L. Yadav. Rapid liquid phase sintered Mn doped $BiFeO_3$ ceramics with enhanced polarization and weak magnetization. Appl. Phys. Lett. 91, 242901 (2007).

[57] Y. Wan and C. W. Nan. Ehanced ferroelectricity in Ti-doped multiferroic $BiFeO_3$ thin films. Appl. Phys. Lett. 89, 52903 (2006).

[58] S. Singh, S. Shanthy, and H. Ishiwara. Reduced leakage current in $BiFeO_3$-$BiCrO_3$ nanocomposite films formed by chemical solution deposition. J. Appl. Phys. 108, 054102 (2010).

[59] J. Wu, J. Wang, D. Xiao, and J. Zhu. Mn^{4+}:$BiFeO_3$/Zn^{2+}:$BiFeO_3$ bilayered thin films of (111) orientation. Appl. Surf. Sci. 257, 7226-7230 (2011).

[60] Y. Chishima, Y. Noguchi, Y. Kitanaka, and M. Miyayama. Defect control for polarization switching in $BiFeO_3$ single crystals. IEEE T. Ultrason. Ferr. 57, 2233-2236 (2010).

[61] A. A. Belik, S. Y. Stefanovich, B. I. Lazoryak, and E. Takayama-Muromachi. $BiInO_3$: a polar oxide with $GdFeO_3$-type perovskite structure. Chem. Mater. 18, 1964-1968 (2006).

[62] M. Azuma, K. Takata, T. Saito, S. Ishiwata, Y. Shimakawa, and M. Takano. Designed ferromagnetic, ferroelectric Bi_2NiMnO_6. J. Am. Chem. Soc. 127, 8889-8892 (2005).

[63] J. Zylberberg, A. A. Belik, E. Takayama-Muromachi, and Z. Ye. Bismuth aluminate: a new high-Tc lead-free piezo-/ferroelectric. Chem. Mater. 19, 6385-6390 (2007).

[64] A. A. Belik, S. Likubo, K. Kodama, N. Igawa, S. Shamoto, M. Maie, T. Nagai, Y. Matsui, S. Y. Stefanovich, B. I. Lazoryak, and E. Takayama-Muromachi. $BiScO_3$: centrosymmetric $BiMnO_3$-type oxide. J. Am. Chem. Soc. 128, 706-707 (2006).

[65] S. V. Halilov, M. Fornari, and D. J. Singh. Lattice instabilities and

ferroelectricity in $AScO_3$ perovskite alloys. Phys. Rev. B 69, 174107 (2004).

[66] P. Baettig, C. F. Schelle, R. Lesar, U. V. Waghmare, and N. A. Spaldin. Theoretical prediction of new high-performace lead-free piezoelectrics. Chem. Mater. 17, 1376-1380 (2005).

[67] R. D. Shannon. Revised effective ionic radii and systematic studies of interatomic distances in halides and chalcogenides. Acta. Cryst. A 32, 751 (1976).

[68] A. A. Belik, T. Wuernisha, T. Kamiyama, K. Mori, M. Maie, T. Nagai, Y. Matsui, and E. Takayama-Muromachi. High-pressure synthesis, crystal structures, and properties of perovskite-like $BiAlO_3$ and pyroxene-like $BiGaO_3$. Chem. Mater. 18, 133-139 (2006).

[69] J. X. Zhang, Q. He, M. Trassin, W. Luo, D. Yi, M. D. Rossell, P. Yu, L. You, C. H. Wang, C. Y. Kuo, J. T. Heron, Z. Hu, R. J. Zeches, H. J. Lin, A. Tanaka, C. T. Chen, L. H. Tjeng, Y. H. Chu, and R. Ramesh. Microscopic origin of the giant ferroelectric polarization in tetragonal-like $BiFeO_3$. Phys. Rev. Lett. 107, 147602 (2011).

[70] A. A. Belik, S. Iikubo, K. Kodama, N. Igawa, S. Shamoto, S. Niitaka, M. Azuma, Y. Shimakawa, M. Takano, F. Izumi, and E. Takayama-Muromachi. Neutron powder diffraction study on the crystal and magnetic structures of $BiCoO_3$. Chem. Mater. 18, 798-803 (2006).

[71] H. Bea, M. Bibes, A. Barthelemy, K. Bouzehouane, E. Jacquet, A. Khodan, J. P. Contour, S. Fusil, F. Wyczisk, A. Forget, D. Lebeugle, D. Colson, and M. Viret. Influence of parasitic phases on the properties of $BiFeO_3$ epitaxial thin films. Appl. Phys. Lett. 87, 072508 (2005).

[72] Z. Mei, S. Shang, Y. Wang, and Z. Liu. Thermodynamics of multiferroic $BiFeO_3$: applications for the deposition of $BiFeO_3$ thin films. Appl. Phys. Lett. 98, 131904 (2011).

[73] M. S. Kartavtseva, O. Y. Gorbenko, A. R. Kaul, T. V. Murzina, S. A. Savinov, and A. Barthelemy. $BiFeO_3$ thin films prepared using metalorganic chemical vapor deposition. Thin Solid Films 515, 6416-6421 (2007).

[74] Y. Lee, J. Wu, and C. Lai. Influence of La doping in multiferroic properties of $BiFeO_3$ thin films. Appl. Phys. Lett. 88, 042903 (2006).

[75] R. Zheng, X. Gao, and J. Wang. Mutiferroic $BiFeO_3$ thin films buffered by a $SrRuO_3$ layer. J. Am. Ceram. Soc. 91, 463-466 (2008).

[76] J. Fukushima, K. Kodaira, and T. Matsushita. Preparation of ferroelectric PZT films by thermal decomposition of organometallic compounds. J. Mater. Sci. 19, 595-598 (1984).

[77] V. Fruth, M. Popa, J. M. Calderon-Moreno, E. M. Anghel, D. Berger, M. Gartner, M. Anastasescu, P. Osiceanu, and M. Zaharescu. Chemical solution deposition and characterization of $BiFeO_3$ thin films. J. Eur. Ceram. Soc. 27, 4417-4420 (2007).

[78] G. Yi, Z. Wu, and M. Sayer. Preparation of $Pb(Zr, Ti)O_3$ thin films by sol-gel processing: electrical, optical, and electro-otic properties. J. Appl. Phys. 64, 2717 (1988).

[79] Y. Takahashi, Y. Matsuoka, and K. Yamaguchi. Dip coating of PT, PZ and PZT films using an alkoxide-diethanolamine method. J. Mater. Sci. 25, 3960-3964 (1990).

[80] http://en.wikipedia.org/wiki/Acetylacetone

Chapter 2

Effect of Excess Bi on $BiFeO_3$ Structure and Ferroelectric Properties

2.1 Introduction

There have been many researches focus on $BiFeO_3$ thin films and many attractive results are obtained. The detected polarization is able to around 100 μC cm^{-2}, [1] which is almost the same as theoretical value. However, the obtained films, in particular, polycrystalline films had several common problems caused by some unidentified factors, which resulted in irreproducible physical characteristics. For example, the polarization curves of films are unsaturated until high electric field is applied. The values of saturated polarization as well as coercive electric field are scattered, strongly depended on the deposition conditions. These issues have been frequently argued from the perspective of Bi deficiencies and the resultant leakage current. [2-4] The Bi deficiencies are known to occur in vacuum process or annealing for crystallization at high temperature because of the high volatility of Bi. To compensate for the Bi loss, Bi is conventionally overdosed in most of the studies. Thus it is strongly required to precisely understand the influence of non-stoichiometric Bi on the structural and ferroelectric properties of BFO films. Gao et al. [5] and Kim et al. [6] reported that overdosing the 5-10 mol% amount of Bi could effectively improve the ferroelectric properties of the BFO thin films. However, these works have focused on only the phenomenological changes of the ferroelectric behavior for the excess Bi, lacking the detailed discussion on why overdosed Bi influences the structure and properties of the films.

In this section, we describe the effect of overdosed Bi on the structural and electrical properties of BFO films prepared by CSD and discuss the ferroelectric behavior in relation to structural change yielded by the excess Bi. These results will offer better understanding of the contribution of excess Bi on properties of BFO and its relationship with the above issues.

2.2 Experiment

2.2.1 Precursor solution

BFO thin films were fabricated by the CSD method on glass substrates (Corning Eagle XG, Non-alkaline aluminosilicate glass). The thermal expansion coefficient of glass substrate (3.17×10^{-6} $^oC^{-1}$) is close to that of Si (3×10^{-6} $^oC^{-1}$). Based on the advantage of precise control of composition for the CSD method [7], we prepared precursor solutions with stoichiometric and 5%, 8%, 10%, 12% and 15% mole ratios of excess Bi, named as BF, B1.05F, B1.08F, B1.1F, B1.12F and B1.15F, respectively. The starting reagents were bismuth nitrate ($Bi(NO_3)_3\cdot5H_2O$, 99.5%) and ferric nitrate ($Fe(NO_3)_3\cdot9H_2O$, 99%). They were dissolved in acetic acid ($C_2H_4O_2$, 99.7%) by stirring under heating. An appropriate amount of acetylacetone ($C_5H_8O_2$, 99%) was added into the solution as a chelating agent. The concentration of precursor solutions was 0.2 mol L^{-1}.

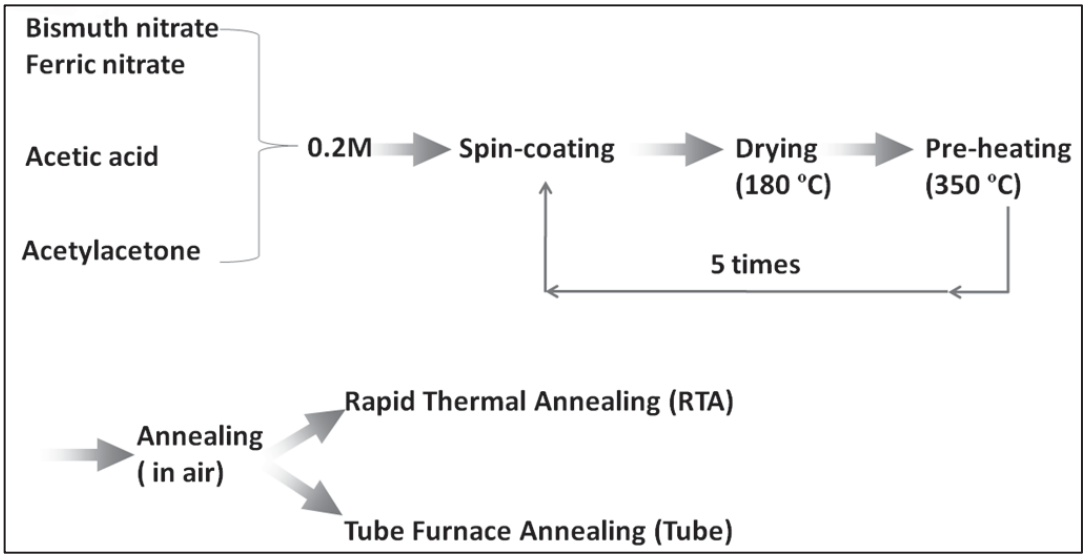

Figure 2.1 Flow chart for deposition $BiFeO_3$ thin films by CSD method.

2.2.2 Film deposition

The precursor solution was spin-coated onto glass substrate, followed by pre-heating at 180 °C and heating at 380 °C for 180 s to remove the solvent and organic pyrolysis, respectively. These steps were repeated for 5 times to obtain the desired thickness. Finally, the films were annealed for crystallization using both rapid thermal annealing (RTA) and normal annealing (Tube), where the heating rates and holding times at final temperatures are 100 °C s^{-1}, 10 min for the RTA and 10 °C min^{-1}, 5 h for the normal annealing, respectively. Flow chart is shown in Figure 2.1.

2.2.3 Measurement

The thickness of the thin film with 5 layers was detected to be near 200 nm by stylus method. X-ray diffraction (XRD) was carried out for structure detection by using Rigaku-Smartlab. Raman spectra were collected from JASCO NRS-3300 to investigate molecular vibrations and bonds. Atomic force microscopy (AFM) was used for surface morphology evaluation. In order to detect the distribution of excess Bi in thin films, transmission electron microscope (TEM) associated with energy dispersive x-ray analysis (EDAX) was carried out on cut-cross section of films.

For electric measurement, we prepared $LaNiO_3$ (LNO) bottom electrode and Au top electrode (200 μm diameter) by sputtering. Leakage current behaviors were estimated by using Keithley 230 voltage source and Keithley 6487picoammeter. The polarization hysteresis was measured at a frequency of 10 kHz at room temperature by using ferroelectric test system FCE-1.

2.3 Results and discussion

2.3.1 Structural and morphology properties

Figure 2.2 shows x-ray diffraction patterns of synthesized thin films annealed by RTA at 500 °C, 550 °C, and 600 °C in air. In Figure 2.2(a), when annealed at 500 °C, the film with stoichiometric composition shows only the γ-Bi_2O_3 phase stable at low temperature (500 °C). When the annealing temperature up to 550 ºC, the sample

crystallizes in BFO-*R*3*c* phase without any other phase can be detected, matching well with PCPDF No. 01-072-7678. In Figure 2.2(e), when annealed at 500 ºC, the XRD curve of B1.15F shows a peak around 28 º, arisen from the formation of

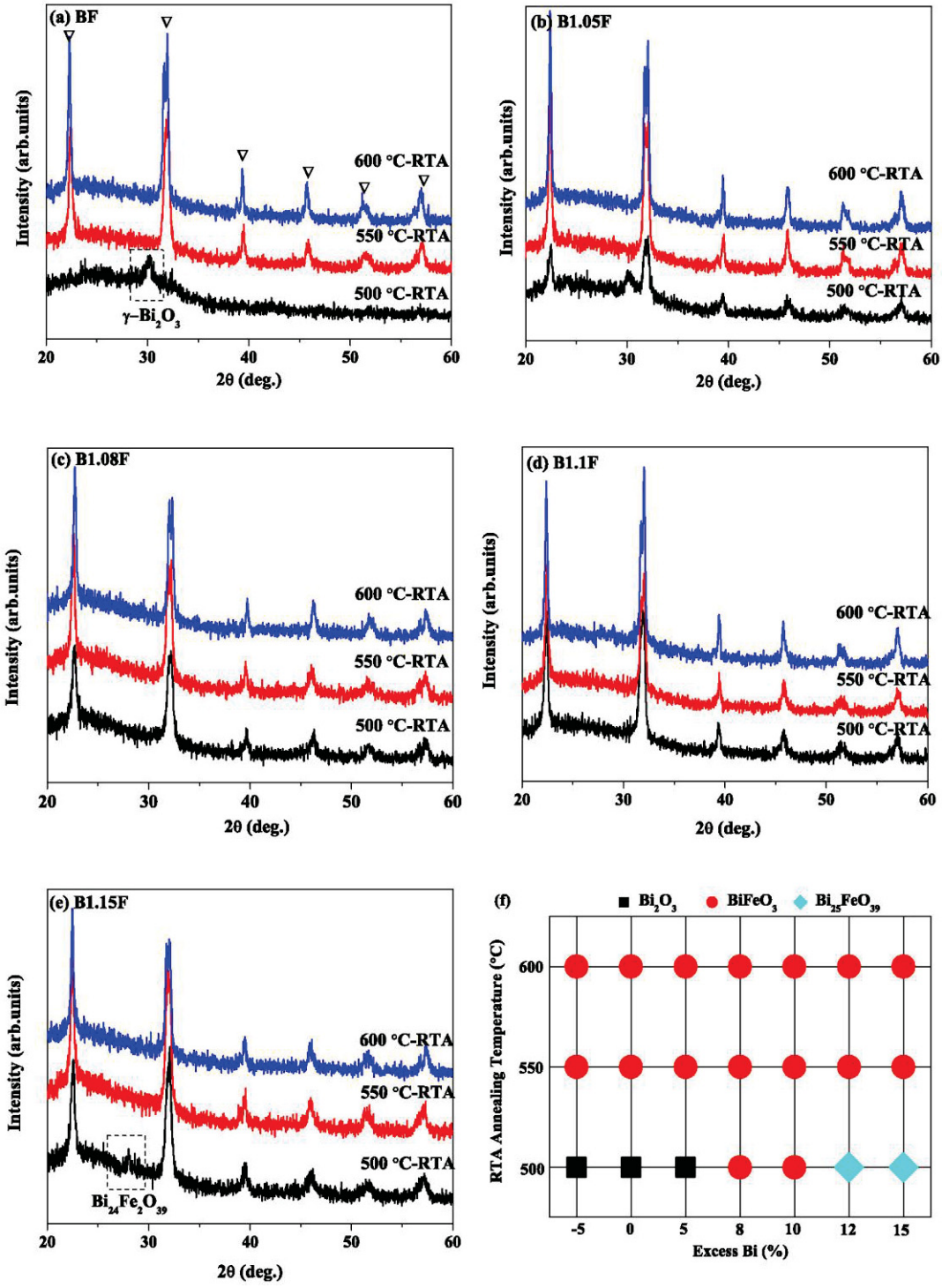

Figure 2.2 X-ray diffraction patterns of **(a)** BF, **(b)** B1.05F, **(c)** B1.08F, **(d)** B1.1F, **(e)** B1.15F, and **(f)** process condition diagram of RTA-annealed $BiFeO_3$ with excess Bi.

excess-Bi phase, $Bi_{24}Fe_2O_{39}$. With increasing annealing temperature, peak for the second phase disappears. It means that increasing annealing temperature promotes the crystallization of $BiFeO_3$ phase and prevents the formation of the other phases, such as γ-Bi_2O_3 and $Bi_{24}Fe_2O_{39}$. Meanwhile, the peak intensities of γ-Bi_2O_3 phase which is easy to form at 500 ºC turn to weak for B1.05F and cannot be detected for B1.08F and B1.1F. The increased excess Bi prevents the formation of Bi_2O_3 and relatively lowers the crystallization temperature of BFO.

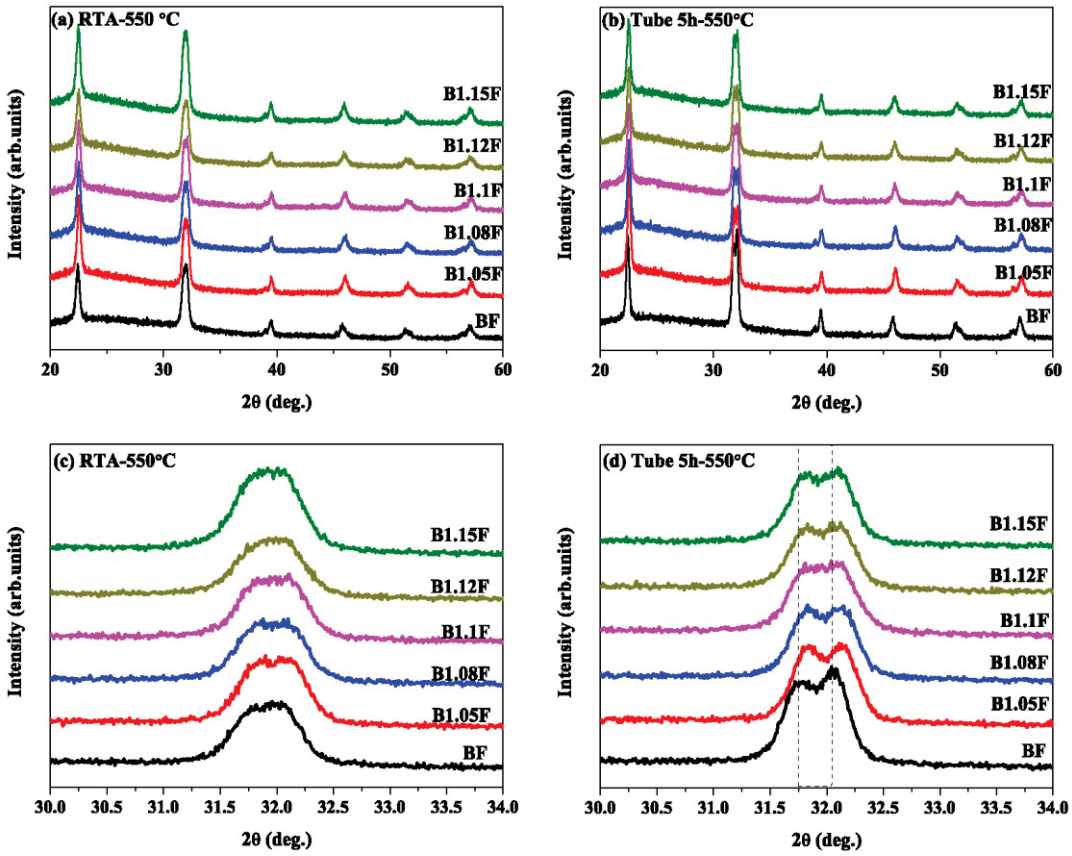

Figure 2.3 XRD patterns of **(a)** RTA- and **(b)** Tube 5h- annealed BFO samples, and partially enlarged (30-34º) XRD patterns for **(c)** RTA- and **(d)** Tube 5h- annealed samples.

Based on the XRD results, the process condition diagram of $BiFeO_3$ is shown in Figure 2.2(f), as a function of excess Bi and RTA annealing temperature. It is obvious that at some certain annealing temperature, such as 550 ºC, thin films can crystallize in BFO-*R*3*c* symmetry without detectable second phase within a wide range of excess Bi. In other words, it means that there would be many defects in the prepared *R*3*c* structure originated from nonstoichiometry by overdosed Bi. Thus it is important

to investigate the influence of defects on structure of BFO films.

However, it should be mentioned that the obtained phases from RTA may be not in final stable states because the RTA is not a process under thermodynamic equilibrium. In order to optimize the crystal structure, we prepared another group of samples by normal furnace annealing at 550 °C in air for 5 h (Tube 5h). As shown in Figure 2.3(b) that all the samples show rhombohedral BFO structure with *R*3*c* symmetry without obvious precipitation of other phases, similar with RTA-annealed samples (Figure 2.3(a)). It indicates that *R*3*c* phase is stable at 550 ºC. In partially enlarged figures (Figure 2.3(c) and (d)), the primary split peaks around 32 º which belong to (104) and (110) planes for *R*3*c* symmetry turn to be clear after long-time annealing, suggesting the improvement of crystallinity. Moreover, it can be noticed that there are shifts for the peak positions of each sample, which indicates the change of lattice constants.

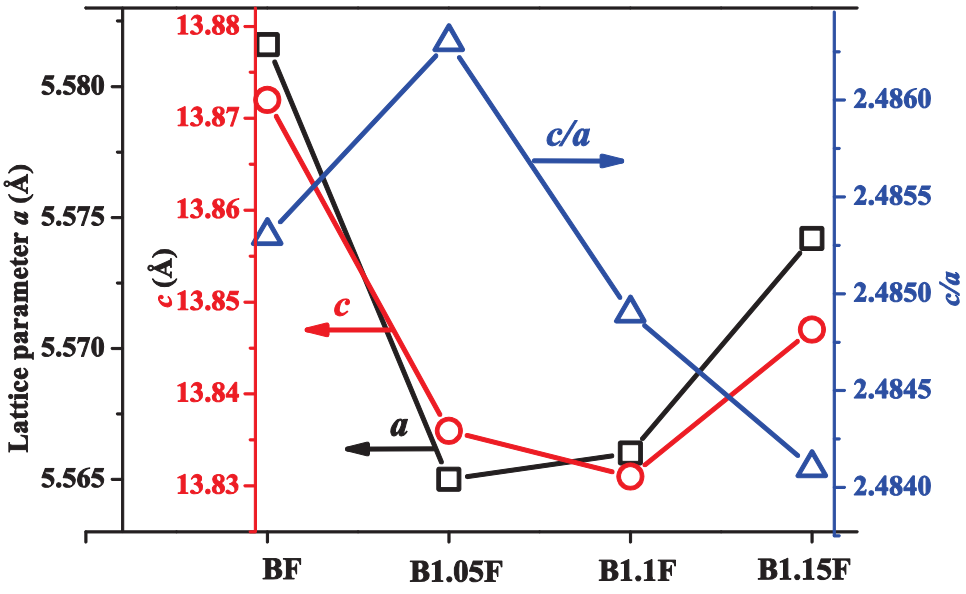

Figure 2.4 The calculated lattice parameters of Tube 5h- annealed samples.

The lattice parameters of Tube-5h annealed samples were calculated using the whole powder pattern fitting (WPPF) method, as shown in Figure 2.4. The lattice constants *a* and *c* decrease rapidly with adding the excess Bi, taking a minimum around 5 mol% (B1.05F), which are 0.30 % lower than those of the stoichiometric BF film. It is suggested that the overdosed Bi is likely to be incorporated into the

perovskite lattice and the ratio of constituent elements in the unit lattice will change consequently due to charge compensation. The non-stoichiometric defects in BFO originated from evaporation loss of Bi during long-time annealing generally expand the lattice because of charge repulsion. As shown in Figure 2.4 that BF sample keeps the largest *a* and *c* value, confirming the presence of Bi vacancies. B1.05F shows smaller *a* and *c* values compared with BF, indicating the decrease of defects. It means that around 5 mol% excess Bi can compensate the evaporation loss of Bi during long-time annealing. The increment of lattice constants for B1.15F may be due to a relative decrease of Fe: Bi ratio accompanied by vacancy-defect formation at the Fe-site.

Apart from defects, the films suffer huge in-plane stress from the substrate, which

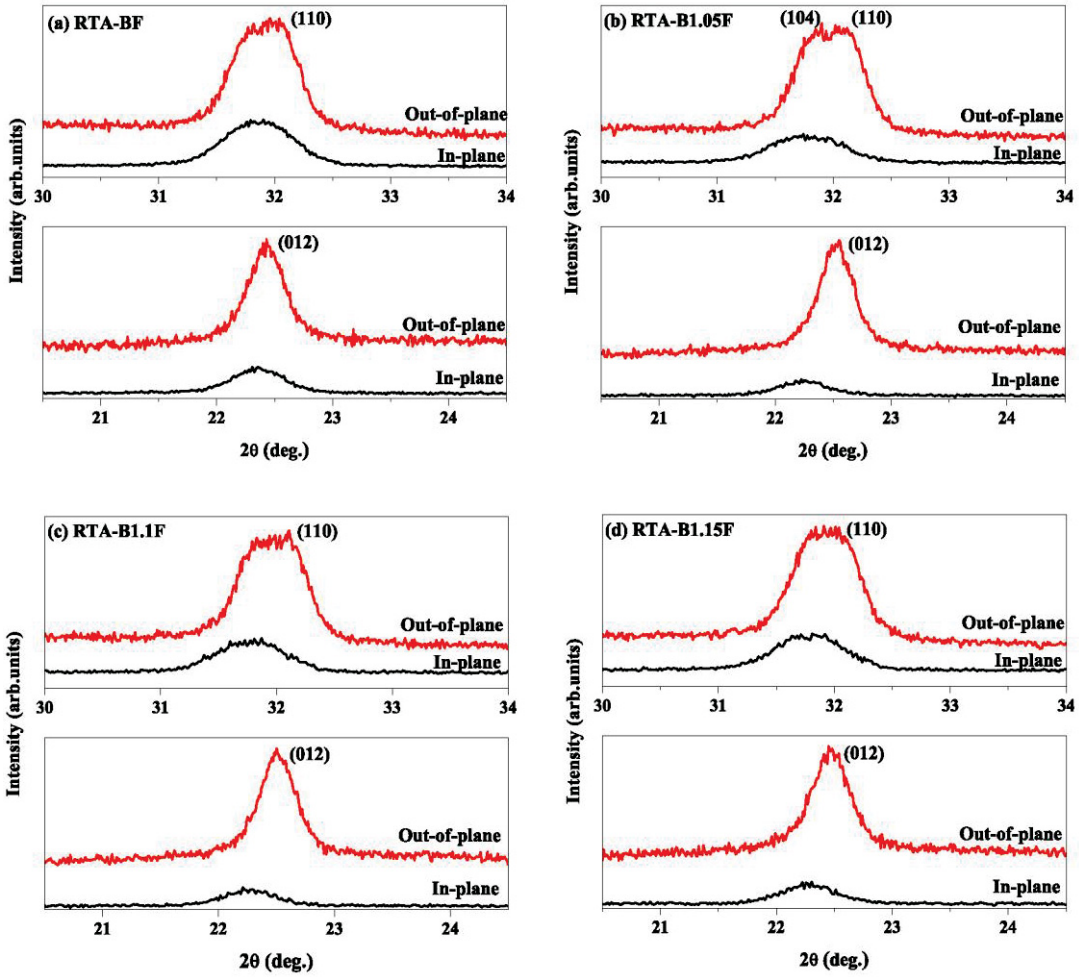

Figure 2.5 In-plane XRD curves around (012) and (110) peaks in comparison with the out-of-plane XRD curves for RTA- annealed **(a)** BF, **(b)** B1.05F, **(c)** B1.1F and **(d)** B1.15F.

can be affected by overdosed Bi and take influence on BFO structure. Figure 2.5 and Figure 2.6 show the in-plane XRD curves around (012) and (110) peaks in comparison with the out-of-plane XRD curves for RTA- and Tube 5h- annealed samples, respectively. The positions of all the in-plane peaks shift somewhat to lower angle region compared with those of out-of-plane peaks, indicating the increase of interplanar spacing.

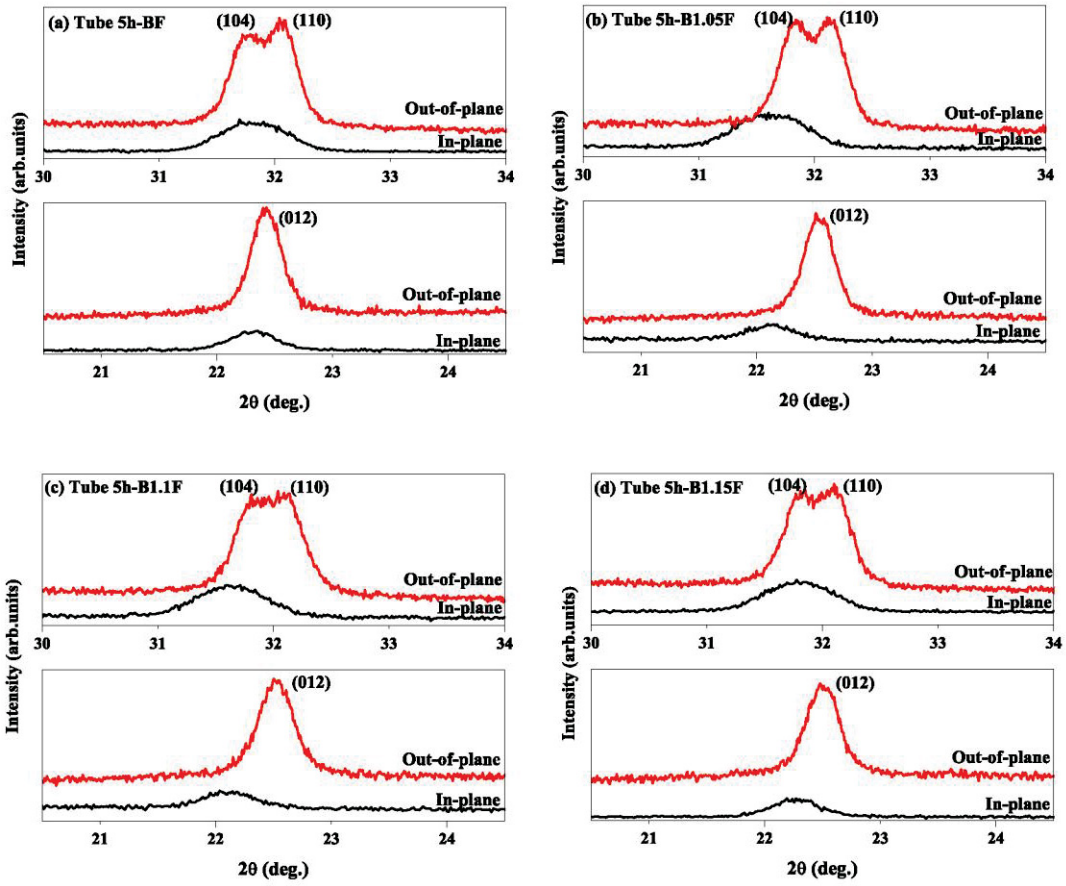

Figure 2.6 In-plane XRD curves around (012) and (110) peaks in comparison with the out-of-plane XRD curves for Tube 5h- annealed **(a)** BF, **(b)** B1.05F, **(c)** B1.1F and **(d)** B1.15F.

In order to discuss these relative changes for in-plane distortion, we calculate $\Delta d = (d_{\text{in-plane}}-d_{\text{out-of-plane}})/d_{\text{out-of-plane}}$ for (012) and (110) planes where d denotes the interplanar spacing of each lattice plane. Figure 2.7 shows the results. The observed Δd comes from the in-plane stress caused by the different thermal expansion coefficients between films and substrates. In our studies, the thermal expansion coefficient of glass substrate is smaller than that of $BiFeO_3$ films, and the strain

derived from the glass substrate is estimated to be an order of GPa, assuming the Young modulus and Poisson's ratio similar to ferrite. [7] As a result of that, the in-plane stress is tensile, which results in positive Δd value.

In Figure 2.7, it is interesting that for the sample with excess Bi, Δd of the (110) plane is almost half that of the (012) plane, indicating that the in-plane distortion depends on the lattice plane. And it is obvious that all the four curves follow the similar tendency that Δd value is maximum at B1.05F. It is opposite to the behavior of lattice constants as shown in Figure 2.4. The sample which keeps the smallest lattice parameters shows the largest in-plane distortion. As discussed above, around 5 mol% excess Bi can compensate the evaporation loss of Bi during long-time annealing. In other words, it can be suggested that B1.05F is actual stoichiometric and there are Bi vacancies in BF sample and Fe vacancies in B1.1F and B1.15F samples. The defective structure will suffer stress relaxation, which is the response for the slight crystal distortion. For B1.05F sample, it shows better crystallinity and is strained without stress relaxation, showing larger Δd value.

Moreover, comparing the Δd value of RTA- and Tube 5h- annealed samples, the increased Δd value after Tube 5h- annealing suggests the enhanced strain and the

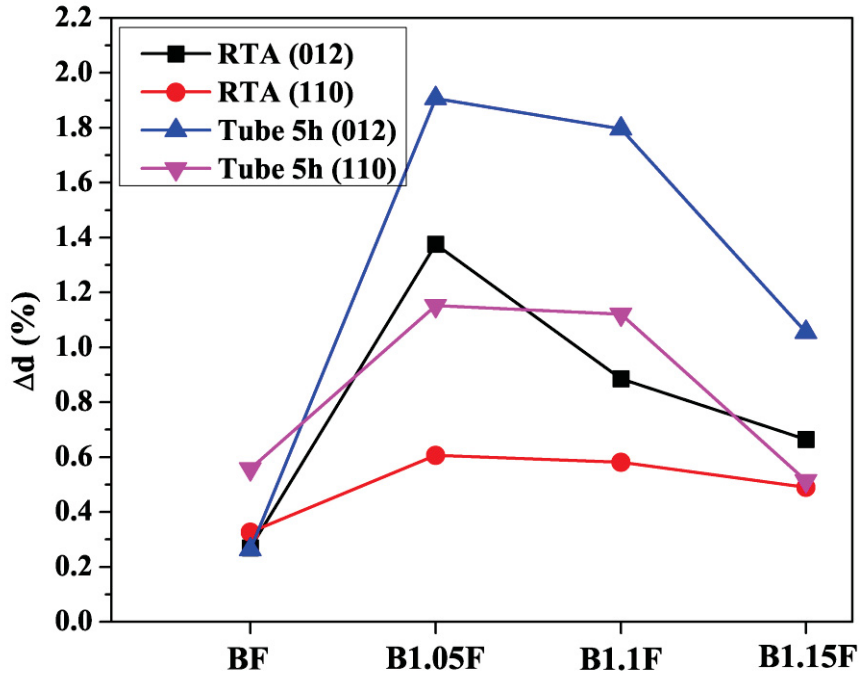

Figure 2.7 The calculated Δd value, where d denotes the interplanar spacing of each lattice plane and $\Delta d = (d_{\text{in-plane}} - d_{\text{out-of-plane}})/d_{\text{out-of-plane}}$.

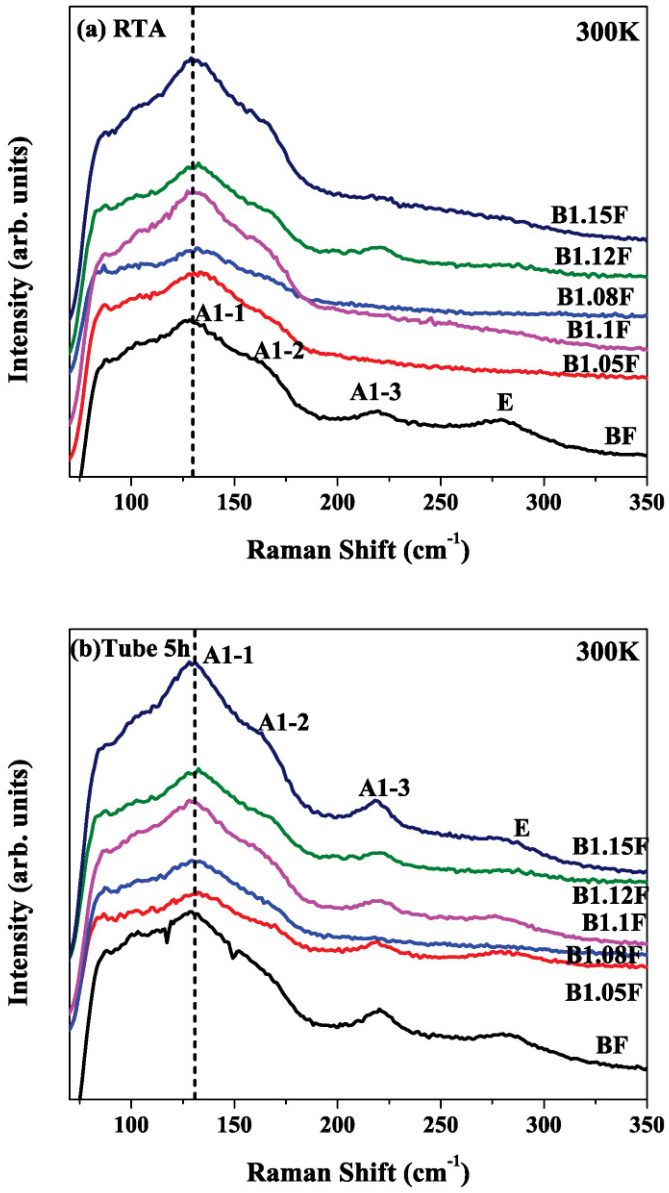

Figure 2.8 Raman spectra of **(a)** RTA- and **(b)** Tube 5h- annealed BFO films, collected at room temperature without polarization.

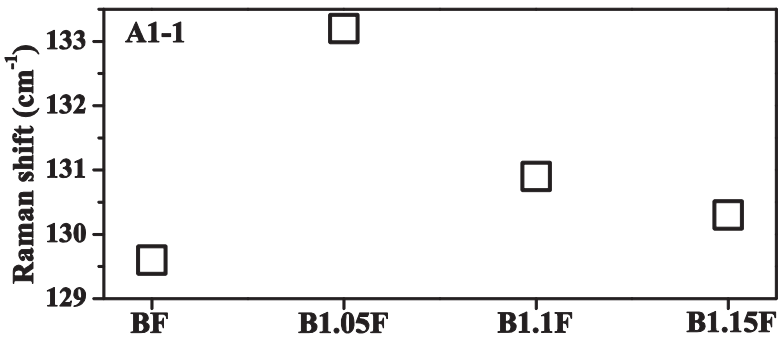

Figure 2.9 Raman shift of A_1-1 mode determined by curve fitting for Tube 5h-annealed samples.

resultant large crystal distortion. Besides the improvement of crystallinity, the bonding reaction of overdosed Bi with O during long-time annealing is considered to be contributed for the enhanced strain. As reported that, in BFO sample which keeps overdosed Bi, the unbonded Bi''' can be bonded with O during annealing in air, as the expected reaction is shown below: [8, 9]

$$2Bi'''+3O_2=2Bi_{Bi}+6O_O+6h^{\cdot} \quad (2.1)$$

The bonding reaction will lead to integrated structure and higher stress between interplanar. But it can be noticed that a certain amount of electro holes are produced in the reaction, which perhaps take influence on electric properties.

As the evidence for molecular vibrations, Figure 2.8 show the Raman spectra collected at room temperature without polarization. The Raman active modes of the rhombohedral BFO can be summarized using the following irreducible representation: [10]

$$\Gamma=4A_1+9E \quad (2.2)$$

Among these modes, the A_1-1 mode around 130 cm^{-1} has a symmetrical Lorentzian profile with the highest intensity.[11, 12] This mode is influenced by the force constant of Bi-O in the rhombohedral BFO where the short-range interatomic force dominates over the long-range ionic force. Thus, BFO crystal with higher quality is considered to keep higher Raman frequency for A_1-1 mode. It is also known that the increase of the Raman frequency shift is associated with the tensile stress existing in the film.[13] The larger the tensile stress existing in the film, the higher frequency of Raman shift appears. For closer inspection, the positions of A_1-1 mode determined by curve fitting are plotted in Figure 2.9. The highest Raman frequency shift is observed for B1.05F, which confirms the above results that the film with excess Bi around 5 mol% is strongly tensile-strained accompanied by high crystalline quality, as compared with other samples.

The surface morphology of BFO samples is investigated by AFM as shown in Figure 2.10. B1.05F shows smaller crystal grain compared with BF and B1.1F. Meanwhile, the grain grows obviously after Tube 5h annealing.

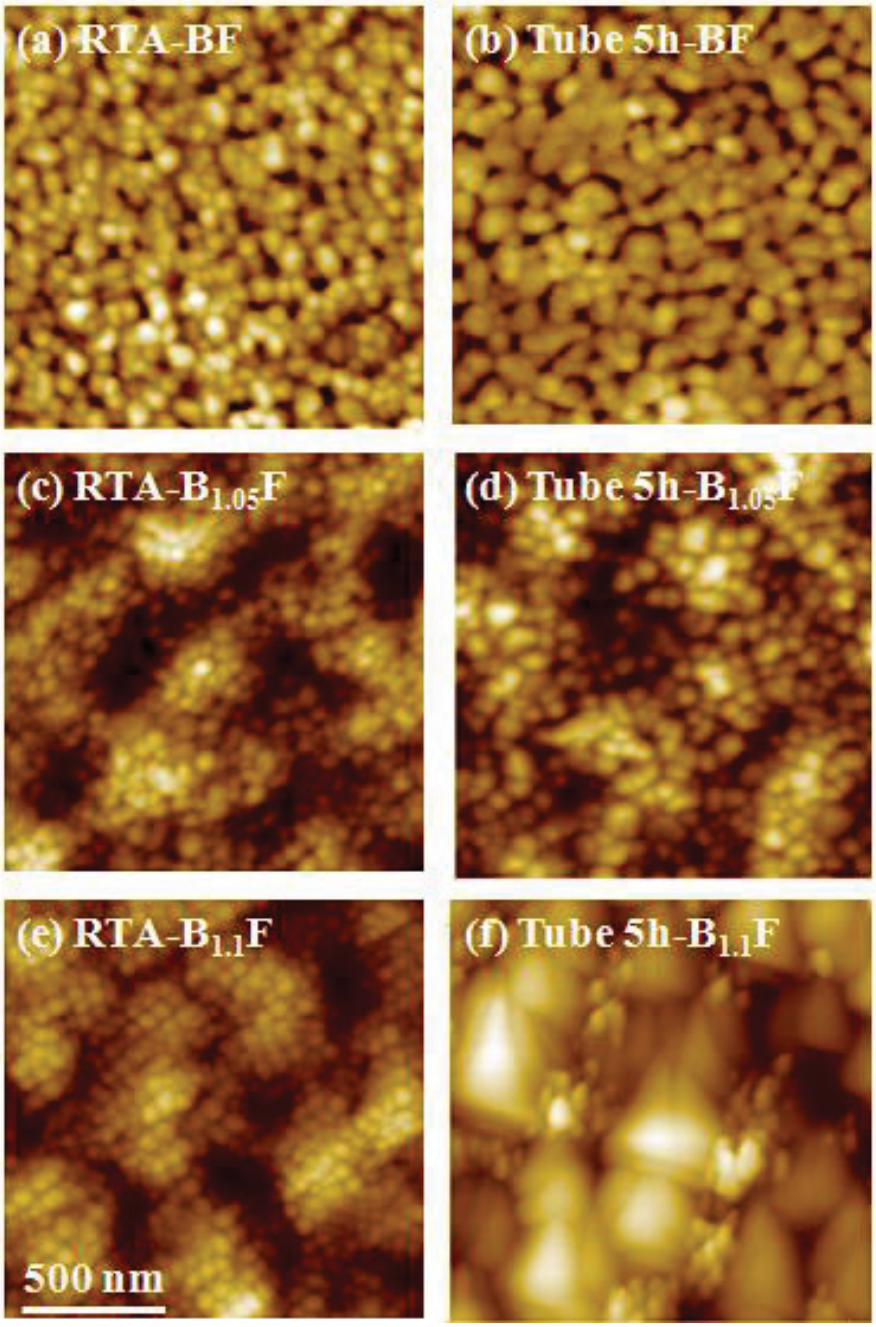

Figure 2.10 AFM images for **(a)** RTA- and **(b)** Tube 5h- annealed BF, **(c)** RTA- and **(d)** Tube 5h-annealed B1.05F, and **(e)** RTA- and **(f)** Tube 5h- annealed B1.1F.

The TEM-EDAX images of Tube 5h-annealed B1.1F measured from cross-cut section are shown in Figure 2.11(a) and (b). Figure 2.11(c) is the overlayer of Figure 2.11(a) and (b). It is clear that excess Bi disperses well in the thin film. A rich Bi region forms around the interface and no obvious second phase is detected.

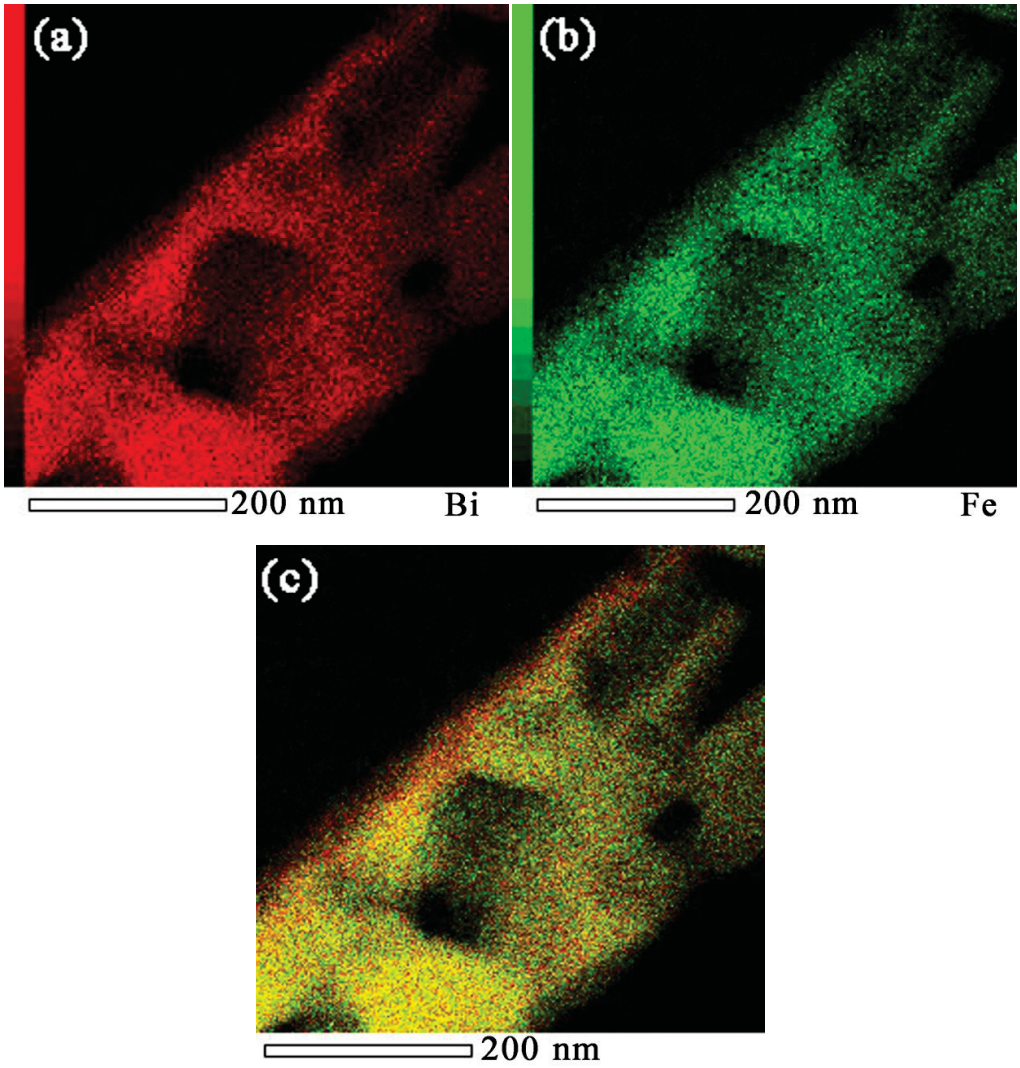

Figure 2.11 TEM-EDAX images of **(a)** Bi, **(b)** Fe and **(c)** overlayer for Tube 5h- annealed B1.1F measured from cross-cut section.

2.3.2 Electric properties

Figure 2.12 shows the leakage current density (*J*) versus applied electric field (*E*) curves of Au/BFO/LNO/glass structures measured at room temperature. The Tube 5h- annealed samples show leakage current one or two orders of magnitude higher than that of RTA- annealed samples. The potential reasons for the increased leakage from long-time annealing are those: (1) grain growth, which is confirmed by AFM images. Fujisawa *et al*. [14] reported that in PZT films the grain boundary was the leakage current conduction path. Based on the schematic diagrams given from Miao

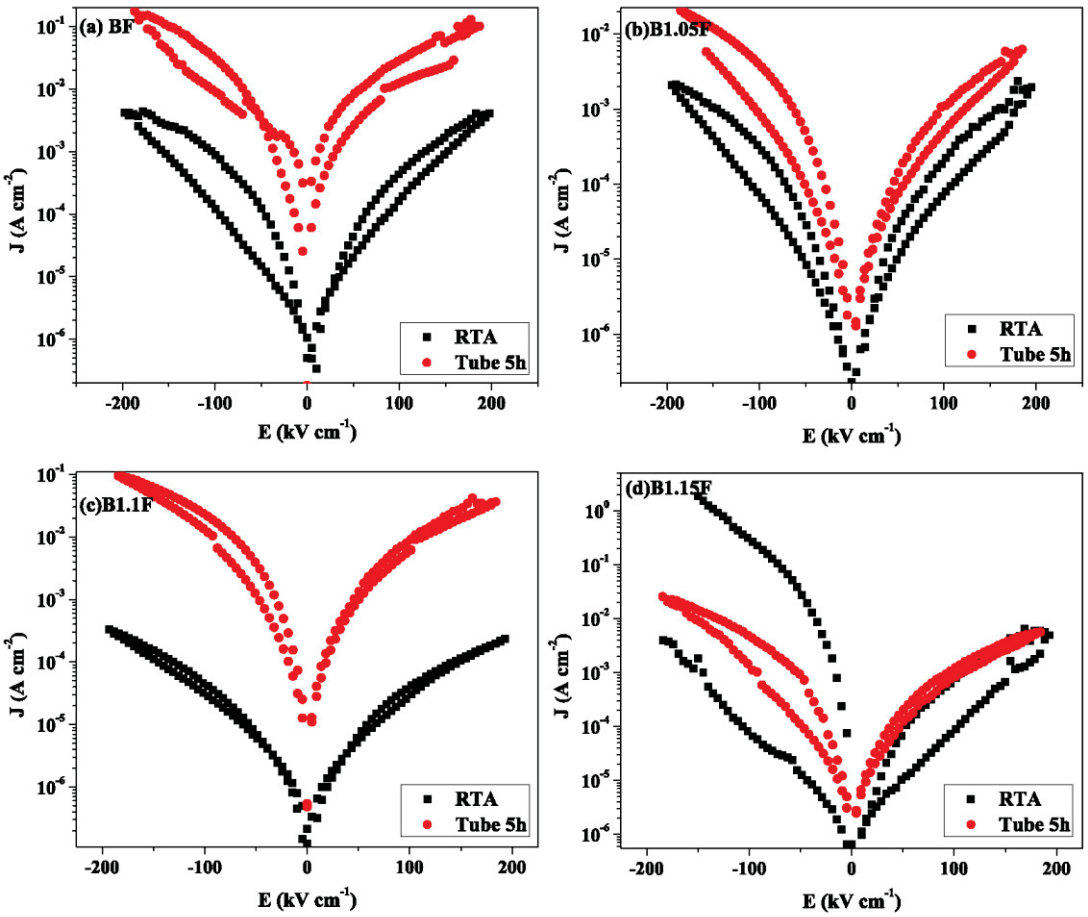

Figure 2.12 *J-E* curves of Au/BFO/LNO/glass structures measured at room temperature for **(a)** BF, **(b)** B1.05F, **(c)** B1.1F and **(d)** B1.15F.

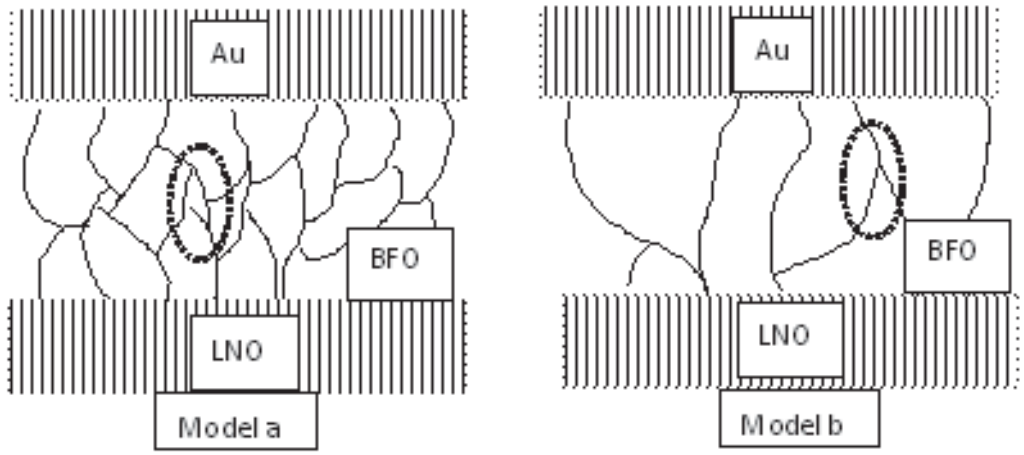

Figure 2.13 Sketch for the possible current conduction path in **(a)** RTA- and **(b)** Tube 5h- annealed BFO films.

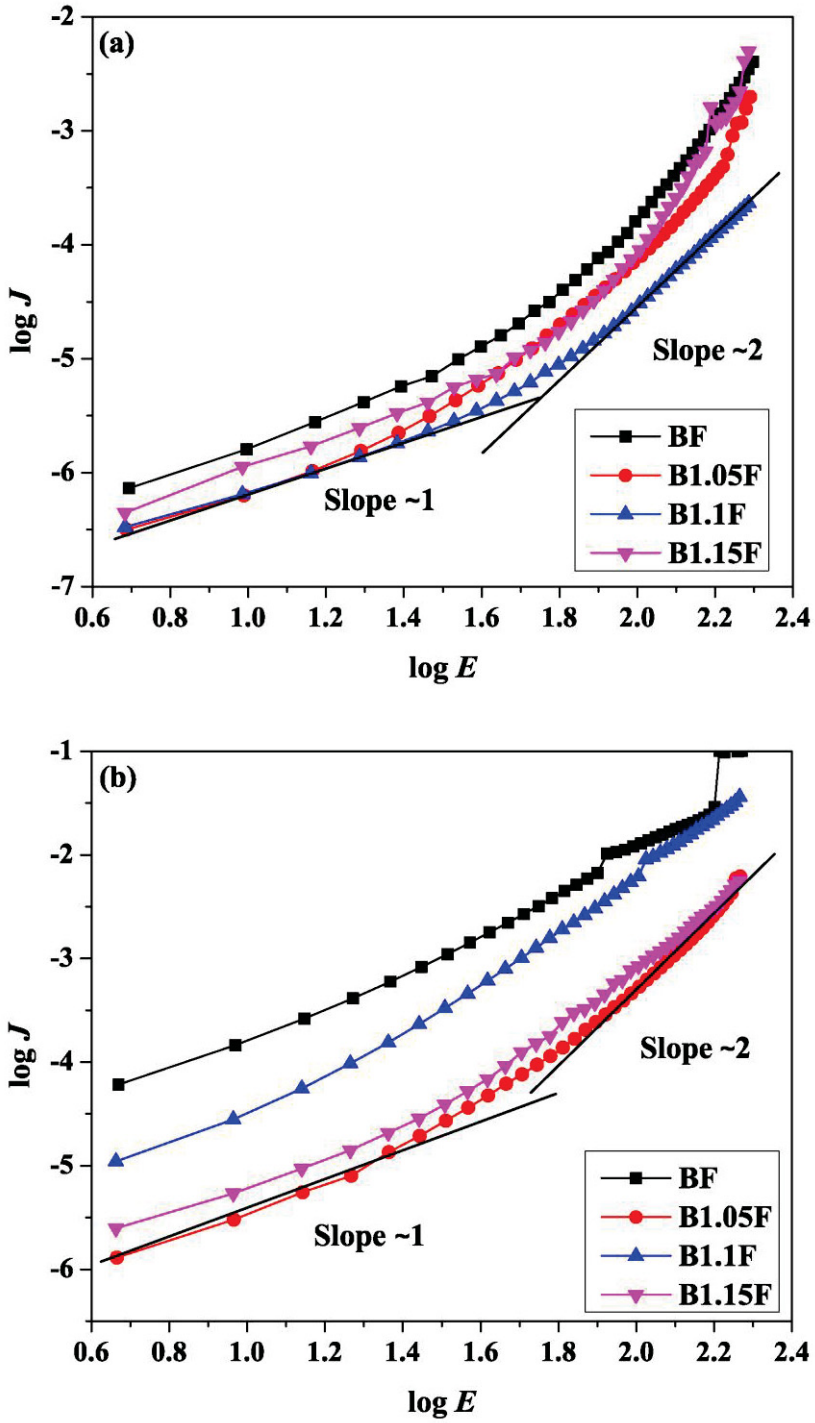

Figure 2.14 log*J*-log*E* curves for **(a)** RTA- and **(b)** Tube 5h- annealed BFO films.

et al. [15] for BST films, we draw a sketch to describe the possible current conduction path in Au/BFO/LNO structure (Figure 2.13). In model a, which shows small crystal grain, the short-cut routes for leakage should be blocked (circle area) and thereby lead to lower leakage current in RTA- annealed sample. In model b, which has larger grain size and relatively short conduction paths, the leakage current increases. In

other words, the higher leakage current exhibited in Tube 5h- annealed films may be attributed to larger grain size and shorter conduction paths. (2) Increased electron holes. For sample with excess Bi, a reasonable quantity of electron hole ($h^{\cdot}$) formed after long-time annealing, arisen from the bonding reaction between un-bonded excess Bi and oxygen. It is reported that the $h^{\cdot}$ can act as a detrimental carrier of leakage current. Thus the increased leakage after long-time annealing is reasonable.

Figure 2.14 show the log*J*-log*E* curves for (a) RTA- and (b) Tube 5h- annealed samples. Curves of log*J*-log*E* are approximated to a straight line with gradient of 1 at the beginning, followed by a straight line with gradient of 2. These suggest that the conduction at interfaces of Au/BFO and BFO/LNO is ohmic and the space charge limited current (SCLC) becomes dominant in the range of higher electric field. [15]

The current density for SCLC can be express as

$$J_{SCLC} = \frac{9\varepsilon\varepsilon_0\mu}{8d}E^2 \tag{2.3}$$

where J is current density, E is electric field, ε_0 is permittivity of vacuum, ε is dielectric constant, d is thickness, μ is carrier mobility and the expected slope is 2-3. [16, 17]

In both of (a) and (b) figures, stoichiometric BF films show largest leakage current. A similar reduction of leakage current by overdosed Bi was reported for the films prepared by CSD method, though the *J*-*E* behavior is slightly different with our results in the low electric field region. [5, 9, 18] In these papers, the lower leakage current was discussed in the following two terms: (1) reduced defects, assuming that the Bi vacancies due to Bi_2O_3 volatility were compensated by excess Bi or (2) the grain size reduction with the increase of excess Bi. In our studies, the changes of lattice parameters by adding excess Bi support the contribution of the term (1), that is, metal vacancies in both A and B-sites are minimum around the excess Bi amount of 5 mol%. In addition, AFM images of the grain show that the term (2) may be concerned with the leakage current. Particularly for Tube 5h- annealed samples, the smaller grain as seen in B1.05F decreases carrier mobility due to the presence of complex grain boundaries which makes leakage-path barriers.

Figure 2.15 shows electric polarization (*P*-*E*) curves of BFO measured at room temperature. Except B1.15F, the other samples exhibit well-saturated hysteresis after

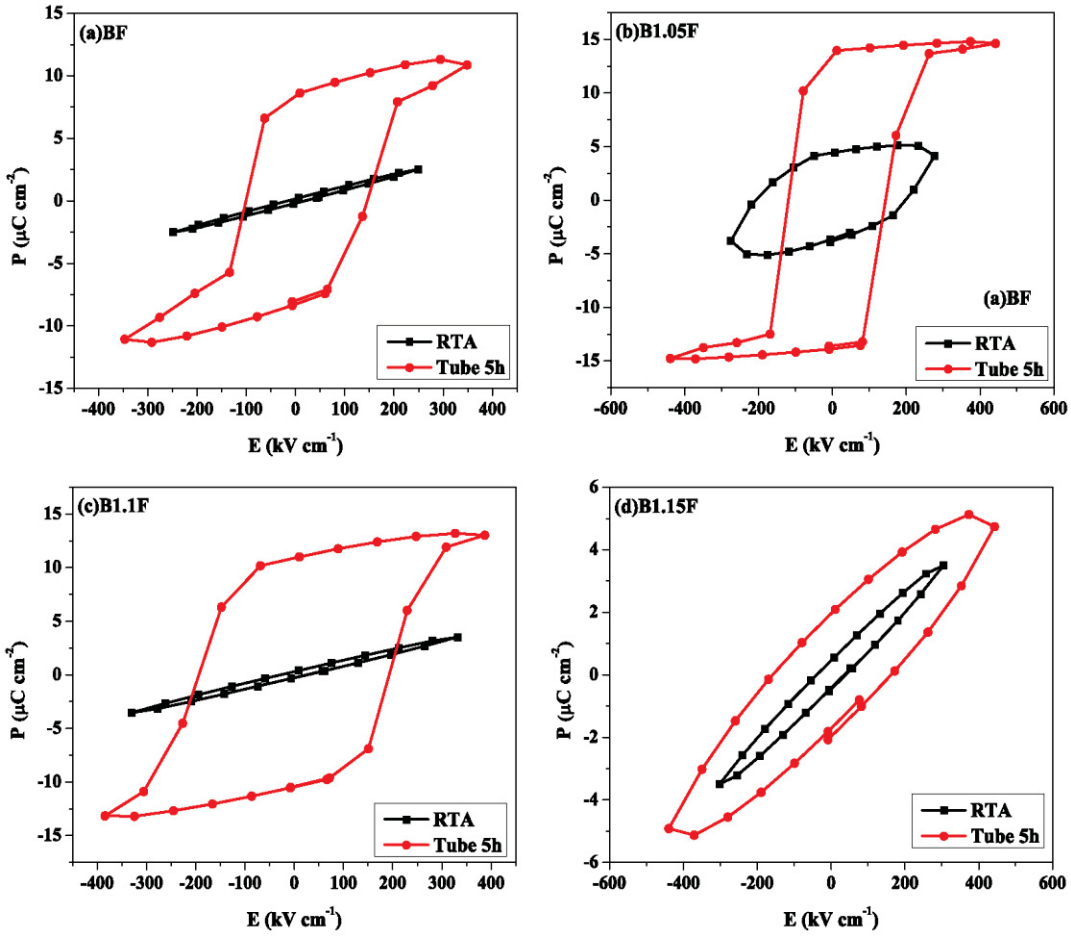

Figure 2.15 *P-E* curves of **(a)** BF, **(b)** B1.05F, **(c)** B1.1F and **(d)** B1.15F measured at room temperature at 10 kHz.

Tube 5h- annealing. It is interesting that RTA- annealed samples which are low conductivity, shows poor polarization behavior, while Tube 5h- annealed samples which keep high leakage, shows enhanced polarization. As a result of this, we suggest there is little relationship between leakage current and polarization behavior.

For Tube 5h- annealed samples, the remnant polarization (P_r) takes a maximum of 14.8 μC cm^{-2} and the coercive field (E_c) takes a minimum of 117 kV cm^{-1} for B1.05F, respectively, showing similar behavior to calculated Δd result that the distortion is maximum at B1.05F. As shown in Figure 2.16, except stoichiometric BF samples, there is an approximate linear relationship between P_r value and calculated Δd for samples with excess Bi. It indicates that the P_r value of the films should strongly depend on the strain [19] and the resultant lattice distortion in the films, i.e. the Δd

value. The lattice distortion induces Fe-ion displacement relative to the negative charge center, as well as the ion off-centering driven by the stereochemically active $6s^2$ lone pairs on Bi^{3+} ion. For B1.05F, the overdosed 5 mol% Bi compensates the Bi vacancies to reduce crystal defects firstly and then the long-time annealing optimizes crystallinity to enhance strain. In this situation, the strain-induced distortion is maximum and lead to largest P_r value.

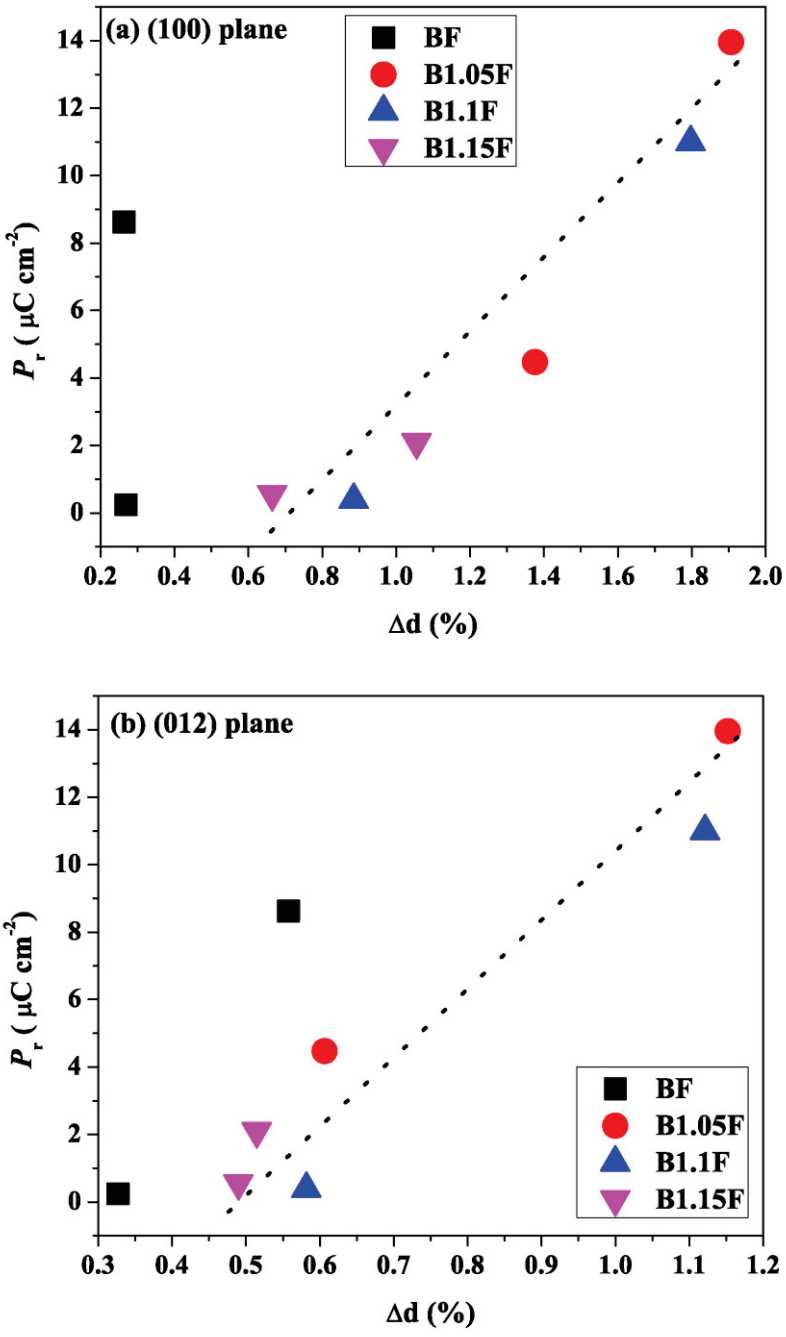

Figure 2.16 Plots for remnant polarization (P_r) vs. in-plane Δd of **(a)** (110) and **(b)** (012) plane.

2.4 Conclusions

Polycrystalline $BiFeO_3$ thin films with overdosed Bi up to 15 mol% have been prepared through chemical solution deposition (CSD). All the films crystallize in *R*3*c* structure after annealing at 550 ºC for 5h by normal furnace. The structure analysis by the out-of-plane and the in-plane XRD show that the film with 5 mol% excess Bi has the smallest lattice parameters indicative of the low ion vacancies and is strongly strained. Moreover, long-time annealing is benefit for crystallization and building up stress, which will further enhance polarization. The ferroelectric polarization curve of film with 5 mol% excess Bi shows well saturated hysteresis accompanied by the largest saturation polarization of 14.8 μC cm^{-2} after long-time annealing. It is found that the value of saturation polarization is strongly correlated with the crystal deformation induced by in-plane tensile stress. These indicate that the excess Bi greatly influences the *P*-*E* properties of BFO thin films via enhancement of lattice deformation induced by in-plane stress.

References

[1] J. Wang, J. B. Neaton, H. Zheng, V. Nagarajan, S. B. Ogale, B. Liu, D. viehland, V. Vaithyanathan, D. G. Schlom, U. V. Waghmare, N.A. Spaldin, K.M. Rabe, M. Wuttig, and R. Ramesh. Epitaxial $BiFeO_3$ multiferroic thin film heterostructres. Science 299, 1719-1722 (2003).

[2] J. Wu and J. Wang. Mutiferroic behavior and electrical conduction of $BiFeO_3$ thin film deposited on quartz substrate. J. Alloys Compd. 507, L4-L7 (2010).

[3] A. Z. Simoes, A. H. M. Gonzalez, L. S. Cavalcante, C. S. Riccardi, E. Longo, and J. A. Varela. Ferroelectric characteristics of $BiFeO_3$ thin films prepared via a simple chemical solution deposition. J. Appl. Phys. 101, 074108 (2007).

[4] R. Zheng, X. Gao, J. Wang, and S. Ramakrishna. Multiferroic $BiFeO_3$ thin films buffered by a $SrRuO_3$ layer. J. Am. Ceram. Soc. 91, 463-466 (2008).

[5] C. Gao, X. Meng, J. Sun, J. Ma, T. Lin, and J. Chu. Ferroelectric properties of $BiFeO_3$ thin films prepared via a simple chemical solution deposition. Ferroelectrics 406,137-142 (2010).

[6] S. S. Kim, E. J. Choi, and A. S. Bhalla. Effects of excess bismuth content in

precursor solution on ferroelectric properties of $BiFeO_3$ thin films prepared by a chemical solution deposition. Ferroelectr. Lett. 34, 84-94 (2007).

[7] P. Hansen, K. Witter, and W. Tolksdorf. Magnetic and magneto-optical properties of bismuth-substituted gadolinium iron gadolinium iron garnet films. Phys. Rev. B 27, 4375-4383 (1983).

[8] Y. Chishima, Y. Noguchi, Y. kitanaka, and M. Miyayama. Defect control for polarization switching in $BiFeO_3$ single crystals. IEEE T. Ultrason. Ferr. 57, 2233-2236 (2010).

[9] A. Lahmar, K. Zhao, S. Habouti, M. Dietze, C. Solterbeck, and M. Souni. Off-stoichiometry effects on $BiFeO_3$ thin films. Solid State Ionics 202, 1-5 (2011).

[10] M. K. Singh, H. M. Jang, S. Ryu, and M. Jo. Polarizated Raman scattering of multiferroic $BiFeO_3$ epitaxial films with thombohedral *R*3*c* symmetry. Appl. Phys. Lett. 88, 042907 (2006).

[11] G. Yuan, S. Or, H Chan, and Z. Liu. Reduced ferroelectric coercivity in multiferroic $Bi_{0.825}Nd_{0.175}FeO_3$ thin films. J. Appl. Phys. 101, 024106 (2007).

[12] D. Rout, K. Moon, and S. Kang. Temperature-dependent Raman scattering studies of polycrystalline $BiFeO_3$ bulk ceramics. J. Raman Spectrosc. 40, 618-626 (2009).

[13] Y. Yang, J. Y. Sun, K. Zhu, Y. L. Liu, and L. Wan. Structure properties of $BiFeO_3$ films studied by micro-Raman scattering. J. Appl. Phys. 103, 093532(2008).

[14] H. Fujisawa, M. Shimizu, T. Horiuchi, T. Shiosaki, and K. Matsushige. Investigation of the current path of $Pb(Zr,Ti)O_3$ thin films using an atomic force microscope with simultaneous current measurement. Appl. Phys. Lett. 71, 416 (1997).

[15] J. Miao, L. Cao. J. Yuan, W. Chen, H. Yang, B. Xu, X. Qiu, and B. Zhao. Microstructure dependence of the electrical properties of $(Ba,Sr)TiO_3$ thin film deposited on $(La,Sr)MnO_3$ conductive layer. J. Cryst. Growth 276, 498-506 (2005).

[16] S. Chang and J. Y. Lee. Electrical conduction mechanism in high-dielectric-constant $(Ba_{0.5},Sr_{0.5})TiO_3$ thin films. Appl. Phys. Lett. 80, 655-657 (2002).

[17] G. W. Pabst, L. W. Martin, Y. Chu, and R. Ramesh. Leakage machanisms in $BiFeO_3$ thin films. Appl. Phys. Lett. 90, 072902 (2007).

[18] F. Gao, X.Qiu, Y. Yuan, B. Xu, Y. Wen, F. Yuan, L. Lu, and J. Liu. Effects of substrate temperature on $Bi_{0.8}La_{0.2}FeO_3$ thin films prepared by pulsed laser

deposition. Thin Solid Films 515, 5366-5373 (2007).

[19] N. A. Pertsev, A. G. Zembilgotov, and A. K. Tagantsev. Effect of mechanical boundary conditions on phase diagrams of epitaxial ferroelectric thin films. Phys. Rev. Lett. 80, 1988-1991 (1998).

Chapter 3

$LaNiO_3$ Bottom Electrode and Its Influence on $BiFeO_3$ Structure and Electrical Properties

3.1 Introduction

In Chapter 2, we got the enhanced polarization in Tube 5h- annealed B1.05F films. But the observed largest P_r value is 14.8 μC cm^{-2}, which is smaller than the reported value for polycrystalline BFO prepared by CSD method. Lahmar *et al*. [1] fabricated BFO films on commercial (111)Pt/Ti/SiO_2/Si substrate by CSD and obtained the P_r value of ~50 μC cm^{-2} for BFO with 10% Bi excess. Simoes *et al*. [2] reported the similar results of P_r values. Both of them used the Pt/Ti/SiO_2/Si substrate, which is widely used in CSD method. However, in our study, the difference is that we choose commercial glass substrate, the rate of thermal expansion and contraction of which is similar with Si substrate. But the glass substrate is amorphous and the thermal conductivity of glass substrate (0.1 W m^{-1} K^{-1}) is much smaller than that of Si substrate (149 W m^{-1} K^{-1}). As a result of it, the glass substrate is considered to be helpful for temperature control in comparison with Si substrate. In this case, $LaNiO_3$ is fabricated as bottom electrode on glass substrate by sputtering, due to the good electrical conductivity and lattice match with BFO [3].

$LaNiO_3$ (LNO), which is a pseudocubic perovskite with a lattice parameter of 3.85 Å, has attracted much attention in the past few years, as a conducting layer for applications in ferroelectric memories. [4] The resistivity of LNO is isotropic and low (~225 μΩ cm^{-1} at room temperature) [5], which is comparable to that of $SrRuO_3$. It is well known that perovskite oxide electrodes, such as $SrRuO_3$, $LaNiO_3$, and $BaPbO_3$, effectively improve crystal growth and electric properties of ferroelectric oxide. [6-10]

The specific characteristics of the $LaNiO_3$ electrode are low preparation temperature, good conductivity and chemical stability. [8] Of particular interest, the $LaNiO_3$ electrode is promising to induce the preferred-orientation and improve the film/electrode interface of ferroelectric films, which often dominates the performance of ferroelectric films. [6] As a result of these, in chapter 3, we detected the process conditions for preparing high quality LNO layer on glass substrate and searched the influence of LNO layer on BFO films. We found that the crystallinity of LNO layer play an important role in ferroelectric behavior of BFO films.

3.2 Experiment

3.2.1 Fabrication of $LaNiO_3$ layer on glass

The LNO layer was deposited on glass substrate (Corning Eagle XG, Non-alkaline aluminosilicate glass) by sputtering in a vacuum system with a base pressure lower than 7.5×10^{-6} torr. The total gas pressure is 10 mtorr (O_2 6%). The temperature of substrate is 400 ºC. The thickness of the deposited LNO layer is around 100 nm. In order to investigate the effect of crystallinity of LNO layer on BFO properties, the as-sputtered LNO layer were annealed at 550, 600 and 650 ºC in air by normal furnace for 3 h, with temperature increasing at a rate of 10 ºC min^{-1}.

Table 3.1 Annealing conditions for LNO layers and BFO thin films.

	RTA (ºC)	Normal furnace (ºC)
LNO/glass		550, 600, 650 (3h, at rate of 10 ºC min^{-1})
BFO/LNO/glass	500, 550(10min)	500, 550 (5h)

3.2.2 Deposition of $BiFeO_3$ on $LaNiO_3$/glass

The deposition of BFO films on LNO layers followed the steps shown in section 2.2. Precursor solutions with stoichiometric (BF) and 5% (B1.05F), 10% (B1.1F) mole ratios of excess Bi were prepared. BFO films were fabricated by spin-coating onto LNO/glass and further heat-treatment. The films were annealed at 500 and 550 ºC for crystallization using rapid thermal annealing (RTA, temperature rise up in 1

min and keep 10 min) and normal furnace (Tube 5h, quickly push into the pre-heated furnace and keep 5 h). The details are shown in Table 3.1

3.2.3 Measurement

X-ray diffraction (XRD) was carried out for structure detection by using Rigaku-Smartlab. Atomic force microscopy (AFM) was used for surface morphology evaluation. For electric measurement, we prepared Au top electrode (200 μm diameter) by sputtering onto BFO/LNO/glass. Leakage current behaviors were estimated by using Keithley 230 voltage source and Keithley 6487picoammeter. The applied voltage was swept from 0 V to 4 V, and from 4 V to -4 V, and from -4 V to 0 V, at a rate of 0.1 V s^{-1}. The polarization hysteresis was measured at a frequency of 5 kHz at room temperature by using ferroelectric test system FCE-1.

3.3 Results and discussion

3.3.1 Structure and morphology of $LaNiO_3$ bottom electrodes

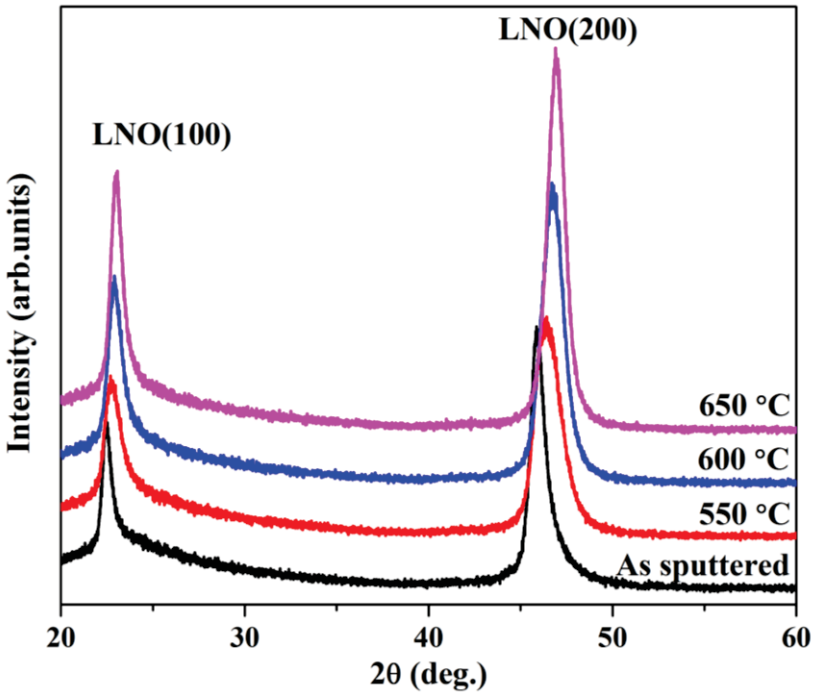

Figure 3.1 XRD patterns of LNO layers, annealed at different temperature.

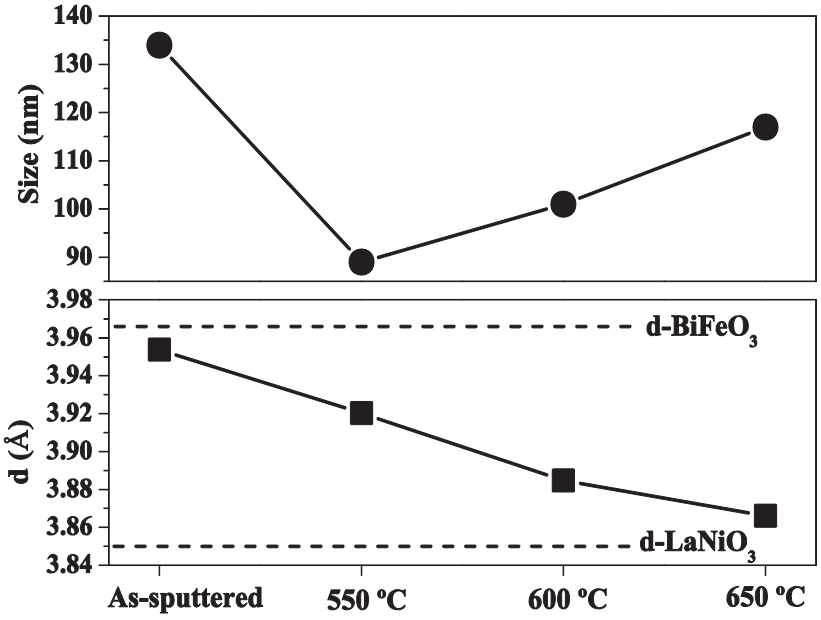

Figure 3.2 Calculated grain size and *d*-spacing value for LNO layers.

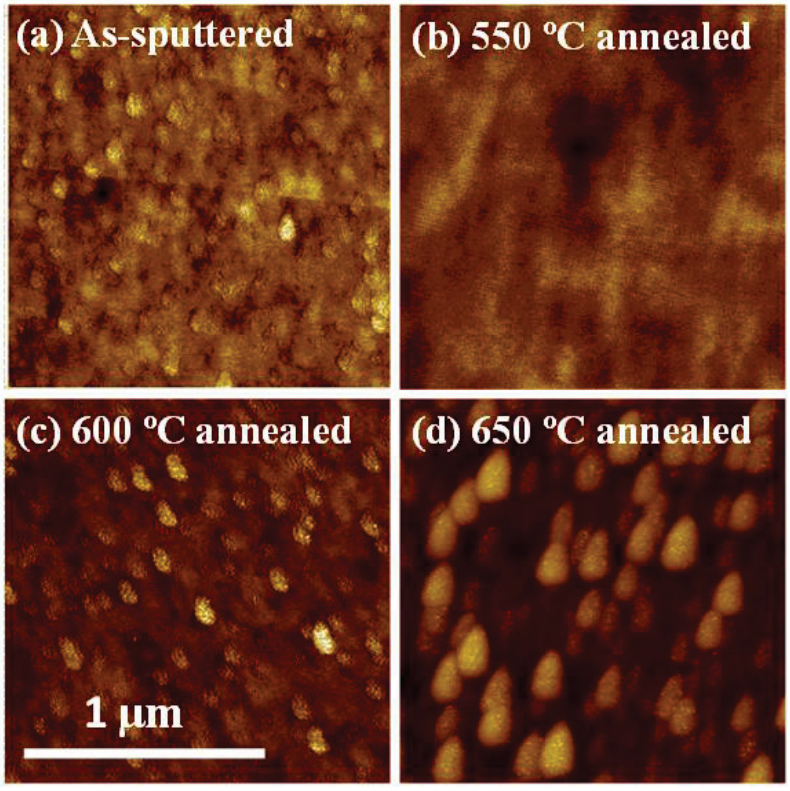

Figure 3.3 AFM images for **(a)** as-sputtered, **(b)** 550 ºC, **(c)** 600 ºC, and **(d)** 650 ºC annealed LNO.

Figure 3.1 shows the XRD patterns of LNO layers, in which the (00*l*)-oriented growth is detected. It is clear that with raising annealing temperature, the diffraction

peaks shift somewhat to right accompanied by the increment of peak intensities. It indicates the decrease of *d*-spacing and enhanced crystallinity. The calculated *d* value and grain size are shown in Figure 3.2. The as-sputtered LNO layer shows the largest grain size and the largest *d*-spacing. For the annealed LNO layers, with raising annealing temperature, grain size increases while *d*-spacing decreases contrarily.

The surface morphology of LNO layers are shown in AFM images in Figure 3.3. 650 ºC-annealed sample (Figure 3.3(d)) shows clear crystal grain with size around 120 nm, which matches well with the calculated particle size from XRD curves.

3.3.2 Stoichiometric $BiFeO_3$ on $LaNiO_3$ bottom electrodes

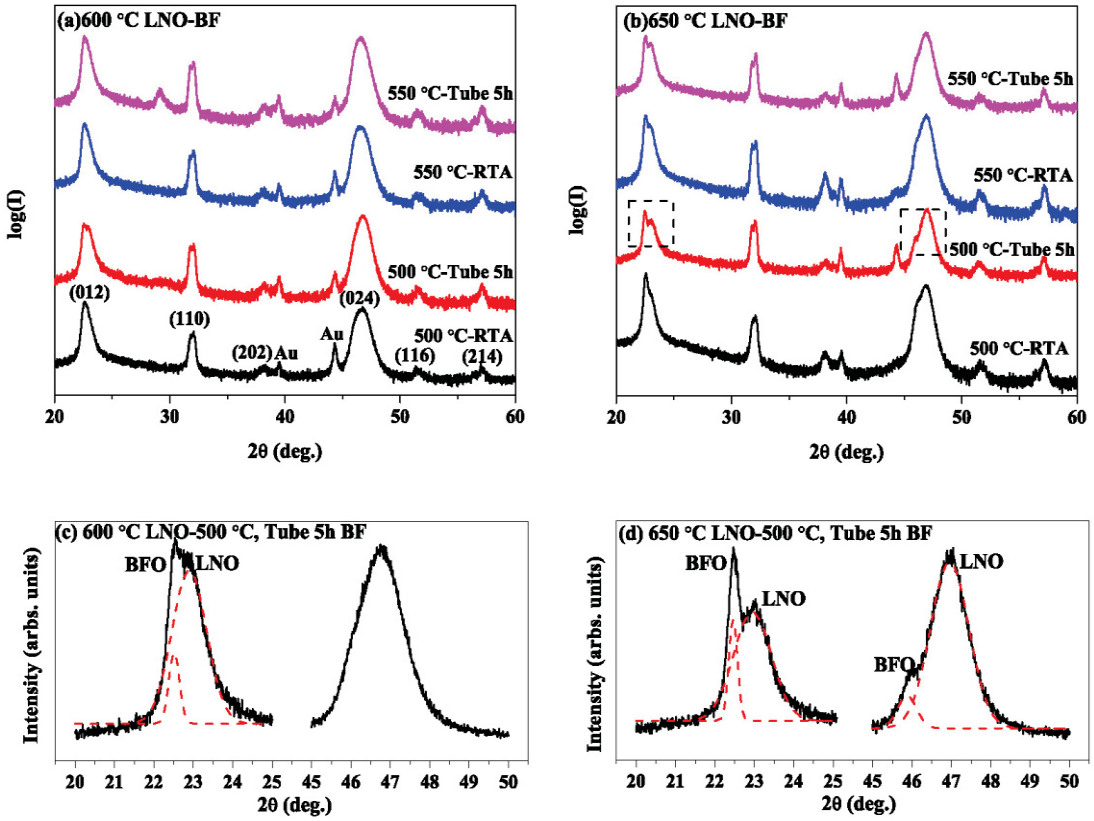

Figure 3.4 XRD patterns of BFO films deposited on **(a)** 600 ºC- and **(b)** 650 ºC- annealed LNO layers; partially enlarged XRD curves(20º-25º for (100) plane and 45º-50º for (200) plane) and linear fitting for 500 ºC-Tube 5h annealed BFO films deposited on **(c)** 600 ºC- and **(d)** 650 ºC-annealed LNO layers.

In Chapter 2, the used LNO bottom electrodes were annealed at 550 ºC for crystallization, which was not the optimal temperature proved by XRD and AFM results. As a result of that, 600- and 650 ºC- annealed LNO layers were usded as bottom electrodes for deposition stoichiometric BFO (BF) films, respectively. Considering the using of LNO bottom laryers is abel to effectively improve crystal growth of top BFO films, we reduced the annealing temperature of BFO/LNO/glass to 500 ºC. After fabrating BFO films, Au top electrode was sputterred on BFO films for electrical measurement. The XRD patterns of Au/BFO/LNO/glass substrate are shown in Figure 3.4.

As discussed in setion 2.3.1 that, stoichiometirc BFO prepared on glass substate just keeps γ-Bi_2O_3 phase after annealing at 500 ºC. But as seen in Figure 3.4 (a) and (b) that the BFO/LNO/glass annealed at 500 ºC show pure *R*3*c* BFO phase, without any other phase can be detected. It demonstrates that the using of LNO underlayer reduces the crystallization temperature of top BFO films. The matched lattice parameter between BFO and LNO is considered to be able to lower the driving force for crystallization process, which makes it possible to get pure BFO phase at lower temperature. It is an important discovery that we can obtain pure phase BFO at low temperature, keeping an advantage of preventing Bi vacancies which is easy to form at high temperature.

Figure 3.4(c) and (d) show the partial enlarged curves for 500 ºC-Tube 5h annealed BFO on 600 ºC- and 650 ºC- annealed LNO, respectively. Compared with BFO on 600 ºC- annealed LNO, the BFO on 650 ºC- LNO shows clear and sharp (012) BFO peak, indicating better crystallinity.

The *J-E* properties of synthesized samples are measured at room temperature and shown in Figure 3.5. Increasing annealing temperature from 500 ºC to 550 ºC, makes leakage current increased one order of magnitude. The grain growth [11] (Figure 3.6) and increased Bi vacancies can respond for it. Figure 3.7 shows the *J-E* curves of 550 ºC-Tube 5h annealed BFO films on LNO layers that annealed at different temperatures. Film deposited on 550 ºC-annealed LNO shows the largest leakage current. It indicates that the crystallinity of bottom LNO layer takes an important role in the leakage current of top BFO film.

Figure 3.8 shows the *P-E* curves of two groups of samples. For BFO on 600 ºC-LNO (Figure 3.8(a)), all the samples show saturated polarization, and samples

annealed at 550 ºC shows larger P_r value than that of 500 ºC annealed samples. The largest P_r value of 15.3 μC cm^{-2} is detected for 550 ºC-Tube 5h annealed sample. This value is closed to the obtained largest P_r value in Chapter 2 (14.8 μC cm^{-2} for B1.05F, doposited on 550 ºC- LNO and annealed by tube for 5 h). For BFO on 650 ºC- LNO (Figure 3.8(b)), an amazing huge polarization of 120 μC cm^{-2} is observed from 500 ºC-Tube 5h annealed film.

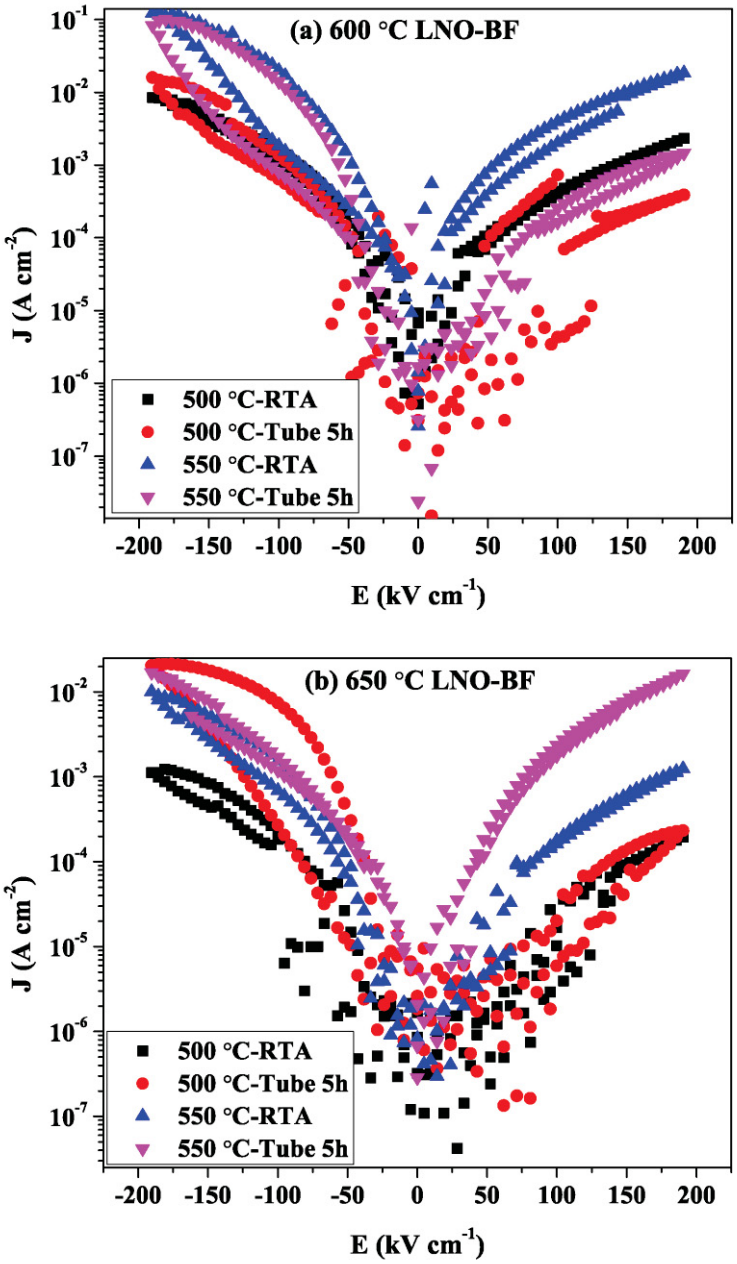

Figure 3.5 *J-E* curves of BFO on **(a)** 600 ºC and **(b)** 650 ºC annealed LNO layers, measured at room temperature.

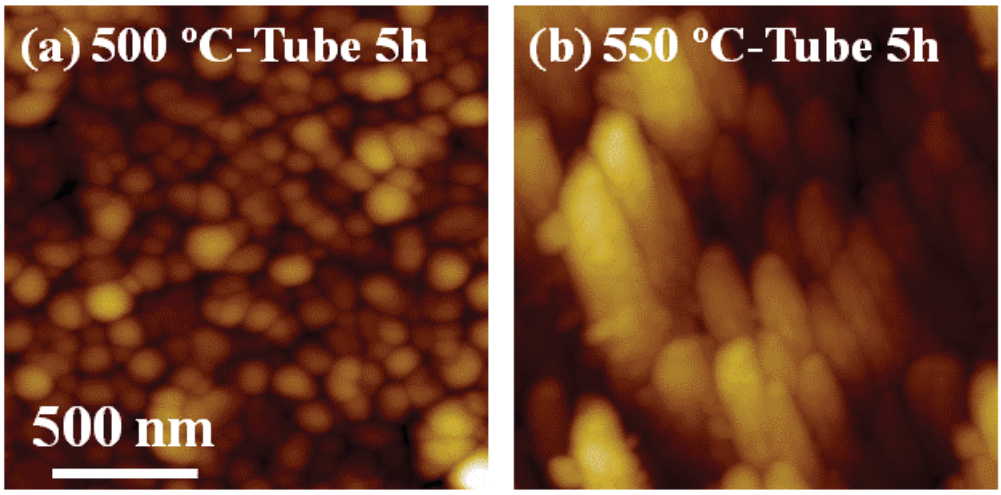

Figure 3.6 AFM images for BFO sample on 650 ºC-LNO, annealed by normal tube furnace for 5h at **(a)** 500 C and **(b)** 550C.

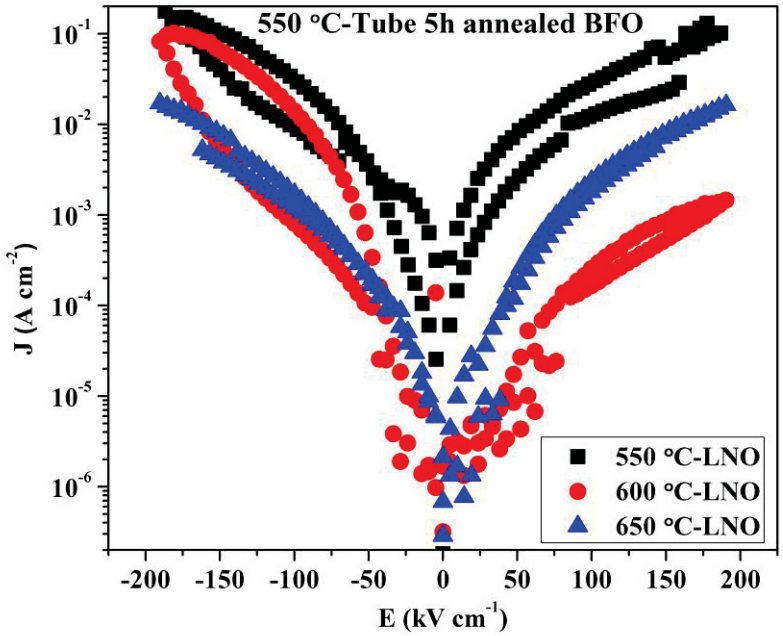

Figure 3.7 *J-E* curves of BFO films annealed at 550 ºC for 5h on LNO layers that annealed at different temperatures.

Figure 3.9 show the *P-E* curves of BFO annealed by tube for 5 h at (a) 500 ºC and (b) 550 ºC, deposited on LNO layers that annealed at different temperatures. For 550 ºC- annealed BFO (Figure 3.9(b)), films deposited on 600 ºC- and 650 ºC- LNO show similar saturated loops with good squareness. However, at lower annealing temperature of 500 ºC, as shown in Figure 3.9(a), film on 650 ºC- LNO shows

extremly larger P_r value than film on 600 ºC- LNO. It is easy to understant that the enhanced polarzaiton is due to less defects achieved by low-temperature annealing. As determinated in Chapter 2 that structure with less defects can be strained without relaxation, which will lead to higher in-plane distortion and enhanced polarization. However, it is confused that the BFO films on 600 ºC- and 650 ºC- LNO show quite different polarization behavior after low-temperature annealing. We suggest the crystallinity of BFO films takes influence on it, but the reason is not clear yet.

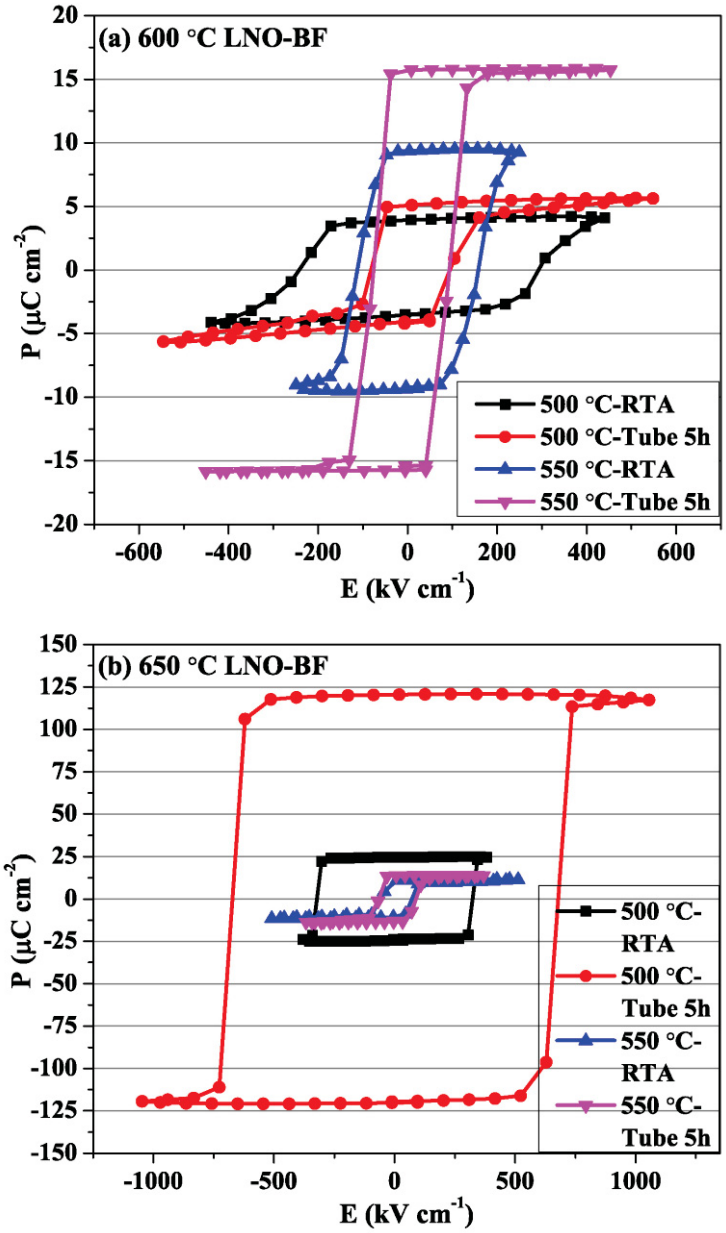

Figure 3.8 *P-E* curves of BFO on **(a)** 600 ºC and **(b)** 650 ºC annealed LNO layers, measured at room temperature at 5 kHz.

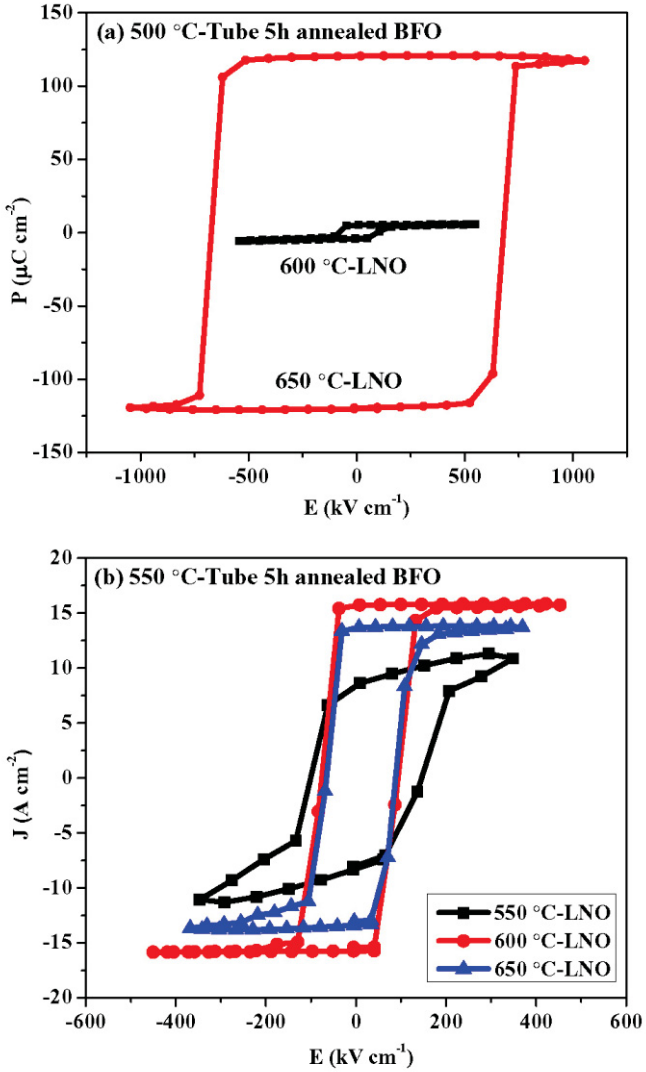

Figure 3.9 *P-E* curves of BFO annealed by tube for 5 h at **(a)** 500 ºC and **(b)** 550 ºC, deposited on LNO layers that annealed at different temperatures.

3.3.3 $BiFeO_3$ with excess Bi on $LaNiO_3$ bottom electrodes

Considering the results shown in Chapter 2 that BFO with 5 mol% excess Bi shows the largest P_r value, we deposited BFO films with excess Bi (5 and 10 mol%) on 650 ºC-LNO. All the samples crystallize in *R*3*c* phase BFO. As shown in Figure 3.10(c) and (d) that, with increasing the amount of excess Bi from 5 to 10 mol%, the (012) peak intensity of BFO shifts to higher angle, indicating the decrease of vacancy-defects in crystal structure. For stoichiometric BFO film, in Figure 3.4(d), the (012) peak is detected at 22.47 º, indicating the presence of Bi vacancies.

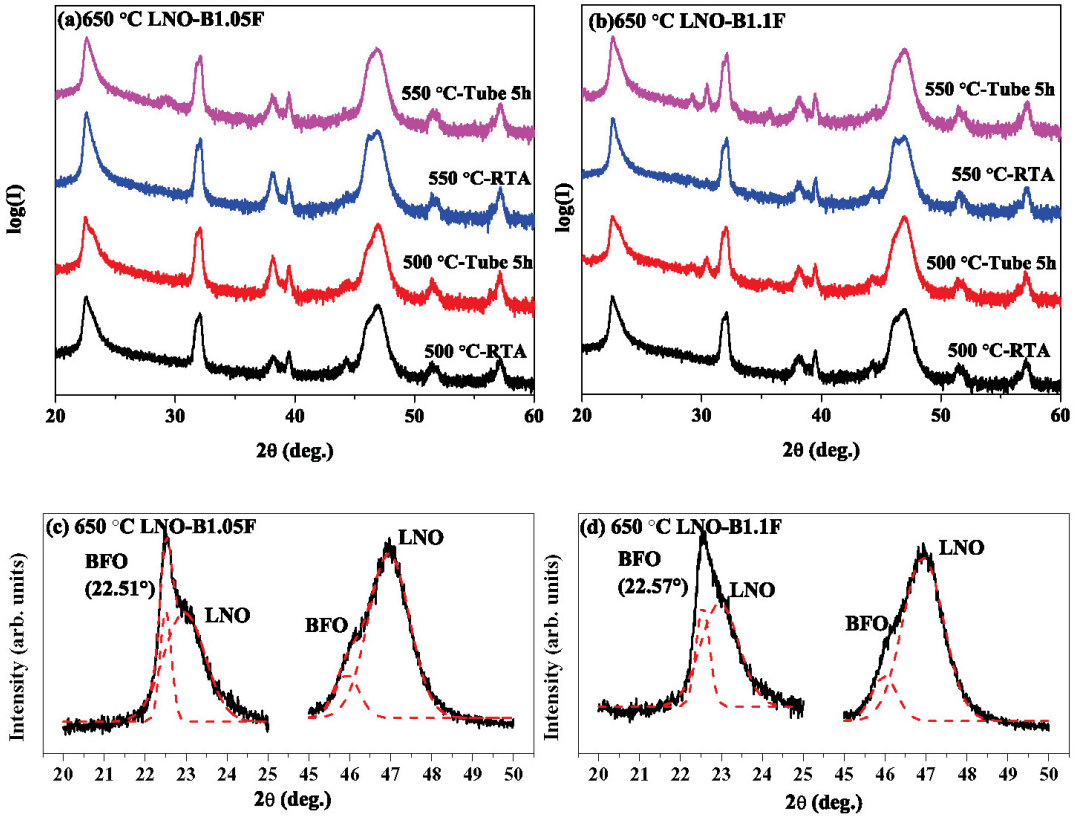

Figure 3.10 XRD patterns of **(a)** B1.05F and **(b)** B1.1F deposited on 650 ºC annealed LNO layers; partially enlarged XRD curves(20º-25º for (100) plane and 45º-50º for (200) plane) and linear fitting for Tube 5h-500 ºC annealed **(c)** B1.05F and **(d)** B1.1F.

The *J-E* curves of BFO with excess Bi are shown in Figure 3.11. There are similar tendencies in these two groups. With increasing annealing temperature, the leakage current increases. 550 ºC-RTA annealed samples show the highest leakage current. Moreover, as shown in Figure 3.12, BF film shows higher leakage current than that of B1.05 and B1.1F films. The presence of defects, such as Bi vacancies can account for them.

The hysteresis loops are shown in Figure 3.13, measured at room temperature at 5 kHz. For B1.05F, which is suggested keeping the least vacancies, the saturated hysteresis loops are observed except for the 550 ºC-RTA annealed sample. For B1.1F, the 500 ºC-Tube 5h annealed sample shows huge remnant polarization of 142 μC cm^{-2}, which is close to the largest P_r value that has been reported for BFO films. It can be noticed that the 500 ºC-Tube 5h annealed samples show the best polarization behaviour. As we discussed in Chapter 2, in-plane strain makes great influence on

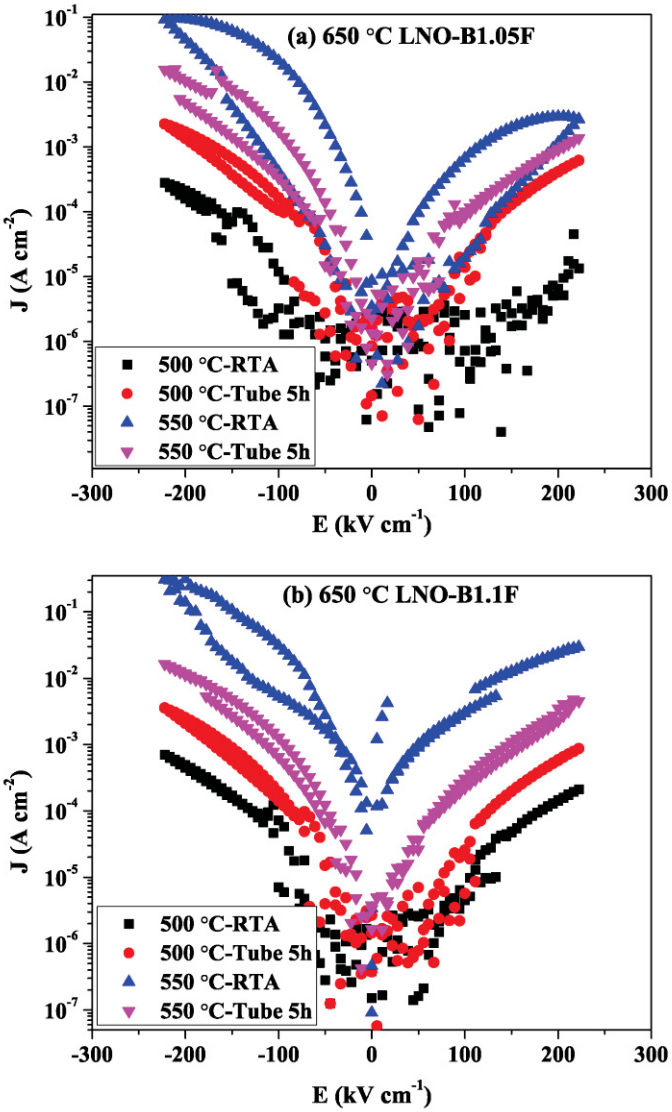

Figure 3.11 *J-E* curves of **(a)** B1.05F and **(b)** B1.1F on 650 ºC annealed LNO layers, measured at room temperature.

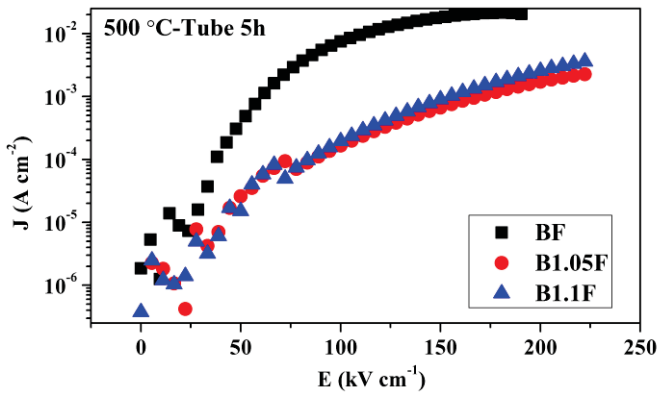

Figure 3.7 *J-E* curves of BFO films with different amounts of excess Bi annealed at 500 ºC for 5h by tube (on 650 ºC- LNO bottom electrodes).

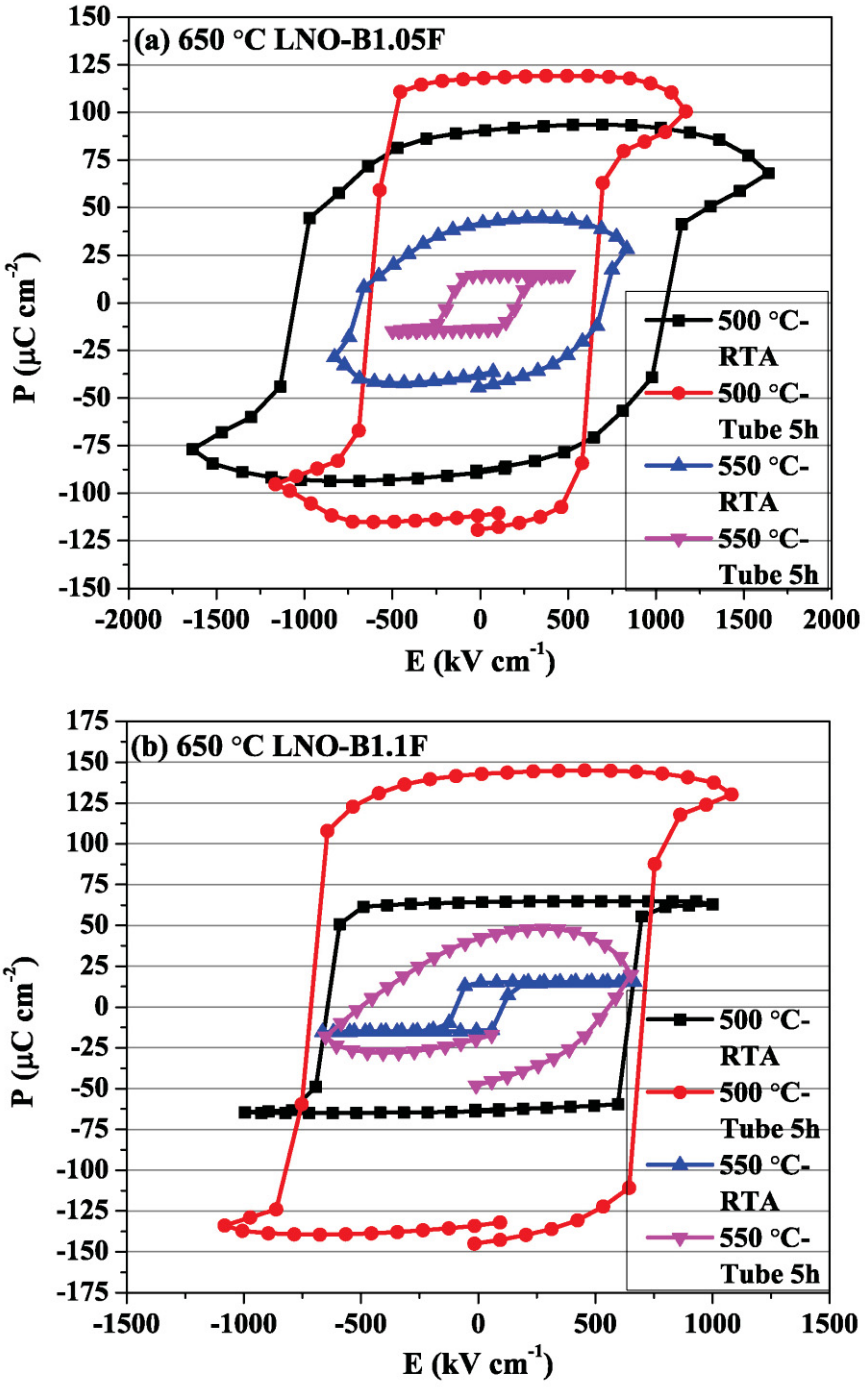

Figure 3.8 *P-E* curves of **(a)** B1.05F and **(b)** B1.1F on 650 ºC annealed LNO layers, measured at room temperature at 5 kHz.

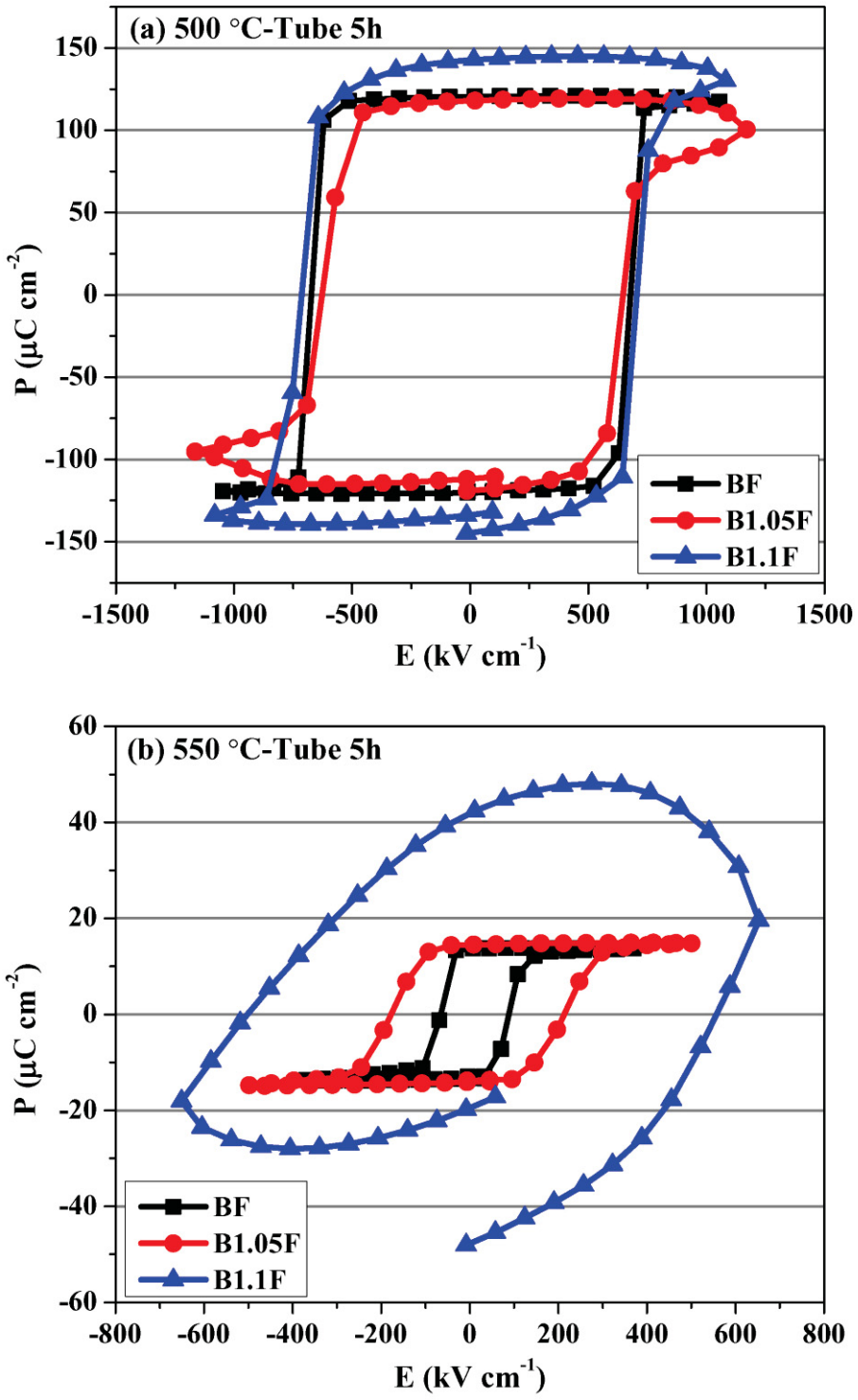

Figure 3.14 *P-E* curves of BFO films on 650 ºC- LNO layers, annealed by tube for 5 h at **(a)** 500 ºC and **(b)** 550 ºC.

polarization, while strain is mainly affected by crystallinity and defects. Annealing at 500 ºC is benefit for preventing Bi evaporation while annealing for a long time improves the crystallinity. As a result of these, the in-plane strain is more efficiently enhanced after 500 ºC-Tube 5h annealing. Thus it is feasible that 500 ºC-Tube 5h annealed samples show the huge polarization value.

For comparison, the *P-E* curves for BFO films on 650 ºC- LNO layers are grouped by annealing temperatures, as shown in Figure 3.14. The polarization behavior greatly changes by raising annealing temperature from 500 ºC to 550 ºC. It means that the heat treatment is an important factor for crystallization and polarization of thin films.

3.4 Conclusions

$LaNiO_3$ bottom electrodes play an important role in the structure and polarization properties of top BFO films. 650 ºC-annealed LNO layer shows better crystallinity, offering a condition for growing high quality BFO film on it. 500 ºC-Tube 5h annealed B1.1F, which is deposited on 650 ºC-annealed LNO, shows the largest P_r value of 142 μC cm^{-2}, attributed to the high in-plane strain achieved by long-time and low-temperature annealing.

References

[1] A. Aahmar, K. Zhao, S. Habouti, M. Dietze, C. H. Solterbeck, and M. E.-Souni. Off-stoichiometry effects on $BiFeO_3$ thin films. Solid State Ionics 202, 1-5 (2011).

[2] A. Z. Simoes, A. H. M. Gonzalez, L. S. Cavalcante, C. S. Riccardi, E. Longo, and J. A. Varela. Ferroelectric characteristics of $BiFeO_3$ thin films prepared via a simple chemical solution deposition. J. Appl. Phys. 101, 074108 (2007).

[3] L. Wan, Y. Li, X. Meng, J. Sun, X. Yuan, J. Shangguan, and J. Chu. Observation of antiphase domains in $BiFeO_3$ thin films by X-ray diffraction. Phys. B 391, 124-129 (2007).

[4] X. Meng, J. Sun, J. Yu, H. Ye, S. Guo, and J. Chu. Preparation of highly (100)-oriented metallic $LaNiO_3$ films on Si substrates by a modified metalorganic decomposition technique. Appl. Surf. Sci. 171, 68-70 (2001).

[5] A. Wold, B. Post, and E. Banks. Rare earth nickel oxides. J. Am. Chem. Soc. 79, 4911-4913 (1957).

[6] Y. Lee, J. Wu, Y. Chueh, and L. Chou. Low-temperature growth and interface characterization of $BiFeO_3$ thin films with reduced leakage current. Appl. Phys. Lett. 87, 172901 (2005).

[7] B. Nagaraj. S. Aggarwal, and R. Ramesh. Influence of contact electrodes on leakage characteristics in ferroelectric thin films. J. Appl. Phys. 90, 375 (2001).

[8] M. Chen, T. Wu, and J. Wu. Effect of textured $LaNiO_3$ electrode on the fatigue improvement of $Pb(Zr_{0.53}Ti_{0.47})O_3$ thin films. Appl. Phys. Lett. 68, 1430 (1996).

[9] Y. Luo and J. Wu. $BaPbO_3$ perovskite electrode for lead zirconate titanate ferroelectric thin films. Appl. Phys. Lett. 79, 3669 (2001).

[10] C. Liang, J. Wu, and M. Chang. Ferroelectric $BaPbO_3/PbZr_{0.53}Ti_{0.47}/BaPbO_3$ heterostructures. Appl. Phys. Lett. 81, 3624 (2002).

[11] H. Fujisawa, M. Shimizu, T. Horiuchi, T. Shiosaki, and K. Matsushige. Investigation of the current path of $Pb(Zr,Ti)O_3$ thin films using an atomic force microscope with simultaneous current measurement. Appl. Phys. Lett. 71, 416 (1997).

Chapter 4

Phase Transition and Electrical Properties of $BiFe_{1-x}Al_xO_3$ Thin Films

4.1 Introduction

Many physical properties of materials may vary significantly with a small change of chemical composition through doping or substitution of impurities. The chemical substitution for BFO has been widely investigated to improve ferroelectric properties of BFO. [1-4]

In BFO system, oxygen vacancies are mainly originated from loss of Bi during vacuum process or heat treatment. Due to the variable valence state of Fe (+2 and +3), the hopping of electron from Fe^{2+} to Fe^{3+} plays an important role in electric conduction.[5] In order to enhance the ferroelectric properties, many authors have already reported chemical substitution on the A and/or the B site of $BiFeO_3$, the goal of which is to alter the Fe environment.[6] Singh *et al*. [7] prepared Cr-doped BFO films and suggested that the stable Cr^{3+} ions would control the volatile nature of Fe^{3+} ions and reduce the formation of Fe^{2+} ions. Doping of Mn and Ti atoms were also documented of successfully reducing the formation of Fe^{2+}, resulting in the reduced leakage current. [2-4] Moreover, the changes of ferroelectric behavior were generally accounted for the reduced leakage current by substitution.

Besides the influence on leakage current, chemical substitution can make change of crystal structure via the "chemical pressure", an alternative way of inducing pressure like strain. [8, 9] It is known that Bi^{3+} with stereochemically active $6s^2$ lone pair electrons takes a main contribution for ion off-centering which will induce ferroelectric polarization.[10] However, recently, Zhang *et al*.[11] indicated that a large

Fe-ion displacement from the relative negative charge center induced by epitaxy was the mechanism for the large polarization in the tetragonal-like BFO phase. Thus, the substitution-induced structure change seems attractive. Will structure distortion induced by substitution be able enhance the polarization?

In the range of chemical substitution for BFO, aluminum has never been chosen, although Al^{3+} ion has a definite oxidation state as Cr^{3+}. Moreover the ionic radius of Al^{3+} (0.535 Å) is smaller than that of Fe^{3+} (0.645 Å), which is considered to bring larger perovskite tolerance factor by Al substitution on Fe-site (see section 1.3).

$BiAlO_3$ (BAO) has a similar structure to $BiFeO_3$ with octahedrally coordinated Al^{3+} ions. Bulk $BiAlO_3$ has *R*3*c* symmetry with *a*=5.38 Å and *c*=13.40 Å, which is smaller than that of *R*3*c* $BiFeO_3$ (*a*=5.58 Å and *c*=13.87 Å). The theoretical study showed that the ferroelectric polarization of BAO should be 75.6 μC cm^{-2} along [111] direction, which was a high-performance ferroelectric. [12,13] Son *et al*. [14] reported an epitaxial BAO films on (001) $SrRuO_3$/ (100) $LaAlO_3$ substrate prepared by PLD. The sample exhibited the remanent polarization of 29 μC cm^{-2}, which was quite smaller than theoretical value. Meanwhile, limited by the extreme preparation conditions of BAO, such as high pressure and high temperature, there were few practical studies focusing on BAO.

In this study, we prepared Al-doped BFO thin films ($BiFe_{1-x}Al_xO_3$, BFAO) via chemical solution deposition (CSD) method and detected the influence of Al doping on BFO structure, phase transition and electrical properties. From that, it is possible to guide synthesis of novel and greatly improved materials.

4.2 Experiment

4.2.1 Precursor solution

The $BiFe_{1-x}Al_xO_3$ (x=0, 0.1, 0.2, 0.3 and 0.4, BF1-xAxO) thin films were prepared via CSD method. The starting reagents were bismuth nitrate ($Bi(NO_3)_3 \cdot 5H_2O$, 99.5%), ferric nitrate ($Fe(NO_3)_3 \cdot 9H_2O$, 99%) and aluminum nitrate ($Al(NO_3)_3 \cdot 9H_2O$, 99.5%). They were dissolved in acetic acid ($C_2H_4O_2$, 99.7%) according to stoichiometry by stirring under heating. An appropriate amount of acetylacetone ($C_5H_8O_2$, 99%) was added into the solution as a chelating agent. The concentration of

precursor solutions was 0.2 mol L^{-1}.

4.2.2 Films deposition

The solution was spin-coated onto glass substrate or Si (100) substrate, followed by pre-heating at 180 ºC and heating at 380 ºC for 3 min to remove the solvent and decompose the nitrates, respectively. The films were annealed for crystallization using rapid thermal annealing (RTA, temperature rise up in 1 min and keep 10 min) and normal furnace (Tube 5h, quickly push into the pre-heated furnace and keep 5h). For ferroelectric measurement, we also fabricated BFAO films on LNO layer, which was prepared by sputtering and annealed at 650 ° C for 3 h by normal furnace (see section 3.2.1). Details for annealing process are shown in Table 4.1.

Table 4.1 Conditions for annealing process of BFAO films

	Glass substrate	Si(100) substrate	LNO/glass
RTA (ºC)	500, 550, 600, 650	600, 700, 800, 900	500, 550
Tube 5h(ºC)			500, 550

4.2.3 Measurement

X-ray diffraction measurement was used to characterize structure properties at room temperature (Cu *Kα* radiation, Rigaku-Smartlab). Raman spectra were measured at room temperature without polarization (JASCO NRS-3300). AFM images were collected to describe the morphology of thin films surface. For electric measurement, we prepared Au top electrode (200 μm diameter) by sputtering onto BFO/LNO/glass. Leakage current behaviors were estimated using Keithley 230 voltage source and Keithley 6487picoammeter. The applied voltage was swept from 0 V to 4 V, and from 4 V to -4 V, and from -4 V to 0 V, at a rate of 0.1 V s^{-1}a ferroelectric test system. The polarization hysteresis was measured at a frequency of 5 kHz at room temperature by using ferroelectric test system FCE-1.

4.3 Results and Discussion

4.3.1 Phase transition of $BiFe_{1-x}Al_xO_3$ films

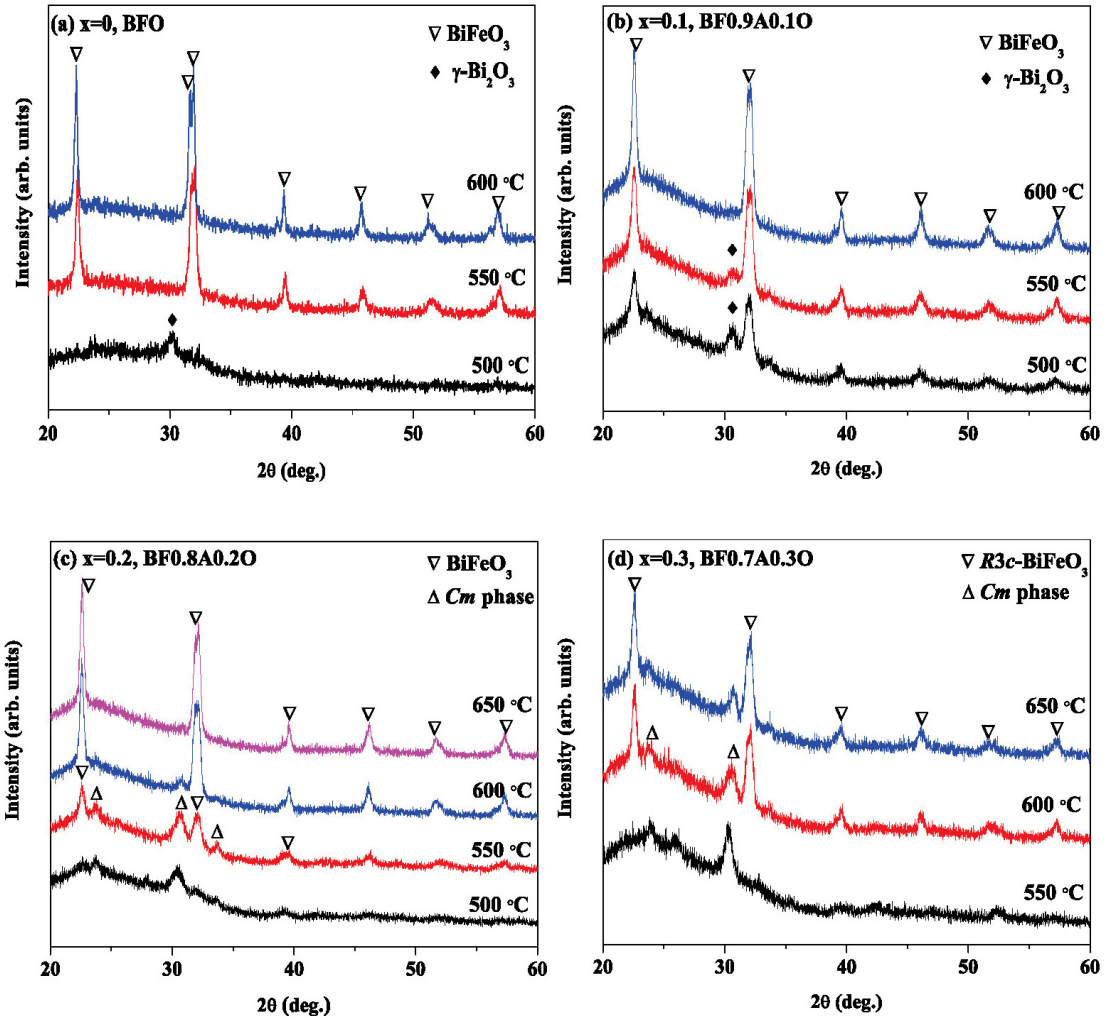

Figure 4.1 XRD patterns of BF1-xAxO on glass for **(a)** x=0, **(b)** x=0.1, **(c)** x=0.2, and **(d)** x=0.3.

Figure 4.1 shows the XRD patterns of BFAO films deposited on glass substrate and annealed at different temperatures. The synthesized pure BFO thin films keep perovskite structure with rhombohedral distorted. Especially the sample annealed at 600 ºC shows obvious split peaks of (104) and (110) which are considered as characteristic for *R*3*c* BFO. For BF0.9A0.1O as shown in Figure 4.1 (b), Bi_2O_3 appears as the second phase after annealing at 500 and 550 ºC, while sample annealed at 600 ºC shows single phase. It suggests that Al doping will increasing

crystallization temperature for *R*3*c*-BFAO. In Figure 4.1(c), BF0.8A0.2O shows other peaks around 24, 30 and 34º after annealing at 550 ºC, which can be denoted in *Cm* phase of BFO. As shown in Figure 4.2, the XRD pattern of BF0.8A0.2O matches perfectly with the calculated data of *Cm* phase (for lattice parameters *a*=0.5325 nm, *b*=0.5316 nm, *c*=0.4635 nm and *β*=91.306 º by using the structural parameters given in the literature [15]) and PCPDF data of *R*3*c* phase. It indicates the co-existence of *R*3*c* and *Cm* phase at x=0.2. However, the *Cm* phase is not stable at high temperate. With increasing annealing temperature to 600 ºC, pure *R*3*c* phase appears. With increasing Al concentration to 0.3, the stable region for *Cm* phase extends (550-650 ºC). 650 ºC- annealed BF0.7A0.3O shows mixture phase of *R*3*c* and *Cm*.

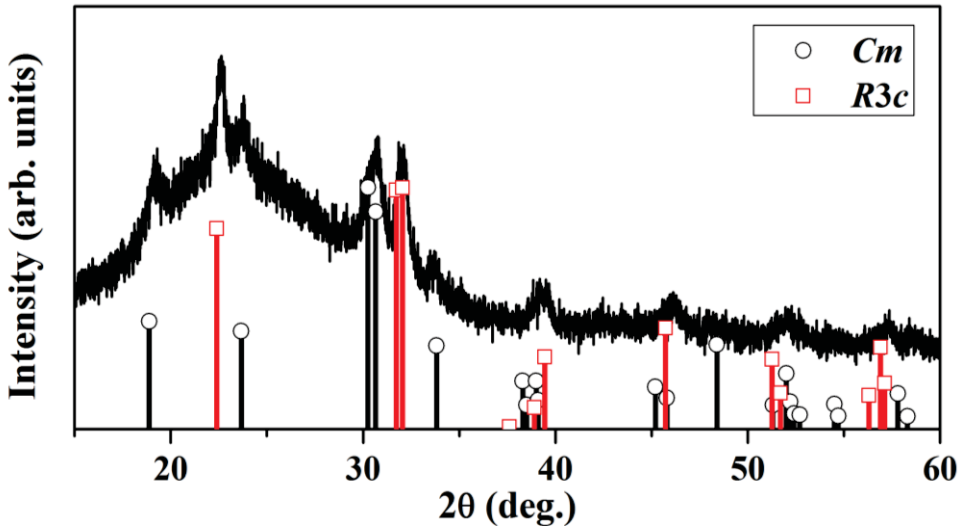

Figure 4.2 Comparison of XRD pattern for 550 ºC-RTA annealed BiFe0.8Al0.2O/glass with calculated diffraction data for the *Cm* phase and PCPDF data of *R*3*c* phase.

The phase diagram of similar solid solution $BiGa_{1-x}Al_xO_3$ has been given by the previous work though it is for powders prepared via the high-pressure (6 GPa) and high-temperature (1373-1473 K) method. [16] It is reported that this system has a pyroxene-type structure ($BiGaO_3$, x=0) with space group *Pcca* and a perovskite structure ($BiAlO_3$, x=1.0) with space group *R*3*c* as end members. Within the experimental composition range (x=0.25, 0.5, 0.75), this system shows a specific phase with both $BiGaO_3$- and $BiAlO_3$- type structure, which has been indexed in a monoclinic system with space group *Cm* (similar to the $PbTiO_3$-type perovskite structure with space group *P*4*mm*). [15, 17]

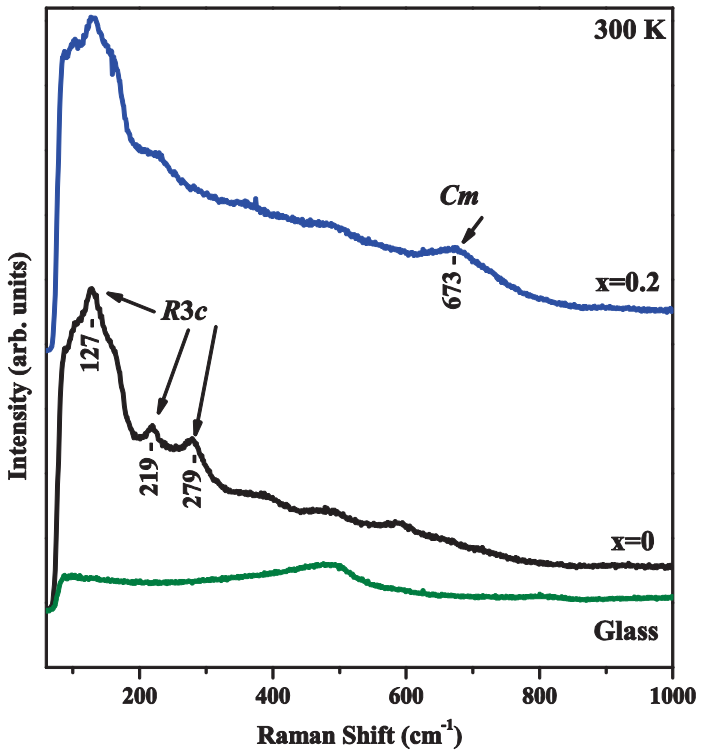

Figure 4.3 Raman spectra of 550 ºC-RTA annealed BFO/glass and BF0.8A0.2O/glass, collected at room temperature.

Raman spectra give evidence for the presence of *Cm* phase. For BFO, Raman shifts for rhombohedral symmetry can be detected. The peaks at 127 and 219 cm^{-1} can be denoted as A_1 modes, while peak at 279 cm^{-1} is due to *E* mode for active modes of the rhombohedral BFO ($\Gamma=4A_1+9E$). For BF0.8A0.2O, a broad peak appears at 673 cm^{-1}. It is the distinctive characteristic of the *T*-like monoclinic phase, which doesn't present in rhombohedral phase. [18, 19] It suggests the co-existence of *R3c* and *Cm* phases clearly.

In our study, the *Cm* phase was obtained under low temperature and normal atmospheric pressure, which is different from the reported essential condition of high-temperature and high-pressure. The formation of *Cm* phase at low temperature of 773 K under normal atmospheric pressure is likely associated with strain induced in the film formation. The strain is derived from the difference of thermal expansion coefficient between film (10.9×10^{-6} $ºC^{-1}$ for BFO [20]) and substrate (3.17×10^{-6} $ºC^{-1}$), reaching an order of GPa by estimated assuming thermal expansion coefficient and typical values of Young modulus (~195 GPa) and Poisson's ratio (~0.3) for ferrite. [21] The film suffers in-plane tensile stress from the glass substrate that has a smaller

thermal expansion coefficient. This tensile stress expands the lattice volume and lowers formation energy of crystal phase that has larger unit cell volume. Thus, it is natural that the tensile stress assists the transition to *Cm* phase with larger unit cell volume than *R*-phase. In this case, the thermal stability of the produced *Cm* phase at the preparation temperature is required. As the *Cm* phase is reported to be stable below 873 K, our preparation temperature satisfies this limitation. Moreover, with increasing Al concentration, the chemical pressure arisen from substitution increases, inducing higher crystal distortion and appearance of *Cm* phase. However, the detailed origin for formation of the *Cm* phase is not yet clear.

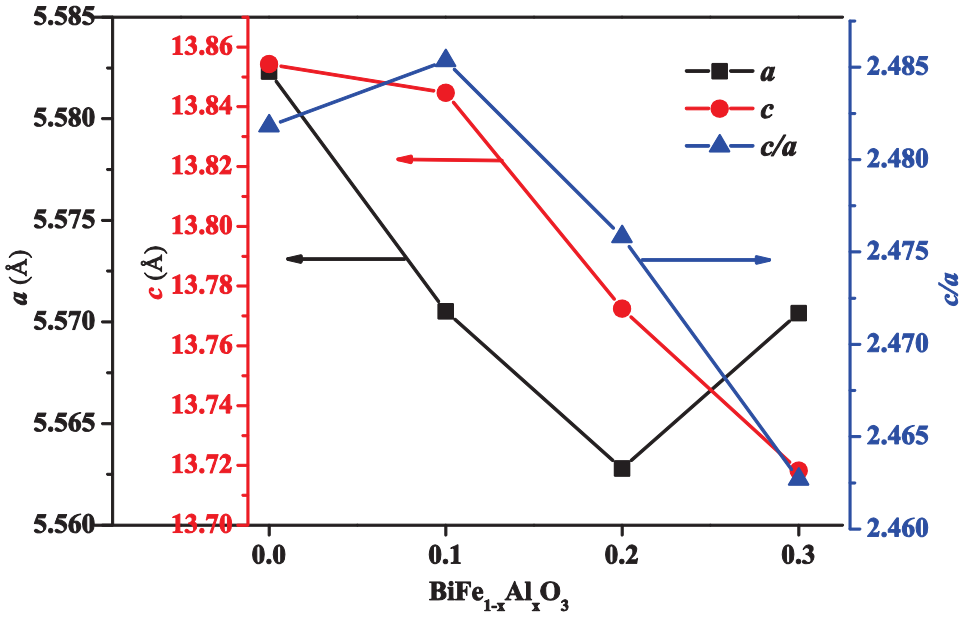

Figure 4.4 The calculated lattice parameters for BFAO films annealed at 600 ºC.

The parameters of samples annealed at 600 ºC are calculated by the whole powder pattern fitting (WPPF) method and plotted in Figure 4.4. When x≤0.2, there is a rough tendency that the lattice constant decreases with increasing Al concentration, which can be explained by the smaller ion radius of Al^{3+} (0.535 Å) compared with that of Fe^{3+} (0.645 Å). For x=0.3, the *a* value increases, perhaps due to the existence of *Cm* phase which keeps larger unit cell volume than *R*3*c* phase.

In order to detect the crystallization property of BFAO at temperature higher than 650 ºC, thin films were deposited on Si (100) substrate which can be heated at higher temperature. Pure BFO is not stable at high temperature known from Figure 4.5(a).

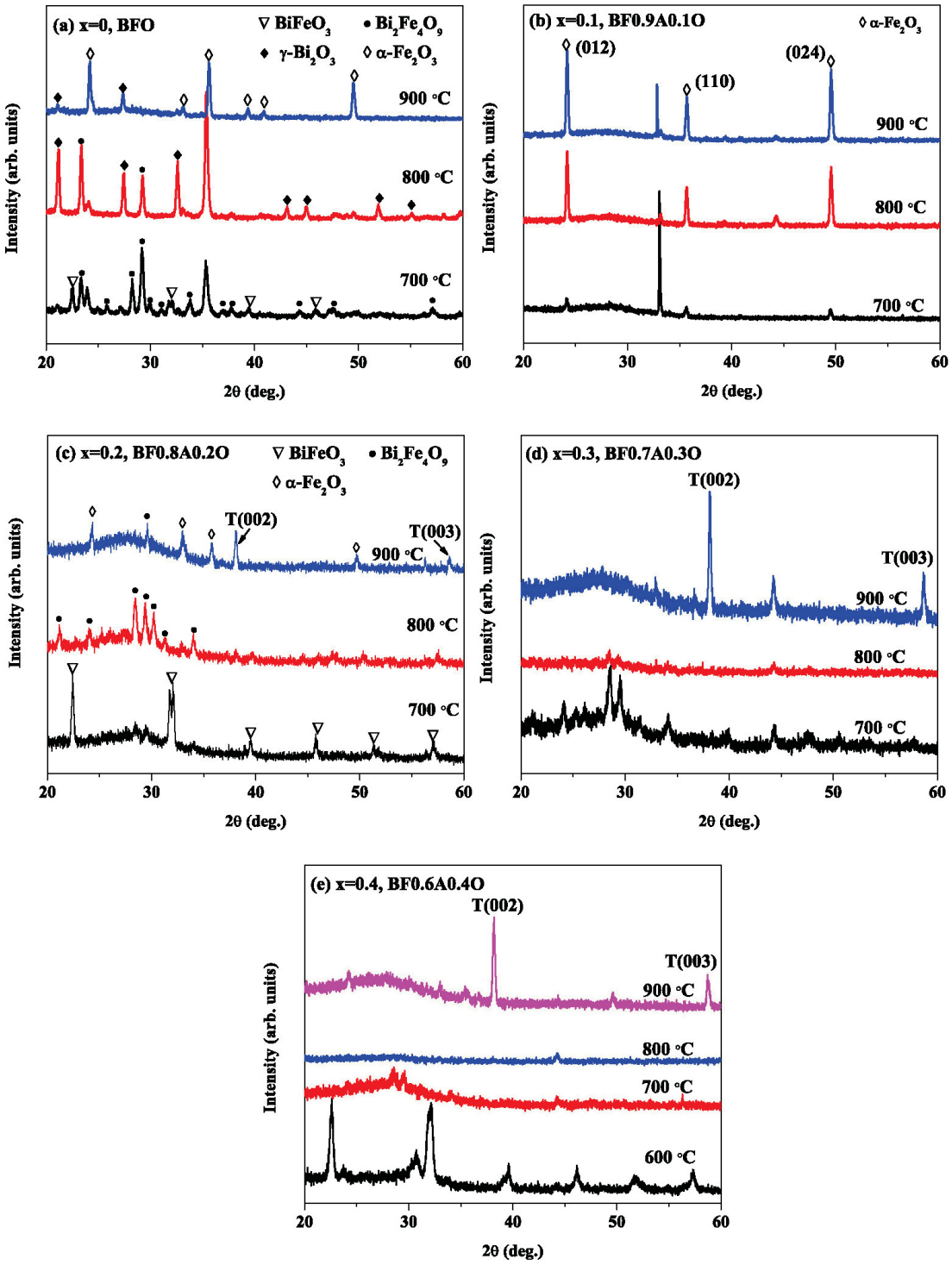

Figure 4.5 XRD patterns of BF1-xAxO films on Si (100) substrate for **(a)** x=0, **(b)** x=0.1, **(c)** x=0.2, **(d)** x=0.3 and (e) x=0.4.

Thin film which is heated up to 700 ºC shows major other phase of $Bi_2Fe_4O_9$, originated from the reaction: [22-24]

$$4BiFeO_3 \rightarrow Bi_2Fe_4O_9 + 2Bi(g) + \frac{3}{2}O_2(g) \quad (4.1)$$

Subsequently, γ-Bi_2O_3 and α-Fe_2O_3 appear with increasing annealing temperature.

There are many compelling changes in XRD patterns after doping Al. BF0.9A0.1O shows oriented Fe_2O_3 phase at high temperature (Figure 4.5(b)). The rhombohedral (012) and (024) planes correspond to cubic (001) and (002), respectively. It means that the Al doped BFO thin films tend to be *c* axis-oriented growth on Si (100) substrate at high temperature. [25] In Figure 4.5(c), two peaks located at 38 º and 59 º are observed for 900 ºC annealed BF0.8A0.2O, detected to be (002) and (003) peaks for tetragonal BFO (*T*-BFO), respectively. With increasing amount of doping Al, the relative intensity of *T*-BFO increases (Figure 4.5(d) and (e)). When x=0.4, *T*-phase turns to the principal phase for BF0.6A0.4O.

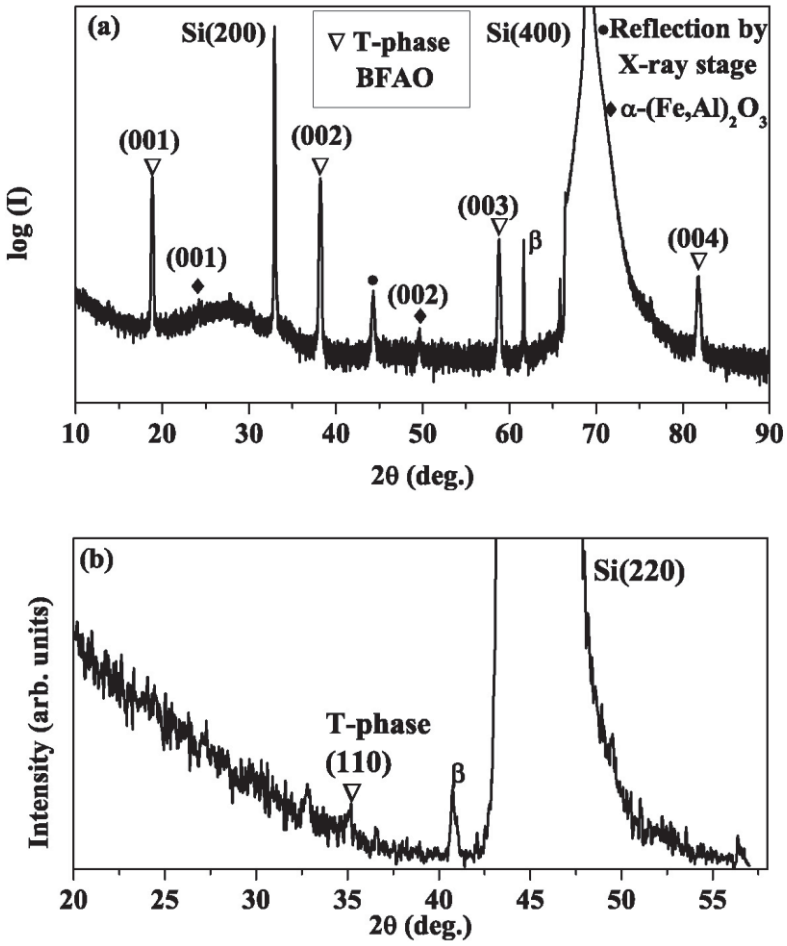

Figure 4.6 (a) Wide range out-of-plane XRD and **(b)** in-plane XRD curves for 900 ºC- annealed BF0.6A0.4O/Si (100).

In previous studies, the *T*-like phase BFO films were generally fabricated by PLD or sputtering method under vacuum. There was no report that *T*-BFO was able to obtain via simple chemical solution deposition method. In the other word, the synthesized *T*-BFO in our study is polycrystalline with oriented growth not epitaxial growth. The position of the (00*l*) peaks yields the out-of-plane parameter for BFAO of c= 4.71±0.01 Å. This c value is larger than that of strained BFO deposited on LAO (c=4.66 Å) substrate. For more evidence of *T*-like phase, wide range out-of-plane XRD and in-plane XRD are carried out on 900ºC-annealed BF0.6A0.4O (Figure 4.6). In Figure 4.6(a), clear (00*l*) peaks for *T*-phase are shown, with slight amount of oriented $(Fe,Al)_2O_3$ phase. In the in-plane XRD curves, the peak around 35 º is assigned to (110) plane of BFAO with *P*4*mm* symmetry, with a value of 3.61 Å. The c/a value of the fabricated BFAO film is 1.3, which matches well with reported c/a values of tetragonal-like BFO (c/a=1.2-1.3).

Figure 4.7(a) shows the room temperature Raman spectra of BF0.6A0.4O/Si(100) samples annealed at different temperature. Based on the previous studies of Raman scattering on BFO, we assign the main peak at 150 cm^{-1} in the curve of 600 ºC to the A_1 mode of *R*3*c* group ($4A_1$+$9E$). For *P*4*mm* space group, the Raman active modes can be summarized by ($3A_1$+B_1+$4E$). According to the calculated data, in the curve of 900 ºC, peaks around 129 and 158 cm^{-1} can be assigned to A_1 mode, while peak at 242 cm^{-1} can be denoted to *E* mode. [26-28] Known from XRD patterns (Figure 4.5(e)), crystal structure of BF0.6A0.4O transfers from rhombohedrally distorted perovskite to tetragonal symmetry via an amorphous region with increasing annealing temperature from 600 ºC to 900 ºC. The Raman scattering results match well with the XRD suggested phase transition.

In Figure 2.7(b), BFO and BF0.9A0.1O, which show γ- Bi_2O_3 and α-Fe_2O_3 phases from XRD patterns, present quite different curves compared with the other three samples which keep *T*-phase. Peaks around 98, 134 and 204 cm^{-1} can be assigned to γ- Bi_2O_3, while peaks at 224, 245 and 292 cm^{-1} are denoted to α-Fe_2O_3 phase. [29, 30] At x=0.2-0.4, typical peaks for *T*-phase are shown.

Based on the above discussion, we made a process condition diagram of $BiFe_{1-x}Al_xO_3$ as a function of the Al doping concentration (x) and RTA annealing temperature (Figure 4.8). At $x \leq 0.1$, samples show rhombohedral structure in the range from 550 ºC to 650 ºC. With increasing annealing temperature, the other

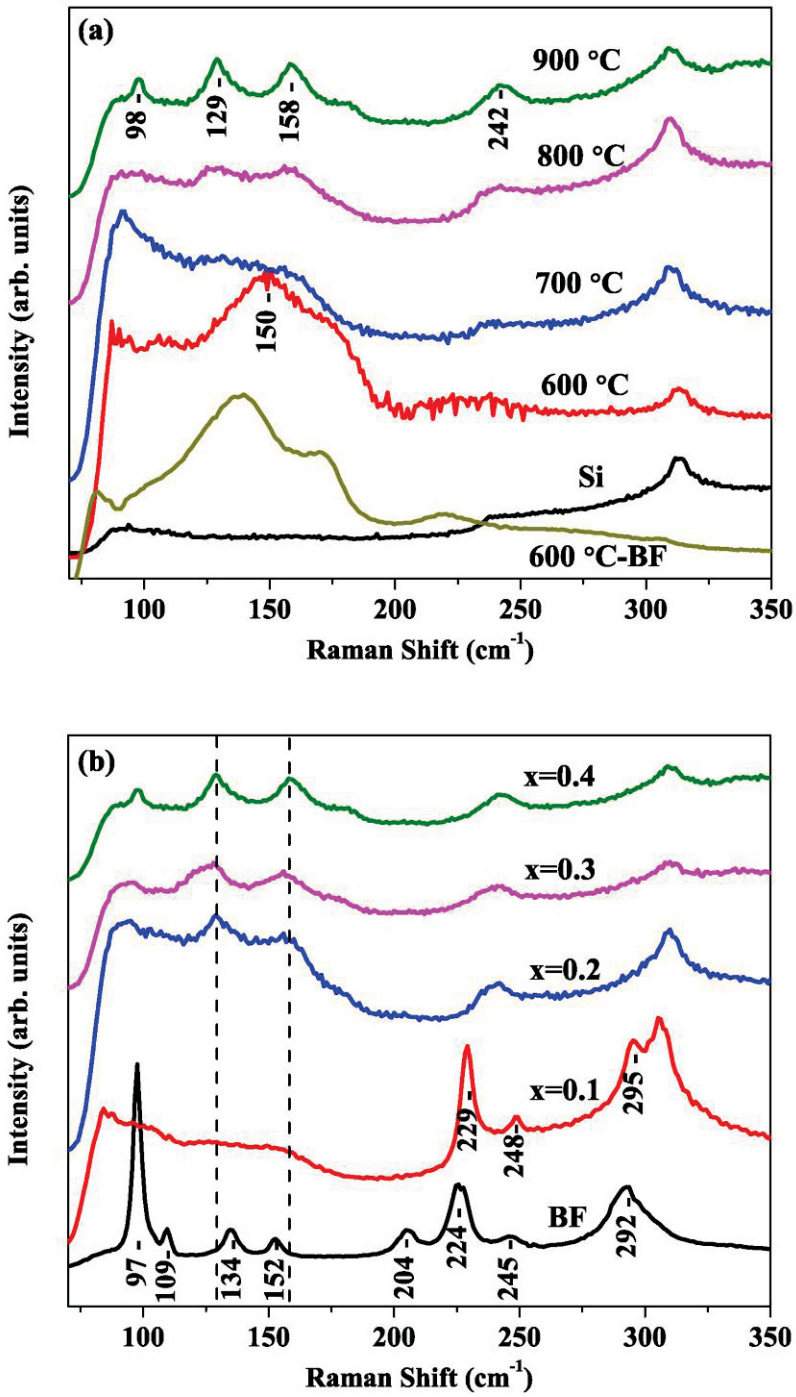

Figure 4.7 Raman spectra of **(a)** BF0.6A0.4O/Si (100) annealed at different temperature and **(b)** 900 ºC- annealed BF1-xAxO/Si (100).

phases appear due to the decomposition of BFO. For BF0.8A0.2O, *Cm* phase appears at 500 ºC and transforms to *R*3*c* symmetry at 600 ºC, with a co-existence of *R*3*c*-*Cm* phases at 550 ºC. Further increasing temperature leads to BFO decomposition. However, a slight amount of tetragonal phase is detected in 900 ºC-annealed

BF0.8A0.2O. With increasing Al concentration, at x=0.3 and 0.4, the amount of *T* phase increases, and *T* phase is the major phase in BF0.6A0.4O. The *T* phase is formed under high temperature and high Al concentration. While the *Cm* phase is likely to appear in the region of low temperature and high Al concentration. There is an obvious co-existence region for *R*3*c* and *Cm* phase, while no such co-existence region for T phase.

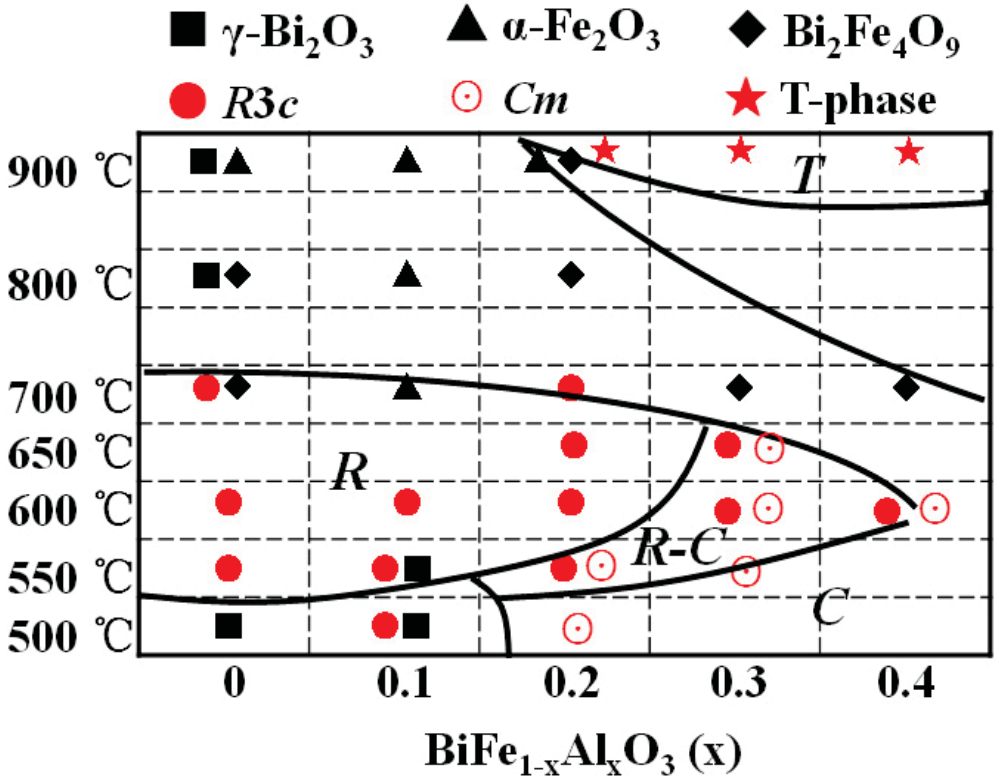

Figure 4.8 Process condition diagram of $BFe_{1-x}Al_xO_3$ (x=0-0.4) as a function of the Al doping concentration (x) and RTA annealing temperature.

The morphology of BF0.6A0.4O samples annealed from 600 ºC to 900 ºC is distinguishable as shown in Figure 4.9(a), (b), (c) and (d), respectively. An understanding of the structural evolution can be understood by investigation of the surface topography of these films using AFM. With annealing temperature increasing, the morphology transforms from spherical agglomerates to irregular granular, with a non-crystallinity intermediate region. For low Al doping concentration samples, the amount of irregular granular is less as shown in AFM images (Figure 4.9(e) and (f) for BF0.7A0.3O and BF0.8A0.2O, respectively).

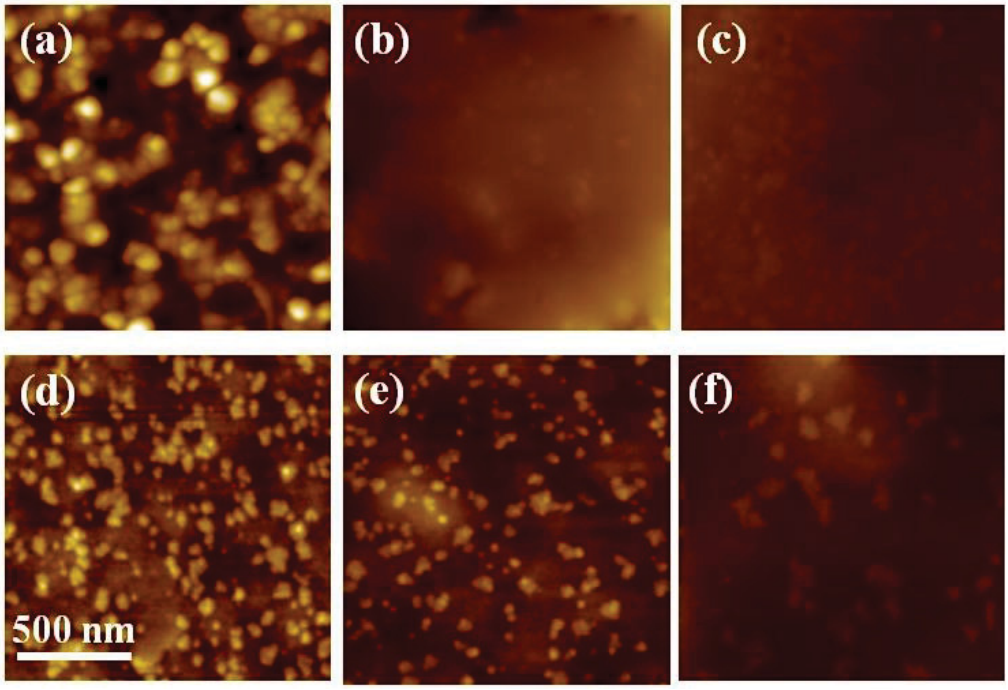

Figure 4.9 AFM images for BF0.6A0.4O/Si (100) annealed at **(a)** 600 ºC, **(b)** 700 ºC, **(c)** 800 ºC, **(d)** 900 ºC; 900 ºC- annealed **(e)** BF0.7A0.3O and **(f)** BF0.8A0.2O on Si (100).

4.3.2 Structure and morphology of $BFe_{1-x}Al_xO_3$/$LaNiO_3$/glass

The XRD patterns of RTA-annealed Au/BF1-xAxO/LNO/glass structure are shown in Figure 4.10(a) and (b). The BF1-xAxO films have no specific crystal orientation on (100)-oriented LNO underlayer. In Figure 4.10(a), after 500 ºC-RTA annealing, the formed crystalline phase is rhombohedral BFO with *R*3*c* symmetry for x=0 and 0.1, while obviously changes to the *Cm* symmetry at x= 0.3 and 0.4 though the detected peaks are weak and broad. The mixture phases is observed at x=0.2. However, the detected *Cm* phase is instable at high temperature, which just exists at x=0.4 associated with *R*3*c* principal phase after annealing at 550 ºC by RTA (Figure 4.10(b)). It matches well with the process condition diagram of BF1-xAxO shown in Figure 4.8 that *Cm* phase exists at low temperature and high Al concentration region.

Considering the results based on pure BFO films that long-time annealing is benefit for crystallinity and enhancing in-plane strain, which will bring excellent polarization behavior, the prepared BF1-xAxO/ LNO/glass were annealed by normal furnace for 5h at 500 ºC and 550 ºC, the XRD patterns of which are shown in Figure 4.10(c) and (d), respectively. In Figure 4.10(c), at x≤0.2, the patterns show slight

change that the FWHM values reduce in comparison with RTA-annealed samples (e.g. the FWHM value of (202) plane (~39º) decreased from 0.31 º (RTA) to 0.24 º (normal-annealed) for pure BFO), indicating improved crystallinity. However, at x=0.3, the *Cm* phase disappears and in return the *R*3*c* phase grows with a small amount of impurity phase. Furthermore, at x=0.4, some impurity phases (such as $Bi_2Fe_4O_9$) is detected. These results suggest that the *Cm* phase generated at high Al concentration (x>0.2) is metastable. In Figure 4.10(d), after long-time annealing at 550 ºC, only *R*3*c* phase form and *Cm* phase is not detected. Meanwhile, at x≥0.2, some impurity phases appear. It demonstrates that the crystal structure of BFAO is instable at high Al concentration, resulting in the formation of impurity phase after long-time annealing at 550 ºC.

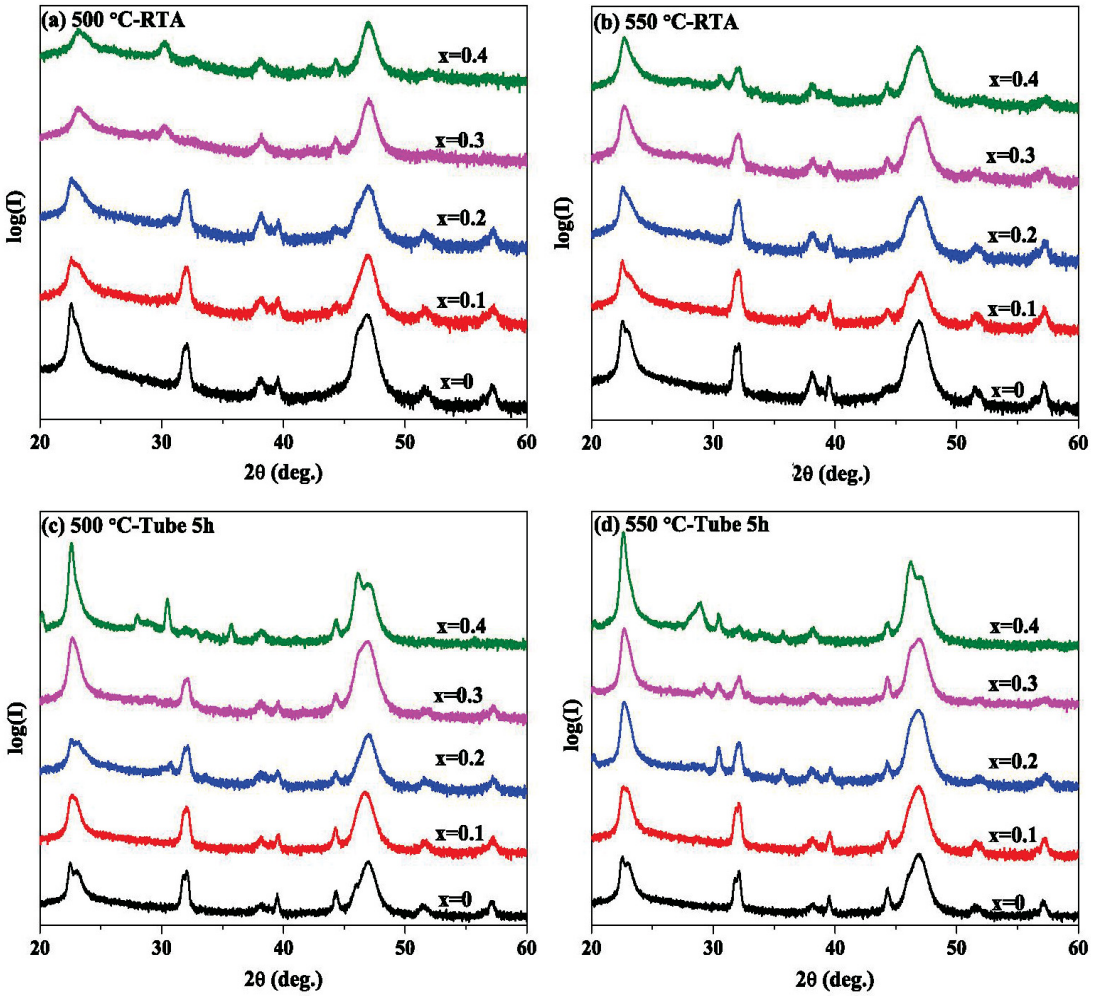

Figure 4.10 XRD patterns of Au/BFAO/LNO/glass substrate annealed at **(a)** 500 ºC and **(b)** 550 ºC by RTA, and **(c)** 500 ºC and **(d)** 550 ºC by normal tube furnace for 5h.

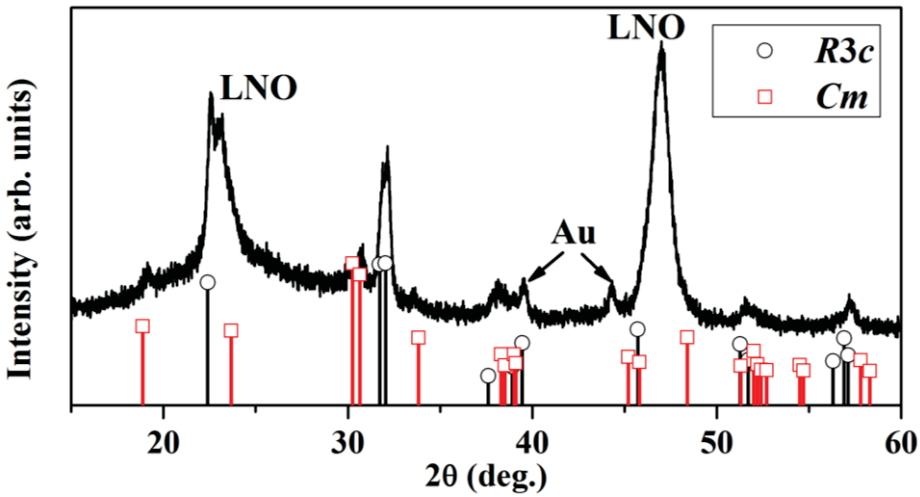

Figure 4.11 Comparison of XRD pattern for 500 ºC-Tube 5h annealed BiFe0.8Al0.2O/LNO/glass with calculated diffraction data for the *Cm* phase and PCPDF data of *R*3*c* phase BFO.

Figure 4.11 shows the XRD pattern of 500 ºC-Tube 5h annealed BiFe0.8Al0.2O, along with the calculated diffraction data of the *Cm* phase and the PCPDF data of *R*3*c* phase. It is clear that this sample keeps co-existence of *R*3*c* and *Cm* phase.

The morphology of 500 ºC-Tube 5h annealed samples is shown in Figure 4.12. At x=0.1 and 0.2, samples show relatively smaller grain size in comparison with BFO (x=0) and BF0.6A0.4O (x=0.4). It means that substitution of Al in a certain range will reduce the grain size. It is reported that the film crystallization occurs by a nucleation- and- growth process, while nucleation plays a significant role in defining the film microstructure. From standard nucleation and growth theory, the energy barrier for homogeneous nucleation is described by

$$\Delta G^* = \frac{16\pi\gamma^3}{3(\Delta Gv)^2} \tag{4.2}$$

where γ is the interfacial energy, ΔGv is the driving force for crystallization (i. e., the free energy difference per unit volume for the amorphous films- crystalline films transformation). [31] It is difficult to assess the free energy of amorphous films before annealing. Since BFO and BFAO films were prepared by the CSD method with same process, it is assumed that the free energies of BFO and BFAO films are similar in the amorphous state. Meanwhile the free energy of crystalline BFO and BFAO films are not well known. However it is known that the bond energy of Al-O is stronger

than that of Bi-O and Fe-O. Accordingly, we suggest the free energy (~lattice energy) of BFAO is higher than that of BFO. Thus the ΔG_v value of BFAO is lower than that of BFO, while the energy barrier for nucleation of BFAO is higher than that of BFO. From these, more energy needs to deal with energy barrier for nucleation during

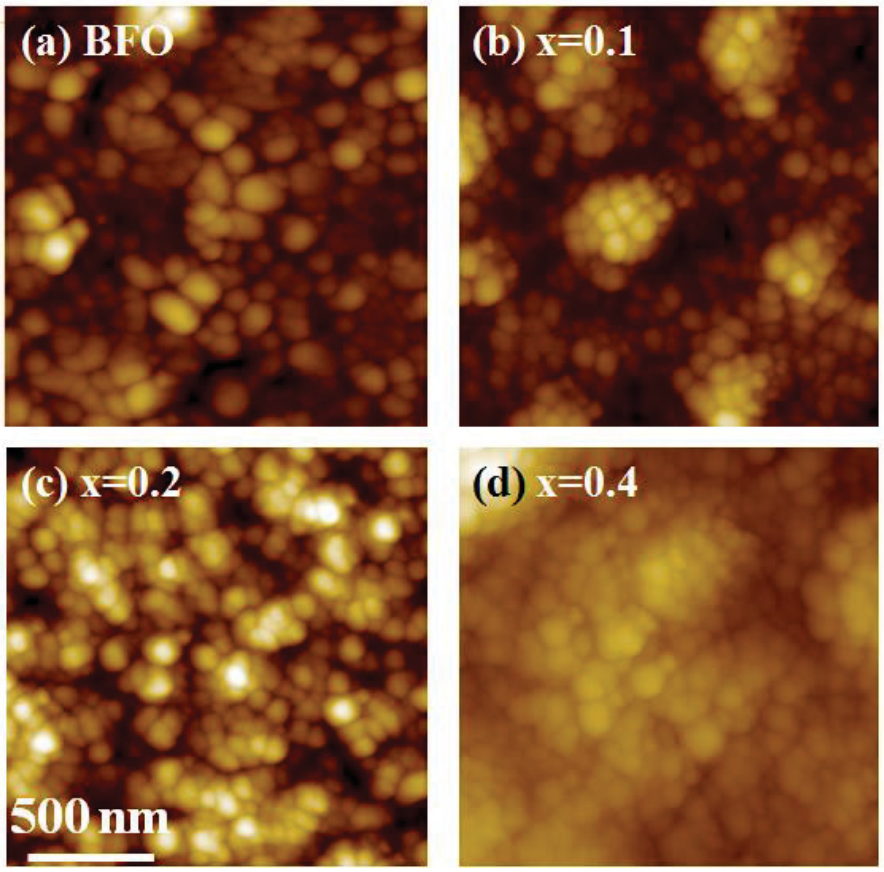

Figure 4.12 AFM images for 500 ºC-Tube 5h annealed BF1-xAxO/LNO/glass at **(a)** x=0, **(b)** x=0.1, **(c)** x=0.2 and **(d)** x=0.4.

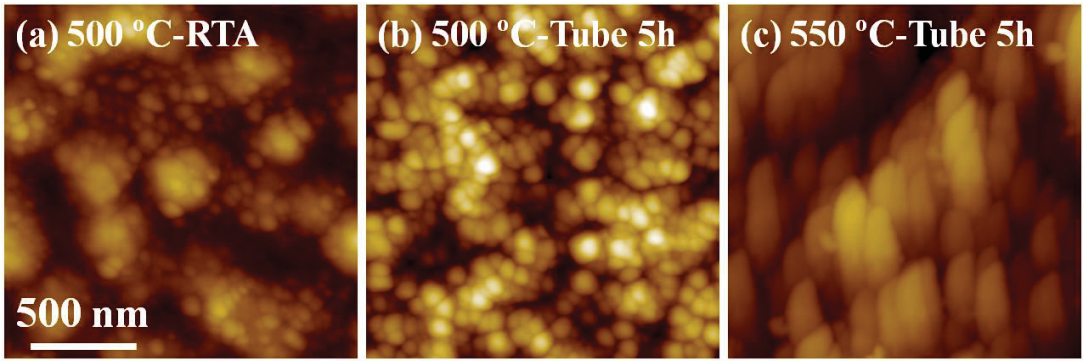

Figure 4.13 AFM images for BF0.8A0.2O/LNO/glass annealed by **(a)** 500 ºC-RTA, **(b)** 500 ºC-Tube 5h, and **(c)** 550 ºC-Tube 5h.

isothermal annealing process for BFAO films in comparison with BFO films, reducing the energy for crystal growth process. As a result of that, in a certain range of Al-substitution, the grain size reduces with increasing Al concentration. There is another evidence for the above theoretical derivation. As shown in Figure 4.1, with increasing Al concentration, the crystallization temperature of *R*3*c*-phase increases. It perhaps originates from the higher energy barrier for nucleation of BFAO. In Figure 4.12(d), at x=0.4, the anomalous grain growth perhaps due to the appearance of impurity phase.

In Figure 4.13, for BF0.8A0.2O, 500 ºC-RTA annealed sample shows relatively small grain size. After 500 ºC-Tube 5h annealing, grain size grows slightly. While after 550 ºC-Tube 5h annealing, an obvious grain growth can be detected. The long-time annealing at 500 ºC is seemed to be able to control grain size and improve crystallinity at the same time. As the relatively small grain size is able to reduce leakage current and high crystallinity is benefit for strain-induced polarization, it can be expected that sample which is long-time annealed at 500 ºC will show excellent electrical properties.

4.3.3 Electrical properties of BFAO thin films

The leakage current properties of BFAO are shown in Figure 4.14. For 500 ºC-RTA annealed samples, in Figure 4.14(a), with increasing Al concentration, the leakage current decreases. BF0.7A0.3O shows leakage current two orders of magnitude lower than that of BF0.9A0.1O. It is known that the bond energy of Al-O is larger than that of Fe-O, which benefits for reducing oxygen vacancies originated from Bi lost. Moreover, due to the variable valence state of Fe (+2 and +3), the hopping of electron from Fe^{2+} to Fe^{3+} plays an important role in electric conduction. Al^{3+} ion which has a definite oxidation state can suppress the electron hopping. Thus Al substitution can efficiently decrease leakage current. For the other annealing process, the change of leakage current follows the same general trend with Al substitution. And as expected that for the long-time annealed samples, 550 ºC-Tube 5h annealed samples (Figure 4.14(d)) show higher leakage current than 500 ºC-Tube 5h annealed samples (Figure 4.14(c)), arisen from grain growth, defects and impurity phases induced by high temperature annealing.

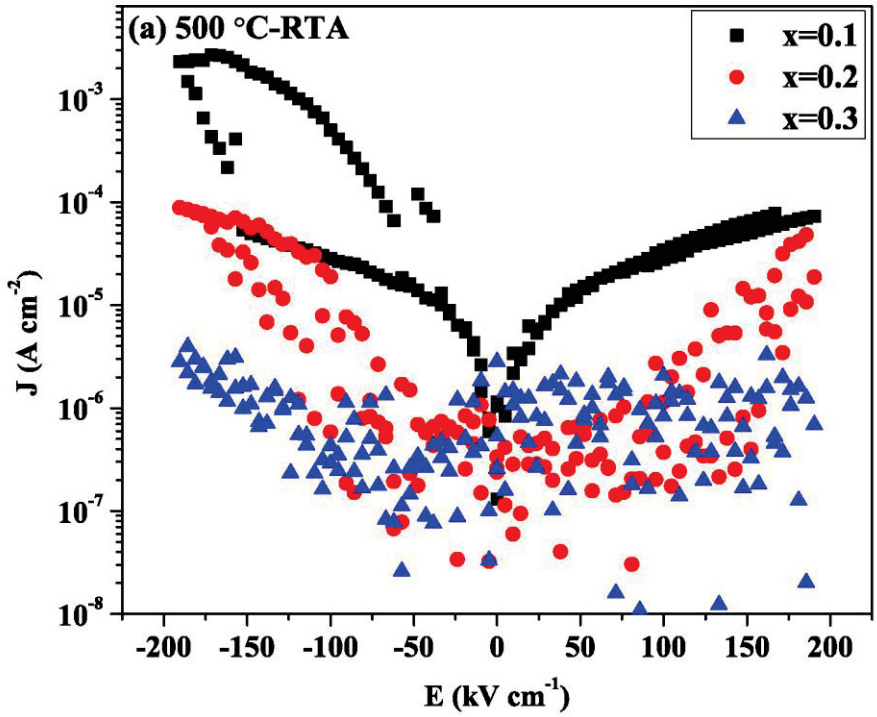
(a) 500 °C-RTA
x=0.1
x=0.2
x=0.3
J (A cm-2)
E (kV cm-1)

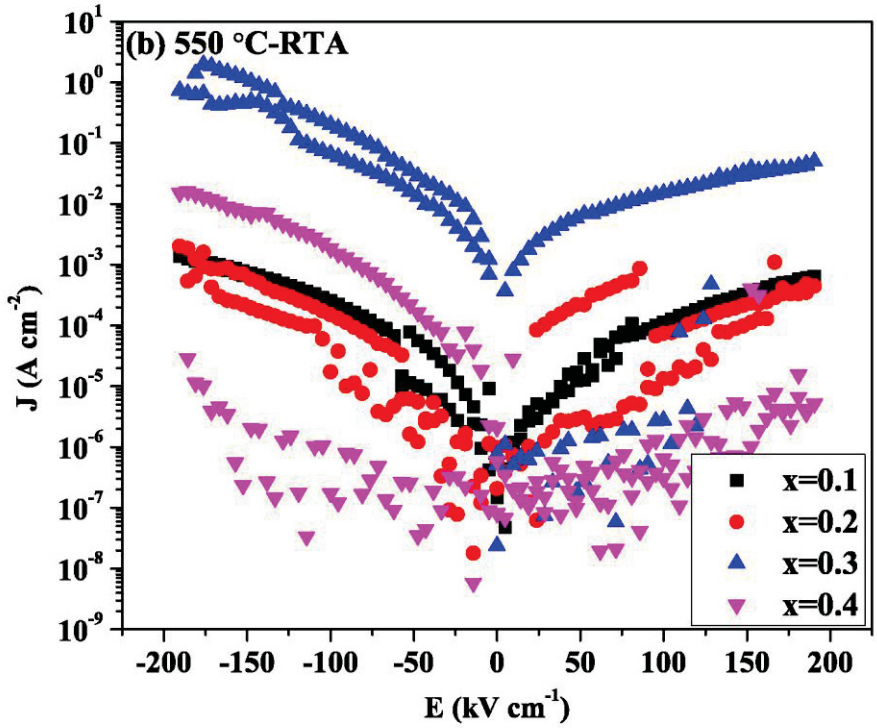
(b) 550 °C-RTA
x=0.1
x=0.2
x=0.3
x=0.4
J (A cm-2)
E (kV cm-1)

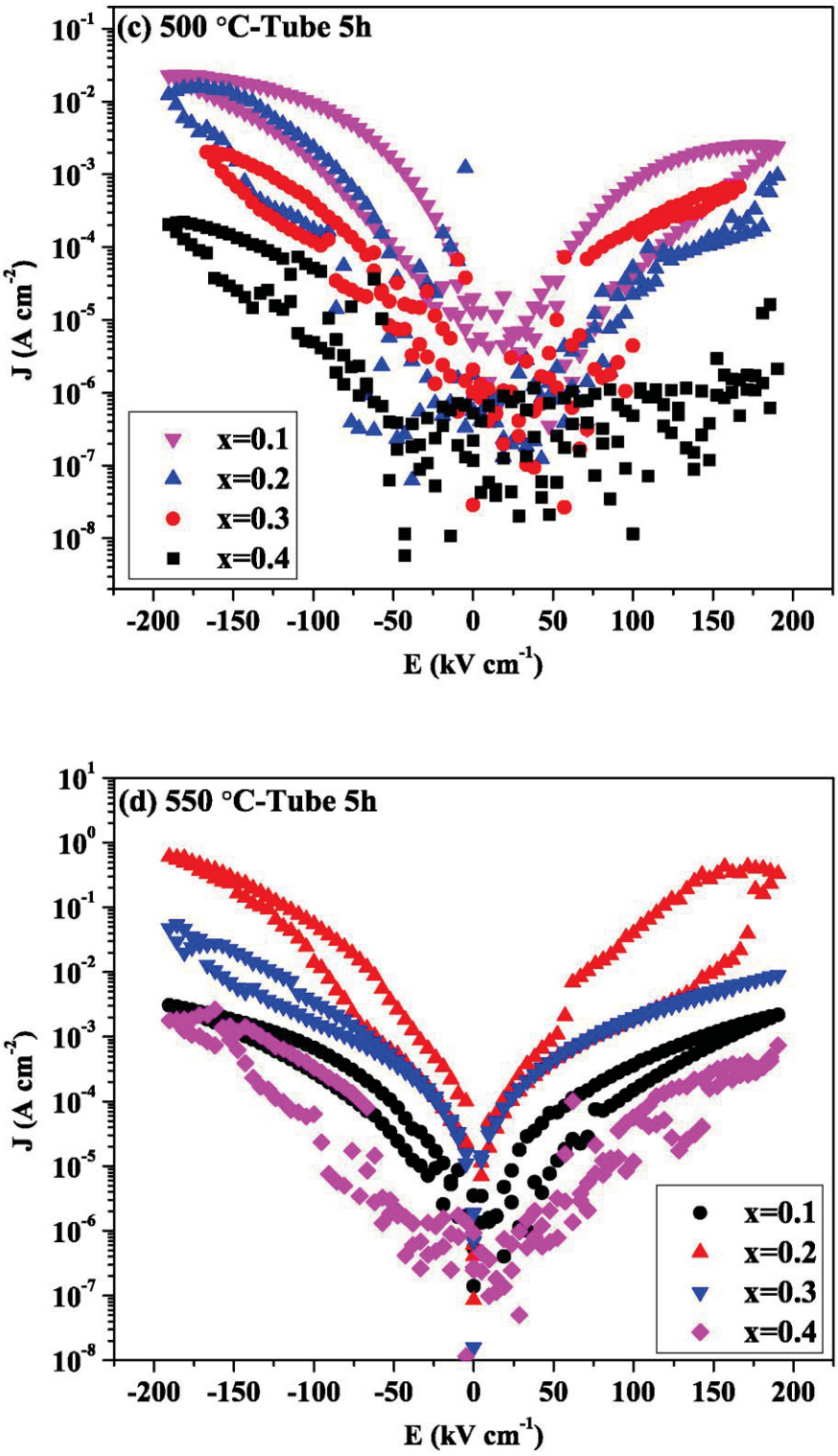

Figure 4.14 *J-E* curves of Au/BFAO/LNO/glass annealed by **(a)** 500 ºC-RTA, **(b)** 550 ºC-RTA, **(c)**500 ºC-Tube 5h, and **(d)** 550 ºC-Tube 5h, measured at room temperature.

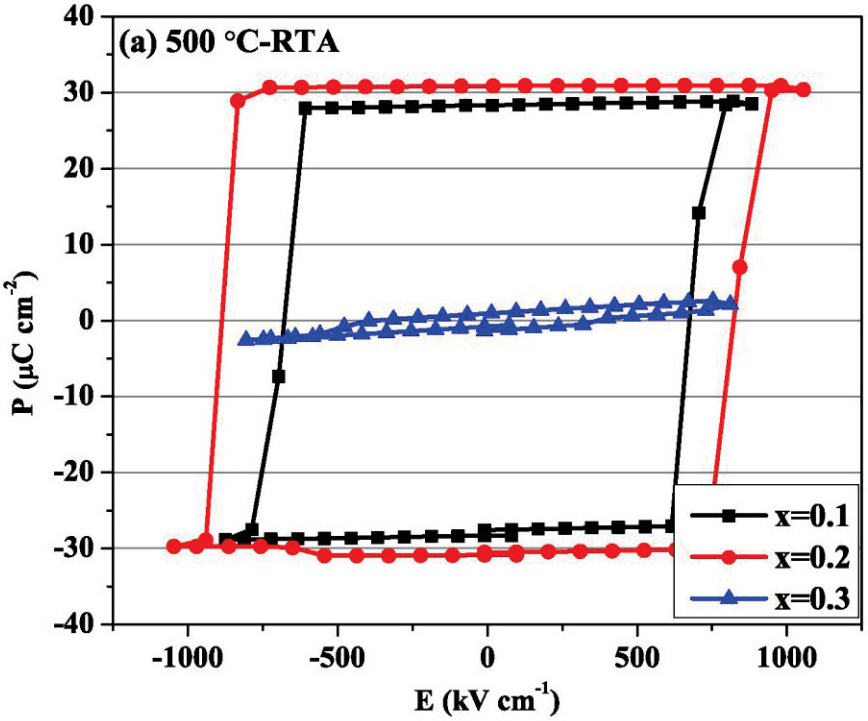
(a) 500 °C-RTA
P (μC cm-2)
E (kV cm-1)
x=0.1
x=0.2
x=0.3

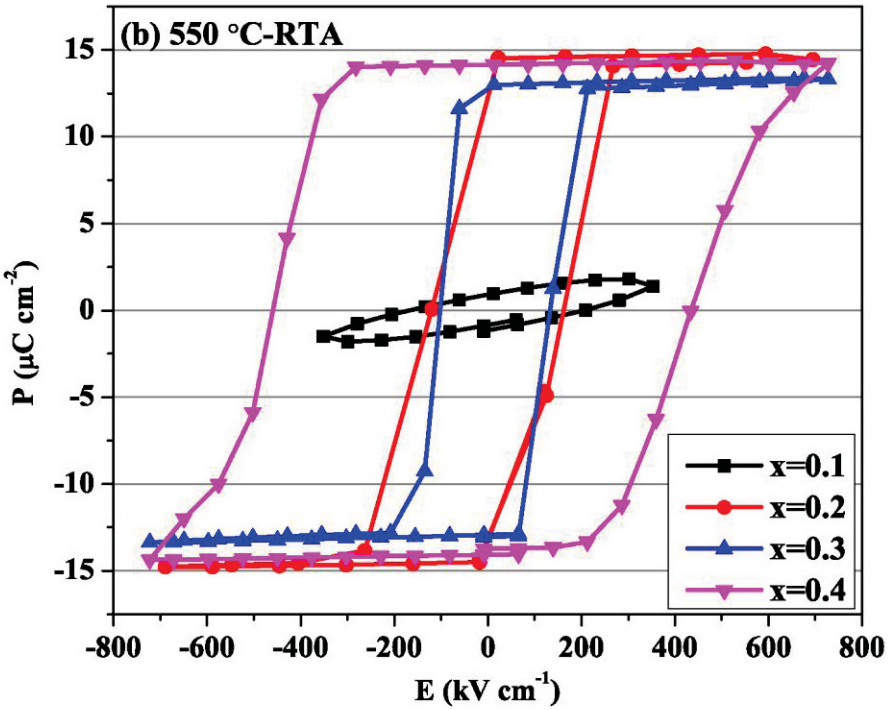
(b) 550 °C-RTA
P (μC cm-2)
E (kV cm-1)
x=0.1
x=0.2
x=0.3
x=0.4

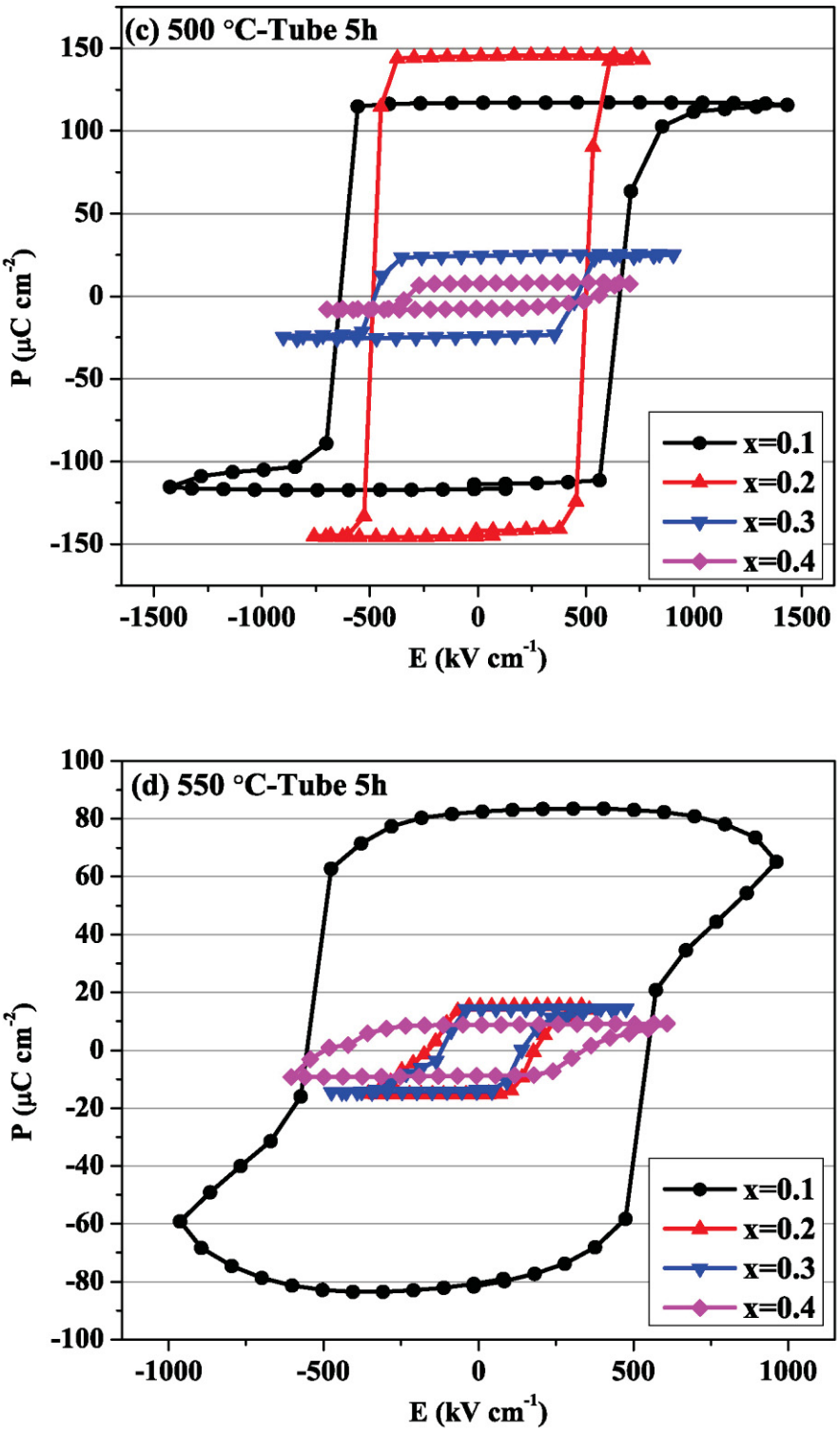

Figure 4.15 *P-E* curves of Au/BFAO/LNO/glass annealed by **(a)** 500 ºC-RTA, **(b)** 550 ºC-RTA, **(c)**500 ºC-Tube 5h, and **(d)** 550 ºC-Tube 5h, measured at room temperature.

The prepared BFAO films showed an interesting feature of polarization. As shown in Figure 4.15(a), for 500 ºC-RTA annealed BFAO, *R*3*c*-phase films (x=0.1 and 0.2) have saturated hysteresis loops with good squareness, while the *Cm*-phase BFAO (x=0.3) shows poor polarization behavior. The obtained remanent polarization (P_r) at x≤0.2 (~30μC cm^{-2}) are quite smaller than the values conventionally reported for BFO, although the P_r value slightly increases with increasing Al concentration. In Figure 4.15(b), increasing annealing temperature to 550 ºC by RTA is useless to enhance polarization. The P_r values of 550 ºC-RTA annealed BFAO even reduce to lower than 15μC cm^{-2}. These results are perhaps due to the poor crystallinity of RTA-annealed samples.

In Figure 4.15(c), all the films keep well saturated hysteresis with good squareness, attributed to the better crystallinity by long-time annealing. The observed remanent polarization is 120 μC cm^{-2} at x= 0.1, the same as that of pure BFO films reported in section 3.3.2. Here, the most striking feature is that a larger polarization of 145 μC cm^{-2} is observed at room temperature for x=0.2, where *R*3*c* and *Cm* symmetries coexist. This value is higher than the theoretical polarization of $BiAlO_3$ (75.6 μC cm^{-2}) and approaches to the theoretically predicted value of tetragonal-like $BiFeO_3$ (150 μC cm^{-2}). However, the polarization value rapidly decreases to 25 and 7.5 μC cm^{-2} for x=0.3 and 0.4, respectively. This reduction reflects the presence of impurity phases such as $Bi_2Fe_4O_9$. The results shown in Figure 4.15(d) confirm the adverse effect of impurity phase on polarization behavior. Only BF0.9A0.1O, which keeps pure *R*3*c* phase, shows high P_r value, while the other samples show P_r value lower than 20 μC cm^{-2}.

It is interesting that the observed enhancement of polarization has a strong correlation with the coexistence of *R*3*c* and *Cm* phases. BiFe0.8A0.2O film which exhibits the largest polarization is the mixture of *R*3*c* and *Cm* phase, which is the pleomorphic phase boundary (PPB) similar to morphotropic phase boundary (MPB). It is reported in Pb(Zr, Ti)O_3 (PZT) system that large piezoelectric response is expected around the MPB through an unusual switching of the polarization path under applied electric field. [32] Enhancement of polarization arising from the change of switching behavior of polarization path is also observed around the MPB in $BiFeO_3$-$PbTiO_3$ films.[33] In addition, first-principle study demonstrates that the polarization value of BFO is also dependent on the switching paths in structural

spacing. [34] As a result of these, we suggest that the lattice instability and the resultant rotation of polarization switching paths around the PPB between *R*3*c* and *Cm* phase may be responsible for the polarization enhancement of BF0.8A0.2O. Moreover, the increased carrier mobility around PPB will benefit for the mobility of domain walls, which will results in the high remanent polarization. As a result of these, it can be suggested that the B-site substitution promotes the structure deformation accompanied by the rotation of polarization direction, resulting in the enhanced polarization.

Table 3.2 P_r and E_c values for BF1-xAxO films (500 ºC-Tube 5h annealed)

x	Phase	P_r (μC cm^{-2})	E_c (kV cm^{-1})
0	*R*3*c*	120	668
0.1	*R*3*c*	116	643
0.2	*R*3*c*+*Cm*	145	478
0.3	*R*3*c*+Impurity	24.5	478

For further understanding, the list for P_r and E_c values of 500 ºC-Tube 5h annealed samples are shown in Table 3.2. For *R*3*c* phase, the P_r and E_c values are approximate to 120 μC cm^{-2} and 650 kV cm^{-1}, respectively. At the co-existence region of *R*3*c* and *Cm* phase, P_r value increases while E_c value decreases. It demonstrates the lattice instability during MPB may be responsible for the polarization enhancement. At high Al concentration of x=0.3, the presence of impurity phase makes strain relaxation and huge drop of P_r value. It is obvious that the in-plane tensile stress and Al substitution induced phase transition makes great influence on polarization property.

4.4 Conclusions

$BiFe_{1-x}Al_xO_3$ thin films with *R*3*c*, *Cm* and *T* phase can be simply obtained by the chemical solution deposition (CSD) method. The *T* phase is formed under high temperature and high Al concentration. While the *Cm* phase is likely to appear in the region of low temperature and high Al concentration. There is an obvious co-existence region for *R*3*c* and *Cm* phase, while no such region for *T* phase. The phase transition is associated with strain induced in the film formation. In the

intermediate region around x=0.2, the mixture of *R*3*c* and *Cm* phases is confirmed. The long-time annealed BFAO films show an enhancement of polarization as large as 145 μC cm^{-2} around PPB. These results suggest that modification of Fe-site of BFO induces structure and phase instability and provides a possibility of prominent enhancement of polarization and piezoelectric response.

References

[1] J. Kim, S. Kim, W. Kim, A. S. Bhalla, and R. Guo. Enhanced ferroelectric properties of Cr-doped $BiFeO_3$ thin films grown by chemical solution deposition. Appl. Phys. Lett. 88, 132901 (2006).

[2] X. Qi, J. Dho, R. Tomov, M. G. Blamire, and J. L. MacManus-Driscoll. Greatly reduced leakage current and conduction mechanism in aliovalent-ion-doped $BiFeO_3$. Appl. Phys. Lett. 86, 062903 (2005).

[3] M. Kumar and K. L. Yadav. Rapid liquid phase sintered Mn doped $BiFeO_3$ ceramics with enhanced polarization and weak magnetization. Appl. Phys. Lett. 91, 242901 (2007).

[4] Y. Wan and C. W. Nan. Ehanced ferroelectricity in Ti-doped multiferroic $BiFeO_3$ thin films. Appl. Phys. Lett. 89, 52903 (2006).

[5] W. M. Zhu and Z. G. Ye. Effects of chemical modification on the electrical properties of $0.67BiFeO_3$-$0.33PbTiO_3$ ferroelectric ceramics. Ceram. Int. 30, 1435-1442 (2004).

[6] J. Chaigneau, R. Haumont, and J. M. Kiat. Ferroelectric order stability in the $Bi_{1-x}Pb_xFeO_3$ solid solution. Phys. Rev. B 80, 184107 (2009)..

[7] S. K. Singh, S. Shanthy, and H. Ishiwara. Reduced leakage current in $BiFeO_3$-$BiCrO_3$ nanocomposite films formed by chemical solution deposition. J. appl. Phys. 108, 054102(2010)

[8] G. Catalan and J. F. Scott. Physics and applications of bismuth ferrite. Adv. Mater. 21, 2463-2485 (2009).

[9] J. Chaigneau, R. Haumont, and J. M. Kiat. Ferroelectric order stability in the $Bi_{1-x}Pb_xFeO_3$ solid solution. Phys. Rev. B 80, 184107 (2009).

[10] R. E. Cohen. Origin of ferroelectricity in perovskite oxides. Nature 358, 136-138 (1992).

[11] J. X. Zhang, Q. He, M. Trassin, W. Luo, D. Yi, M. D. Rossell, P. Yu, L. You, C. H. Wang, C. Y. Kuo, J. T. Heron, Z. Hu, R. J. Zeches, H. J. Lin, A. Tanaka, C. T. Chen, L. H. Tjeng, Y. H. Chu, and R. Ramesh. Microscopic origin of the giant ferroelectric polarization in tetragonal-like $BiFeO_3$. Phys. Rev. Lett. 107, 147602 (2011).

[12] J. Zylberberg, A. A. Belik, E. T. Muromachi, and Z. G. Ye. Bismuth aluminate: a new high-Tc lead-free piezo-/ferroelectric. Chem. Mater. 19, 6385-6390 (2007).

[13] P. Baetting, C. F. Schelle, R. Lesar, U. V. Waghmare, and N. A. Spaldin. Theoretical prediction of new high-performance lead-free piezoelectrics. Chem. Mater. 17, 1376-1380 (2005).

[14] J. Y. Son, C. S. Park, and Y. H. Shin. Epitaxial $BiAlO_3$ thin film as a lead-free ferroelectric material. Appl. Phys. Lett. 92, 222911 (2008).

[15] A. A. Belik, D. A. Rusakov, T. Furubayashi, and E. Takayama-Muromachi. $BiGaO_3$-based perovskites: a large family of polar materials. Chem. Mater. 24, 3056-3064 (2012).

[16] A. A. Belik, T. Wuernisha, T. Kamiyama, K. Mori, M. Maie, T. Nagai, Y. Matsui, and E. Takayama-Muromachi. High-pressure synthesis, crystal structures, and properties of perovskite-like $BiAlO_3$ and pyroxene-like $BiGaO_3$. Chem. Mater. 18, 133-139 (2006).

[17] H. Yusa, A. A. Belik, E. Takayama-Muromachi, N. Hirao, and Y. Ohishi. High-pressure phase transitions in $BiMO_3$ (M=Al, Ga, and In): in situ x-ray diffraction and Raman scattering experiments. Phys. Rev. B 80, 214103 (2009).

[18] J. Kreisel, P. Jadhav, O. Chaix-Pluchery, M. Varela, N. Dix, F. Sanchez, and J. Fontcuberta. A phase transition close to room temperature in $BiFeO_3$ thin films. J. Phys.: Condens. Matter 23, 343303 (2011).

[19] R. Palai, H. S. Schmid, and R. S. Katiyar. Polarized raman scattering of multiferroic BiFeO3 single domain crystal and thin film. IEEE-ISAF 2, 1 (2008).

[20] S. K. Singh, H. Ishiwara, and K. Maruyama. Enhanced polarization and reduced leakage current in $BiFeO_3$ thin films fabricated by chemical solution deposition. J. Appl. Phys. 100, 064102 (2006).

[21] P. Hansen, K. Witter, and W. Tolksdorf. Magnetic and magneto-optical properties of bismuth-substituted gadolinium iron garnet films. Phys. Rev. B 27, 4375-4383 (1983).

[22] S. M. Selbach, M. Einarsrud, T. Grande. On the thermodynamic stability of $BiFeO_3$. Chem. Mater. 21, 169-173 (2009).

[23] T. T. Carvalho, P. B. Tavares. Synthesis and thermodynamic stability of multiferroic $BiFeO_3$. Mater. Lett. 62, 3984-3986 (2008).

[24] T. Rojac, M. Kosec, B. Budic, N. Setter, and D. Damjanovic. Strong ferroelectric domain-wall pinning in $BiFeO_3$ ceramcis. J. Appl. Phys. 108, 074107 (2010).

[25] R. Ramesh and D. G. Schlom. Orienting ferroelectric films. Science, 296, 1975-1976 (2002).

[26] M. K. Singh, S. Ryu, and H. M. Jang. Polarizaed raman scattering of multiferroic $BiFeO_3$ thin films with pseudo-tetragonal symmetry. Phys. Rev. B 72, 132101 (2005).

[27] M. N. Iliev, M. V. Abrashev, D. Mazumdar, V. Shelke, and A. Gupta. Polarized Raman spectroscopy of nearly tetragonal $BiFeO_3$ thin films. Phys. Rev. B 82, 014107 (2010).

[28] M. K. Singh, H. M. Jang, S. Ryu, and M. Jo. Polarized Raman scattering of multiferroic $BiFeO_3$ epitaxial films with rhomboderal R3c symmetry. Appl. Phys. Lett. 88, 042907 (2006).

[29] J. Salazar-Perez, M. A. Camacho-Lopez, L. Escobar-Alarcon, E. Camps. Synthesis and characterization of $LiNiO_2$ targets for thin film deposition by pulsed laser ablation. Superficies y Vacio 18, 27-30 (2005).

[30] A. Zoppi, C. Lofrumento, E. M. Castellucci, and Ph. Sciau. Al-for-Fe substitution in hematite: the effect of low Al concentration in the Raman spectrum of Fe_2O_3. J. Raman Spectrosc. 39, 40-46 (2008).

[31] R. W. Schwartz. Chemical solution deposition of perovskite thin films. Chem. Mater. 9, 2325-2340 (1997).

[32] L. Bellaiche, A. García, and D. Vanderbilt. Electric-field induced polarization paths in $Pb(Zr_{1-x}Ti_x)O_3$ alloys. Phys. Rev. B 64, 060103(R) (2001).

[33] M. A. Khan, T. P. Comyn, and A. J. Bell. Large remanent polarization in ferroelectric $BiFeO_3$-$PbTiO_3$ thin films on Pt/Si substrates. Appl. Phys. Lett. 91, 032901 (2007).

[34] J. B. Neaton, C. Ederer, U. V. Waghmare, N. A. Spaldin, and K. M. Rabe. First-principles study of spontaneous polarization in multiferroic $BiFeO_3$. Phys. Rev. B 71, 014113 (2005).

Chapter 5

Phase Transition and Electrical Properties of $BiFe_{1-x}Ga_xO_3$ Thin Films

5.1 Introduction

Besides Al, in the group of nonmagnetic ions with +3 oxidation state, Ga is another attractive element. Researches on polar perovskite-type crystal, such as Bi*M*O_3 (*M*=Al, Ga, In, and Co) have been intensively done. [1-4] Belik *et al*. [5] reported that a large family of polar materials with *R*3*c* and *Cm* symmetries was found for solid solution of $BiGa_xM_{1-x}O_3$ (*M*= Cr, Mn and Fe) and the supertetragonal-*Cm* like phase which was just obtained in BFO film previously could be stabilized in bulk form in this system.

$BiGaO_3$ is indexed in an orthorhombic system with lattice parameters of *a*≈5.4162 Å, *b*≈5.1335 Å and *c*≈4.9685 Å. Theoretical studies on $BiGaO_3$ predicted that they could be high-performance piezoelectrics and ferroelectrics with a very large spontaneous polarization (151.9 μC cm^{-2} along the [100] direction). [6] However, high-pressure and high-temperature synthesis is required for preparation of this material as reported, the same as $BiAlO_3$. In the research of Belik *et al*., after high-pressure and high-temperature process, the synthesized *Cm* phase samples are powder, which prevents the measurement of ferroelectric properties of these novel materials.

Thus, in this section, we would like to fabricate Ga-doped BFO ($BiFe_{1-x}Ga_xO_3$, BF1-xGxO) thin films by simple chemical solution deposition. The phase transition with Ga concentration will be investigated. Then the electrical properties of $BiFe_{1-x}Ga_xO_3$ thin films will be detected.

5.2 Experiment

5.2.1 Precursor solution

The $BiFe_{1-x}Ga_xO_3$ (BF1-xGxO, x=0, 0.05, 0.1 and 0.2) thin films were fabricated by the CSD method. The starting reagents were bismuth nitrate ($Bi(NO_3)_3 \cdot 5H_2O$, 99.5%), ferric nitrate ($Fe(NO_3)_3 \cdot 9H_2O$, 99%) and gallium nitrate ($Ga(NO_3)_3 \cdot 8H_2O$, 99%). They were dissolved in acetic acid ($C_2H_4O_2$, 99.7%) with stoichiometry by stirring under heating. An appropriate amount of acetylacetone ($C_5H_8O_2$, 99%) was added into the solution as a chelating agent. The concentration of precursor solutions was 0.2mol L^{-1}.

5.2.2 Film deposition

The solution was spin-coated onto glass or Si(100) substrate, followed by pre-heating at 180 ºC and heating at 380 ºC for 3 min to remove the solvent and decompose the nitrates respectively. These steps were repeated for 5 times to obtain the desired thickness (~200 nm). After that, the films were annealed by RTA (temperature rise up in 1 min and keep 10 min) and normal furnace (Tube 5h, quickly push into the pre-heated furnace and keep 5h). Details for annealing process are shown in Table 5.1.The LNO underlayer and Au top layer with 200 μm in diameter were fabricated by sputtering and acted as electrodes for ferroelectric measurement. The LNO bottom electrode was annealed at 650 º C for 3 h. Details for annealing process are shown in Table 5.1.

5.2.3 Measurement

The structural properties of the prepared films were characterized by X-ray diffraction (Cu *Kα* radiation, Rigaku-Smartlab). AFM images were collected to describe the morphology of thin films surface. Leakage current behaviors were estimated using FCE-1 Keithley 230 voltage source and Keithley 6487 picoammeter . The applied voltage was swept from 0 V to 4 V, and from 4 V to -4 V, and from -4 V to 0 V, at a rate of 0.1 V s^{-1}. The polarization hysteresis was measured at a frequency

of 5 kHz at room temperature by using ferroelectric test system FCE-1.

Table 5.1 Annealing conditions for BFGO films on different substrates

	Glass substrate	Si(100) substrate	LNO/glass
RTA (ºC)	500, 550, 600, 650	600, 700, 800, 900	500, 550
Tube 5h(ºC)			500, 550

5.3 Results and discussion

5.3.1 Structure and phase transition of $BiFe_{1-x}Ga_xO_3$ films

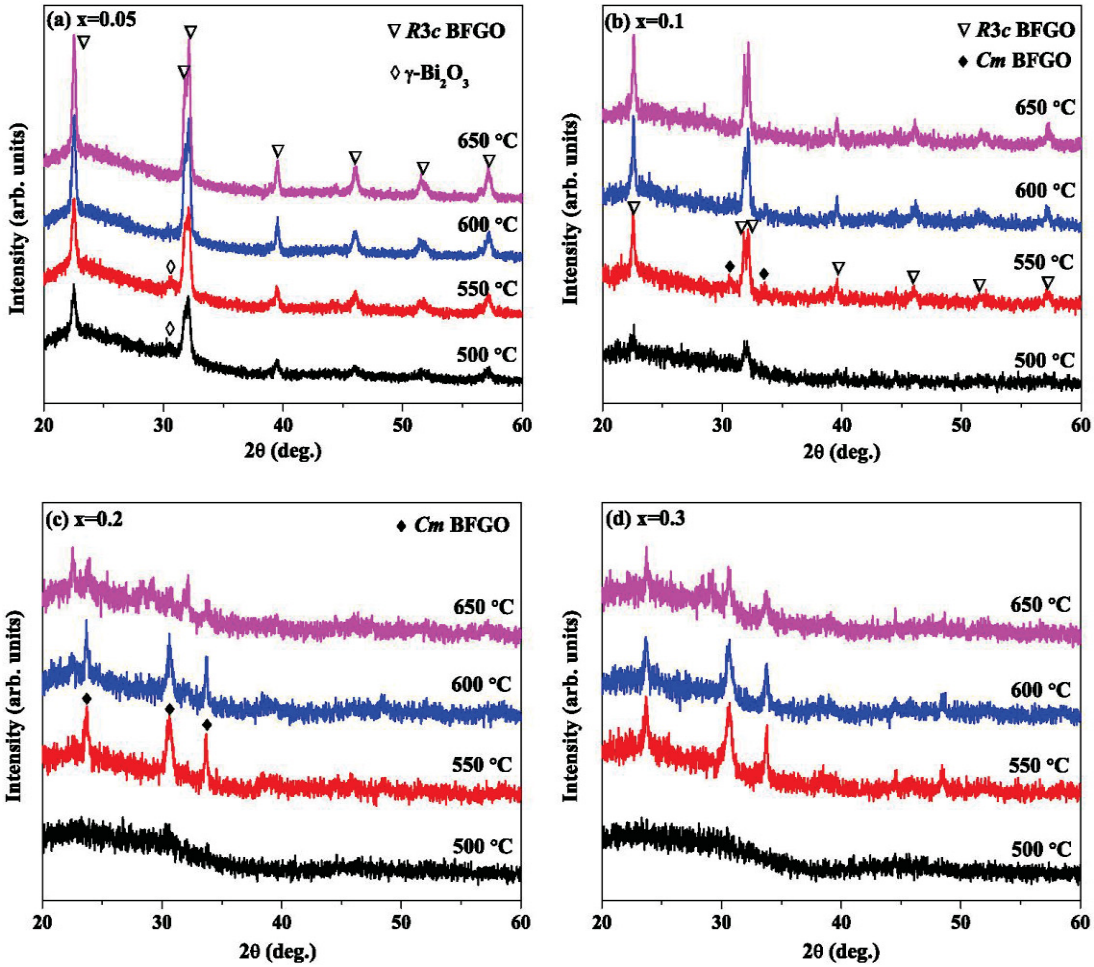

Figure 5.1 XRD patterns of BF1-xGxO on glass for **(a)** x=0.05, **(b)** x=0.1, **(c)** x=0.2, and **(d)** x=0.3.

Figure 5.1 shows the XRD patterns of BF1-xGxO (BFGO) films deposited on glass substrate and annealed at different temperature. At x=0.05, when annealed at low temperature, the second phase (Bi_2O_3) appears, while sample annealed at 650 ºC shows pure *R*3*c* phase. The perovskite structure with rhombohedral distortion is supported by the clear split peaks around 32 º, which are the peaks of (104) and (110) plane for *R*3*c*-BFO. At x=0.1, sample annealed at 550 ºC shows a mixture of *R*3*c* and *Cm* phases. After increasing annealing temperature to 600 ºC and 650 ºC, the peaks for *Cm* phase disappear and sample keeps pure *R*3*c* phase. At x=0.02 and 0.03, the pure *Cm* phase appears after annealing around 550 ºC and 600 ºC, and disappears at higher temperature. The BFGO films keep the same tendency with BFAO films that the *Cm* phase appears at low temperature and high Ga (Al in BFAO system) concentration regions. However the difference is that in BFAO system, the peaks for *Cm* phase are broad and in weak intensities. While in BFGO system, sharp and high intensities peaks are shown in XRD curves, indicating the better crystallized *Cm* phase in comparison with that of BFAO system.

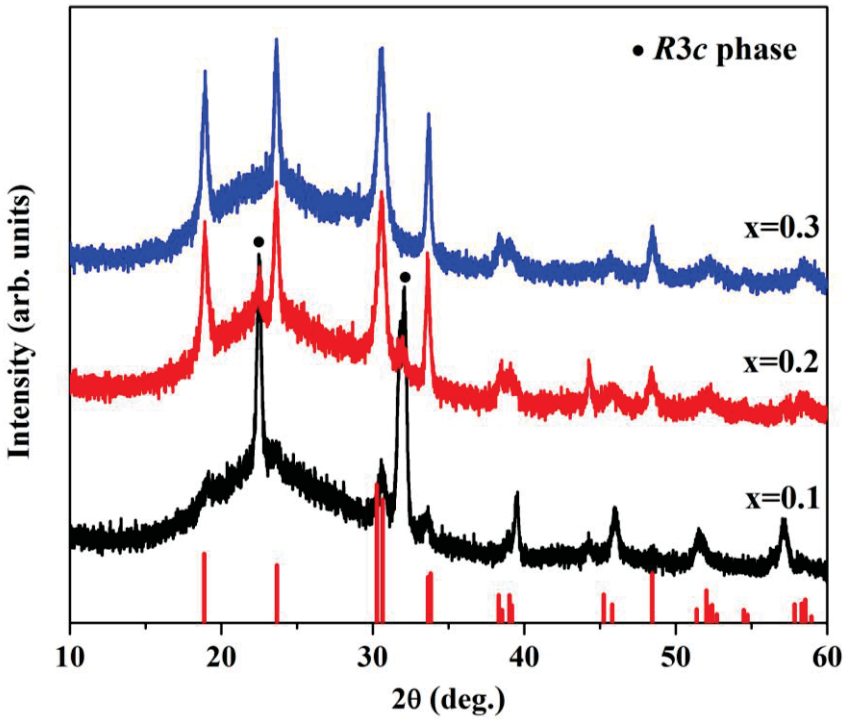

Figure 5.2 XRD patterns of 550 ºC annealed BF1-xGxO/glass (x=0.1-0.3).

For detailed comparison, XRD patterns of 550 ºC annealed samples were detected in wider 2θ range by Rigaku-Smartlab, as shown in Figure 5.2. It is obvious that the

*R*3*c*-*Cm* co-existence region is at x=0.1-0.2, *R*3*c* is major phase at x=0.1 while *Cm* is major phase at x=0.2. At x=0.3, pure *Cm* phase appears. It indicates that *Cm* phase is easy to form at high Ga concentration region.

We calculated the lattice parameters of 550 ºC-RTA annealed BFGO which were prepared on glass substrate by the whole powder pattern fitting (WPPF) method, listed in Table 5.2. At x=0.05, the *a* value of *R*3*c* phase is smaller than that of BFO, due to the smaller ionic radius of Ga^{3+} in comparison with Fe^{3+}. As x rising from 0.05 to 0.2, *a* parameters of *R*3*c* phase increase, arisen from the monoclinic distortion induced by in-plane tensile stress. At x=0.1 and 0.2, where is the co-existence region for *R*3*c* and *Cm* phase, the *c* values of unit cell show large deviation between *R*3*c*

Table 5.2 Calculated lattice parameters for 550 ºC-RTA annealed BF1-xGxO/glass

x	*R*3*c*		*Cm*		
	a (Å)	*c*(Å)	*a*(Å)	*c*(Å)	*c/a*
0	5.5764	13.8551			
0.05	5.5651	13.8556			
0.1	5.5671	13.8437	5.3312	4.6378	0.87
0.2	5.5678	13.8891	5.3126	4.6922	0.88
0.3			5.3102	4.6874	0.88

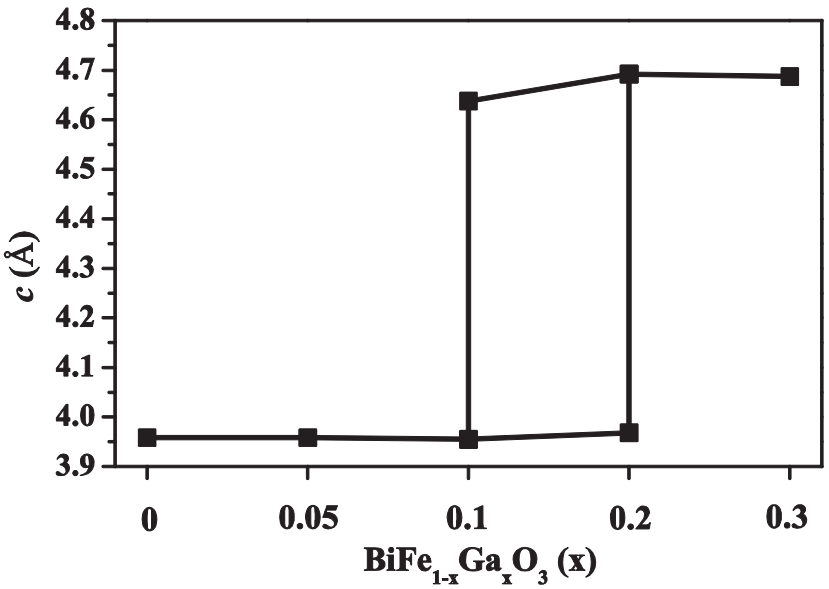

Figure 5.3 Ga concentration (x)-dependence of lattice parameters *c* for BF1-xGxO/glass annealed at 550 ºC.

phase and *Cm* phase, as shown in Figure 5.3, indicating a complex structure in this region corresponded with the strain-induced monoclinic distortion. At x=0.3, *Cm* phase of BF0.7G0.3O shows smaller lattice parameters than that of BF0.8G0.2O, arisen from the smaller ionic radius of Ga^{3+}.

The approximate phase diagram of this system ($BiFe_{1-x}Ga_xO_3$) has been given by Belik *et al*. It is reported that this system has a pyroxene-type structure ($BiGaO_3$, x=1.0) with space group *Pcca* and a perovskite structure ($BiFeO_3$, x=0) with space group *R*3*c* as end member. With increasing x value (Ga concentration), this system shows a phase transition around x=0.3 from rhombohedral structure (*R*3*c*) to a new monoclinic structure with space group *Cm* which is similar to the $PbTiO_3$-type perovskite structure with space group *P*4*mm*. [5] But in their study, the *Cm* phase just can be prepared via the high-pressure (6 GPa) and high-temperature (1700 K) method, which is quite different from our results that the *Cm* phase just appears at low temperature.

This striking result that the *Cm* phase is successfully obtained at low temperature of 833 K under normal atmospheric pressure is likely associated with strain induced in the film formation. This strain is derived from the difference of thermal expansion coefficient between film (10.9×10^{-6} ºC^{-1} for BFO [7]) and substrate (3.17×10^{-6} ºC^{-1} for glass), reaching an order of GPa by estimated assuming thermal expansion coefficient, and typical Young modulus (~195 GPa) and Poisson's ratio (~0.3) for ferrite. [8] The film suffers in-plane tensile stress from the glass substrate which has a smaller thermal expansion coefficient. This tensile stress expands the lattice volume and lowers formation energy of crystal phase that has larger unit cell volume. Furthermore, for $BiFe_{1-x}Ga_xO_3$, the substituted Ga^{3+} performs stronger distortion of octahedral environment, tending to a square-pyramidal coordination which is similar to the pyroxene-type structure of $BiGaO_3$. This kind of distortion will lead to the increase of unit cell volume, resulting in the structure transition to the phase with large unit cell volume (*R*3*c*→*Cm*→*Pcca* with increasing Ga concentration). The calculated lattice parameters shown in Table 5.2 support this suggestion. Thus, it is natural that the tensile stress assists the transition to *Cm* phase accompanied by the Ga-substitution.

As another factor of *Cm*-phase occurrence, crystallization at low temperature should be also considered. For the bulk reaction of Bi-Fe-Ga-O system, high

temperature and/or high pressure are supplied as driving force for crystallization arisen from the small solubility of Bi-Ga-O system. Meanwhile, high pressure is required to prevent the structure containing Bi from decomposition. In our study, contributed to the advantage of CSD method, the crystallization process occurs at lower temperature that high pressure is not necessary for low-temperature crystallization. It allows stabilization of high-pressure phase such as *Cm* phase at ambient pressure.

In either case, the thermal stability of the produced *Cm* phase at the preparation temperature is required. As the *Cm* phase is reported to be stable below 873 K, our preparation temperature satisfies this limitation. When annealing temperature is higher than 600 ºC, *Cm* phase disappears. However, the detailed origin for formation of the *Cm* phase is not yet clear.

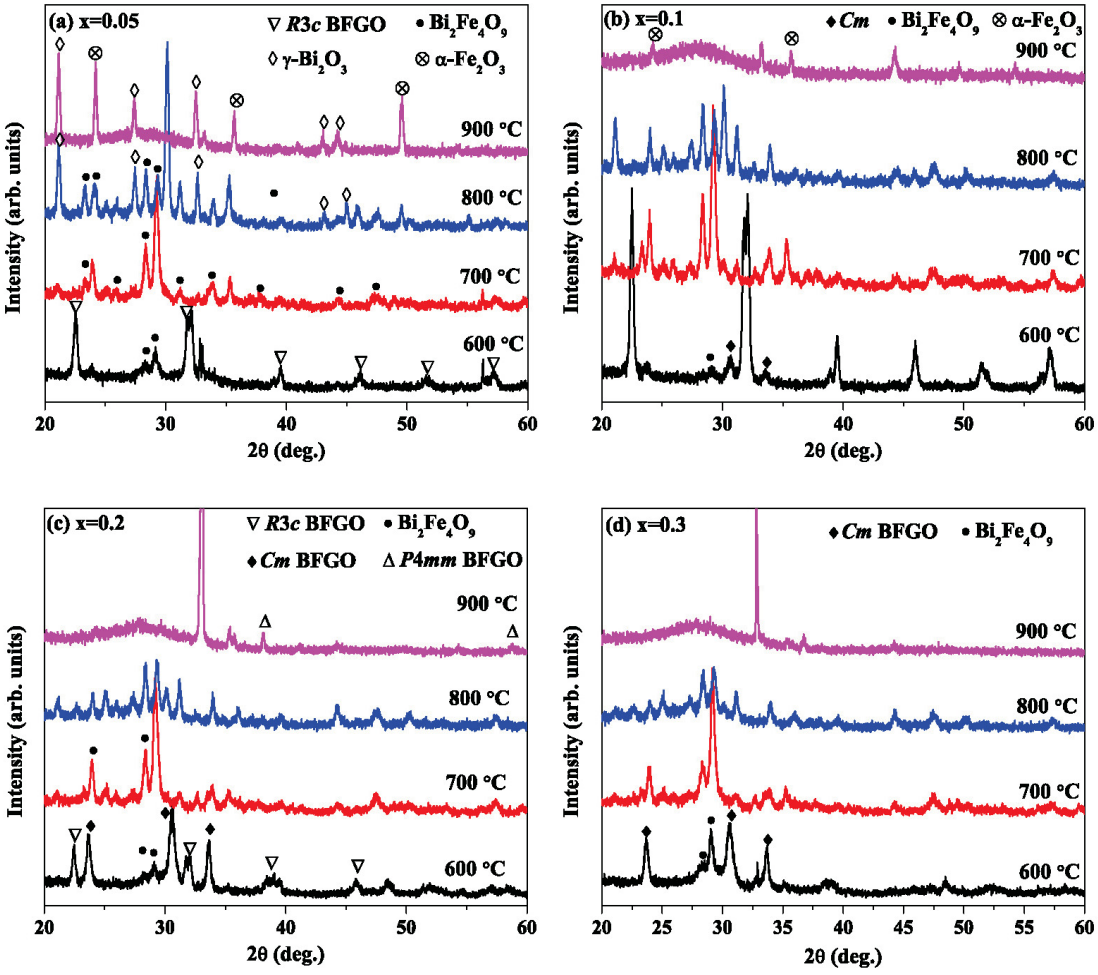

Figure 5.4 XRD patterns of BF1-xGxO films on Si (100) substrate for **(a)** x=0.05, **(b)** x=0.1, **(c)** x=0.2, and **(d)** x=0.3.

In order to detect the crystallization of BFGO at temperature higher than 650 ºC, thin films were deposited on Si (100) substrate which can be heated at higher temperature. Figure 5.4 shows the XRD patterns of BFGO films deposited on Si (100) substrate.

In Figure 5.4(a), BF0.95G0.05O shows the similar behaviour with pure BFO. Film that is heated up to 700 ºC shows major other phase of $Bi_2Fe_4O_9$. Subsequently, γ-Bi_2O_3 and α-Fe_2O_3 phase appear with increasing annealing temperature arisen from decomposition of BFO. At x=0.1 and 0.2, 600 ºC annealed sample shows the co-existed of *R*3*c* and *Cm* phases, with slight amount of $Bi_2Fe_4O_9$. With increasing annealing temperature, the impurity phases turn to major phase. 900 ºC-annealed BF0.9G0.1O shows oriented Fe_2O_3 phase, which is close to 900 ºC-annealed BF0.9A0.1O. 900 ºC-annealed BF0.8G0.2O shows two weak peaks around 38 º and 59 º, which is similar as the (002) and (003) tetragonal phase peaks detected in BFAO system. The out-of-plane spacing for *T*-BF0.8G0.2O is calculated to be 4.71 Å, which is the same as *T*-BFAO. However, in BFAO system, with increasing amount of doping Al, the intensity of *T*-BFAO increases. When x=0.4, *T*-phase turns to the principal phase for BF0.6A0.4O. It is different in BFGO system, as seen in Figure 5.4(d), at x=0.3, we cannot detect any peak for *T*-phase. There is an instinct reason for this change that the ionic radius of Ga^{3+} (r_{IV}=0.47 Å and r_{VI}=0.62 Å) is larger than that of Al^{3+} (r_{IV}=0.39 Å and r_{VI}=0.535 Å) and close to that of Fe^{3+} (r_{IV}=0.49 Å and r_{VI}=0.645 Å). Al-substitution seems to make larger distortion of crystal structure due to the huge difference in ionic radius. Thus, the highly-distorted tetragonal phase is easy to form in BFAO system.

Based on the XRD patterns, we made a process condition diagram of $BFe_{1-x}Ga_xO_3$ as a function of the Ga doping concentration (x) and RTA annealing temperature. At $x \leq 0.05$, samples show rhombohedral structure in the range from 550 ºC to 650 ºC. With increasing annealing temperature, the other phases appear due to the decomposition of BFO. When x=0.1 and annealing temperature around 550 ºC to 600 ºC, the co-existence of *R*3*c* and *Cm* phase appears. This is the region as called pleomorphic phase boundary (PPB). With increasing temperature to 650 ºC, the *Cm* phase disappears and only *R*3*c* phase remains. Subsequently increasing temperature, the other phases appear due to the decomposition of BFO. At $x \geq 0.2$, the pure *Cm* phase forms around 550 ºC and the other phase of $Bi_2Fe_4O_9$ appears even at low

temperature of 600 ºC. It means that at high Ga concentration, the BFGO structure is unstable. Thus the second phase is easy to form at temperature as low as 600 ºC. At x=0.2, a slight amount of tetragonal phase is formed at 900 ºC. However the *T*-phase disappears at x=0.3, perhaps due to the decomposition of BFGO.

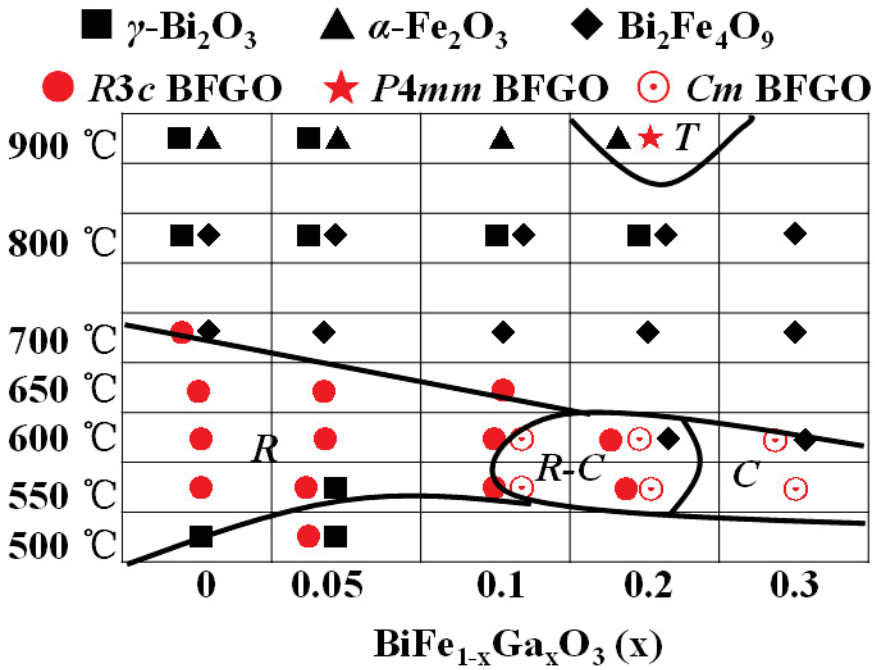

Figure 5.5 Process condition diagram of $BFe_{1-x}Ga_xO_3$ as a function of the Ga doping concentration (x) and RTA annealing temperature.

5.3.2 Structure and ferroelectric properties of BFGO/LNO

The XRD patterns of Au/BF1-xGxO/LNO/glass structure are shown in Figure 5.6, grouped by annealing method. Seen from Figure 5.6(a), after 500 ºC- RTA annealing, BFGO crystallize in *R*3*c* phase at x=0.05; at x=0.3, the *Cm* phase is formed; for x=0.1 and 0.2, the mixture of *R*3*c* and *Cm* phase appears. The 500 ºC-RTA annealed BFGO/LNO/glass keep the similar crystalline condition with 550 ºC-RTA annealed BFGO/glass. The decrease of crystallization temperature means that on LNO/glass substrate, the *R*3*c*-*Cm* phase transition is easier to carry out in comparison with on glass substrate. We attribute it to the similar crystal structure of LNO and BFO, which are both perovskite and keep approximate unit cell (a_{BFO}=3.97 Å and a_{LNO}=3.85 Å). The nucleation and crystal growth on LNO/glass will be easier due to

the matched lattice is able to decrease the driving force of crystallization. As a result of that the *Cm* phase can be formed at lower temperature on LNO/glass substrate.

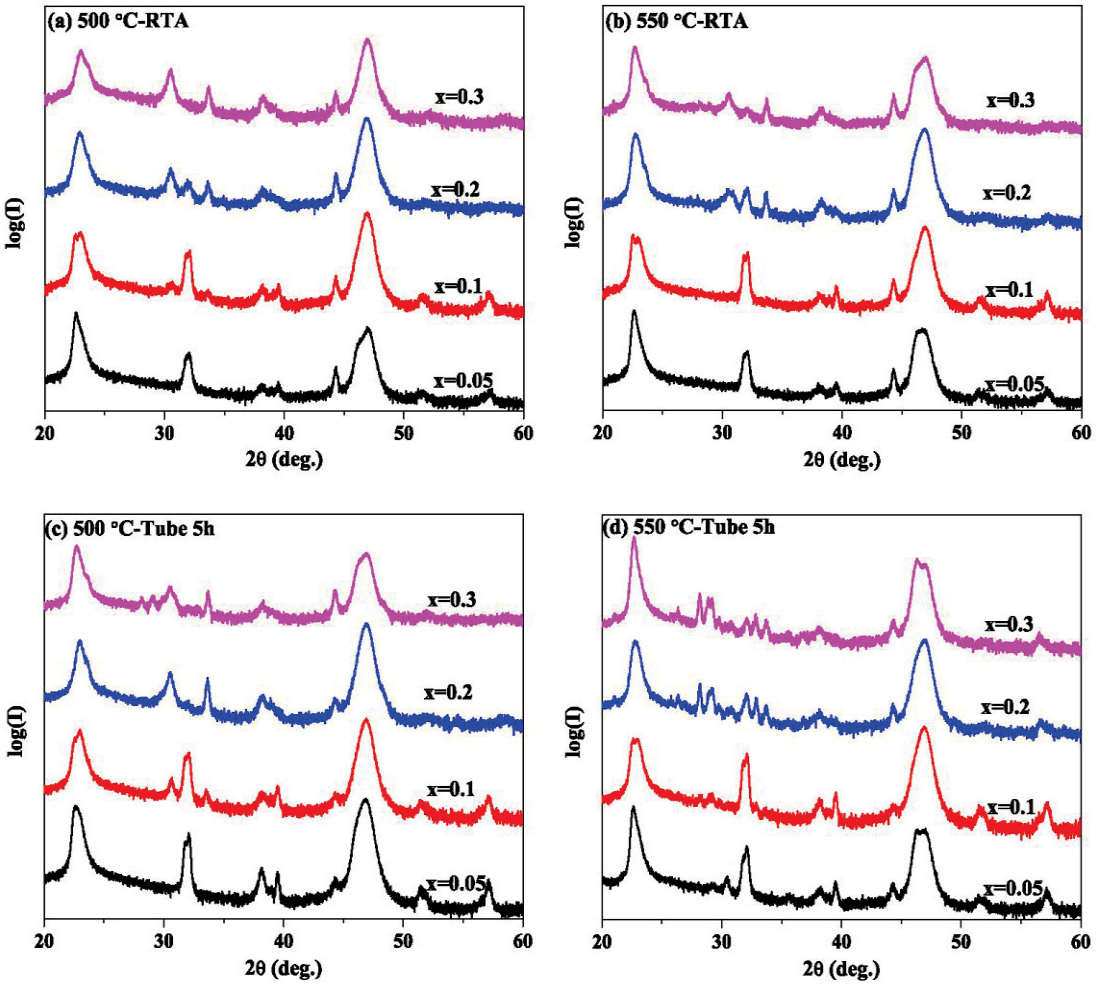

Figure 5.6 XRD patterns of Au/BFGO/LNO/glass substrate annealed at **(a)** 500 ºC and **(b)** 550 ºC by RTA, and **(c)** 500 ºC and **(d)** 550 ºC by normal tube furnace for 5h.

However, extending annealing time by normal furnace tube (Figure 5.6(c)) at 500 ºC, the co-existence region for *R*3*c* and *Cm* phase just appears at x=0.1. When x=0.2, the pure *Cm* phase is shown. The shift of *R*3*c*-*Cm* boundary to low Ga concentration region after long-time annealing arises from the increased strain induced by higher crystallinity after long time annealing, where the phase transition is mainly carried out under stress. In Figure 5.6(b), the 550 ºC- RTA annealed samples shows the similar curves as that of 500 ºC- RTA annealed samples. However, after long time annealing at 550 ºC, the other phase is formed at x≥0.2. It means that at high Ga

concentration, arising from high structure distortion, the BFGO structure is not stable and easy to decomposition at high temperature.

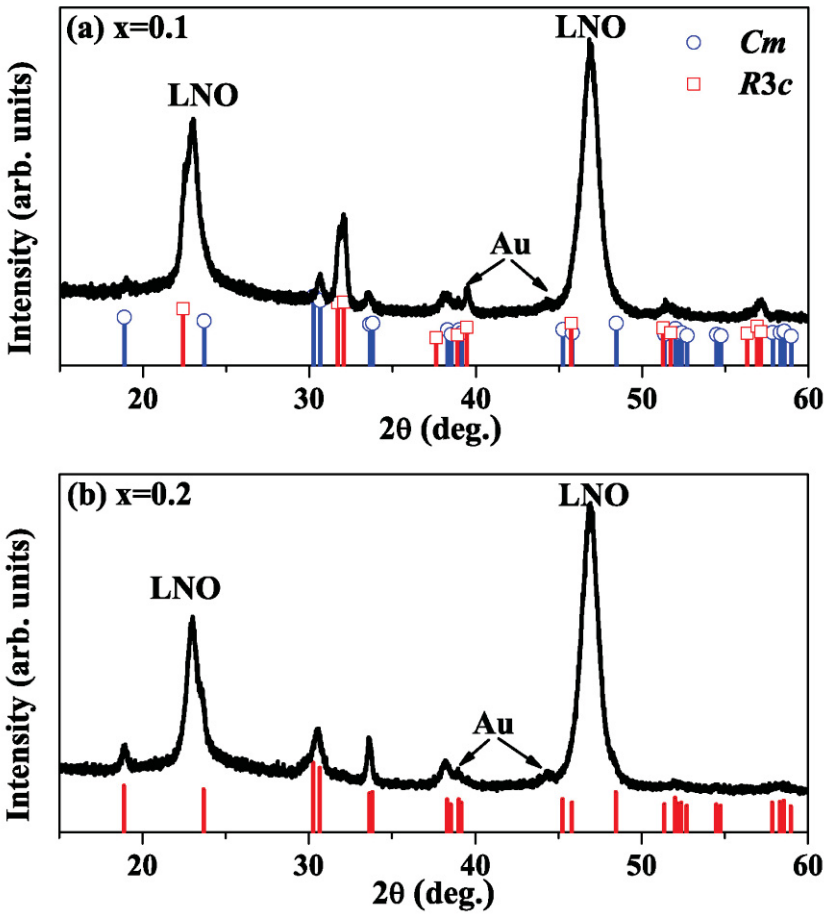

Figure 5.7 Comparison of XRD pattern for 500 ºC-Tube 5h annealed BF1-xGxO/LNO/glass with calculated diffraction data for the *Cm* phase and PCPDF data of *R*3*c* phase BFO, at **(a)** x=0.1 and **(b)** x=0.2.

Figure 5.7 show the comparison between measured XRD spectrum of Tube 5h-500 ºC annealed BFGO and diffraction data of the *Cm* phase calculated for lattice parameters a=0.5325 nm, b=0.5296 nm, c=0.4697 nm and β=91.056 º by using the structural parameters given in the literature. The XRD pattern of BF0.8G0.2O matches perfectly with calculated data of *Cm* phase, while BF0.9G0.1O shows mixture of *R*3*c* and *Cm* phase.

The surface morphologies of 500 ºC-Tube 5h annealed samples are shown in Figure 5.8. It is obvious that at x=0.1 the grain size is uniform and the smallest. The similar phenomenon that *R*3*c*-*Cm* co-existence region keeps smaller grain size is also

observed in BFAO system.

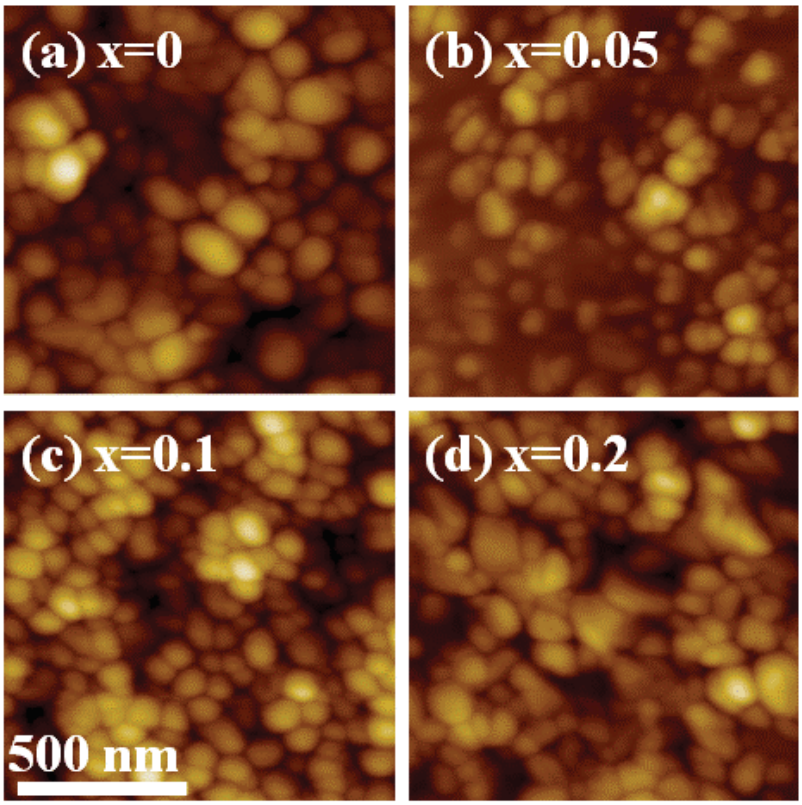

Figure 5.8 AFM images for 500 ºC-Tube 5h annealed BF1-xGxO/LNO/glass with **(a)** x=0, **(b)** x=0.05, **(c)** x=0.1 and **(d)** x=0.2.

Figure 5.9 shows the *J-E* properties of BFGO samples grouped by annealing process. For RTA annealed samples, in Figure 5.9(a) and (b), leakage current decreases with increasing Ga concentration. It confirms our suggestion that Ga-substitution can efficiently decrease leakage current by suppressing formation of Fe^{2+}, the similar as Al-substitution. According to the Pauling electronegativity theory, the higher the difference of electronegativity between two elements is, the stronger the bond energy is. Accordingly, the bonding energy of Ga-O is stronger than that of Bi-O and Fe-O (bonding of Ga^{3+}-O^{2-} is 2.94 eV and Fe^{3+}-O^{2-} is 2.6 eV [9]). Thus the strong chemical bond of Ga-O reduces oxygen vacancies arisen from volatilization of Bi during heat treatment, which will reduce leakage current.

For Tube-5h annealed samples, at x=0.3 in Figure 5.9(c) and x=0.2 and 0.3 in Figure 9(d), samples show unusual high leakage current. It is perhaps due to the

presence of the other phase, which is detected from XRD in Figure 5.6. For the samples which show pure *R*3*c* and/or *Cm* phase follow the tendency that leakage current decreases with increasing Ga concentration.

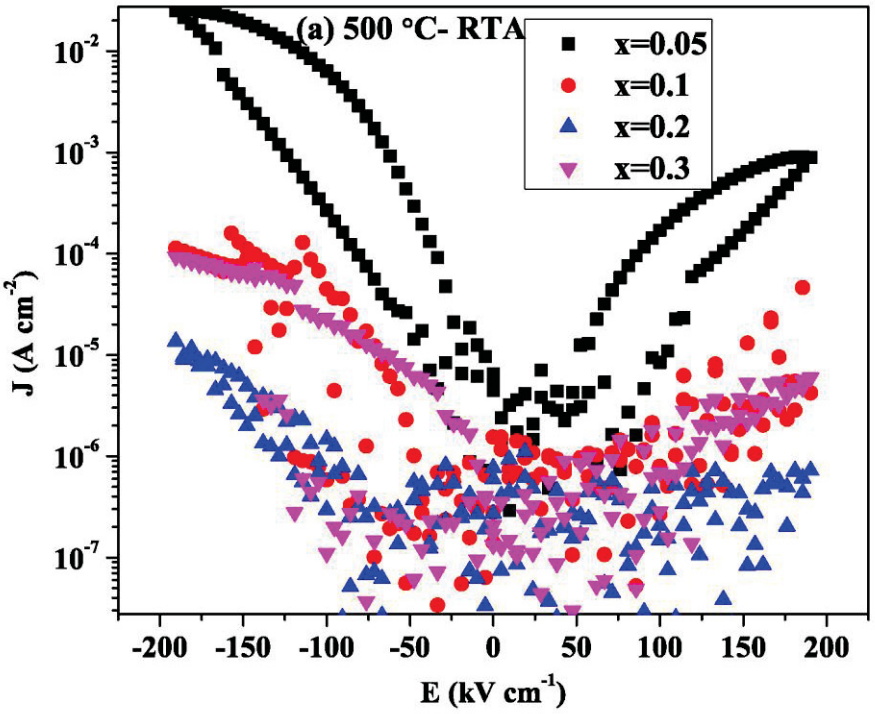

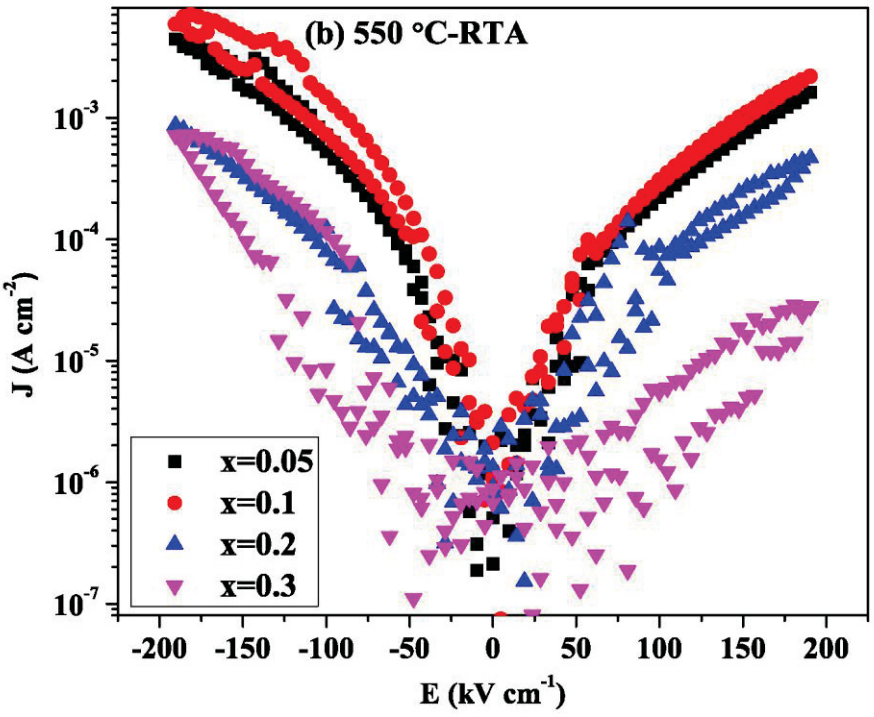

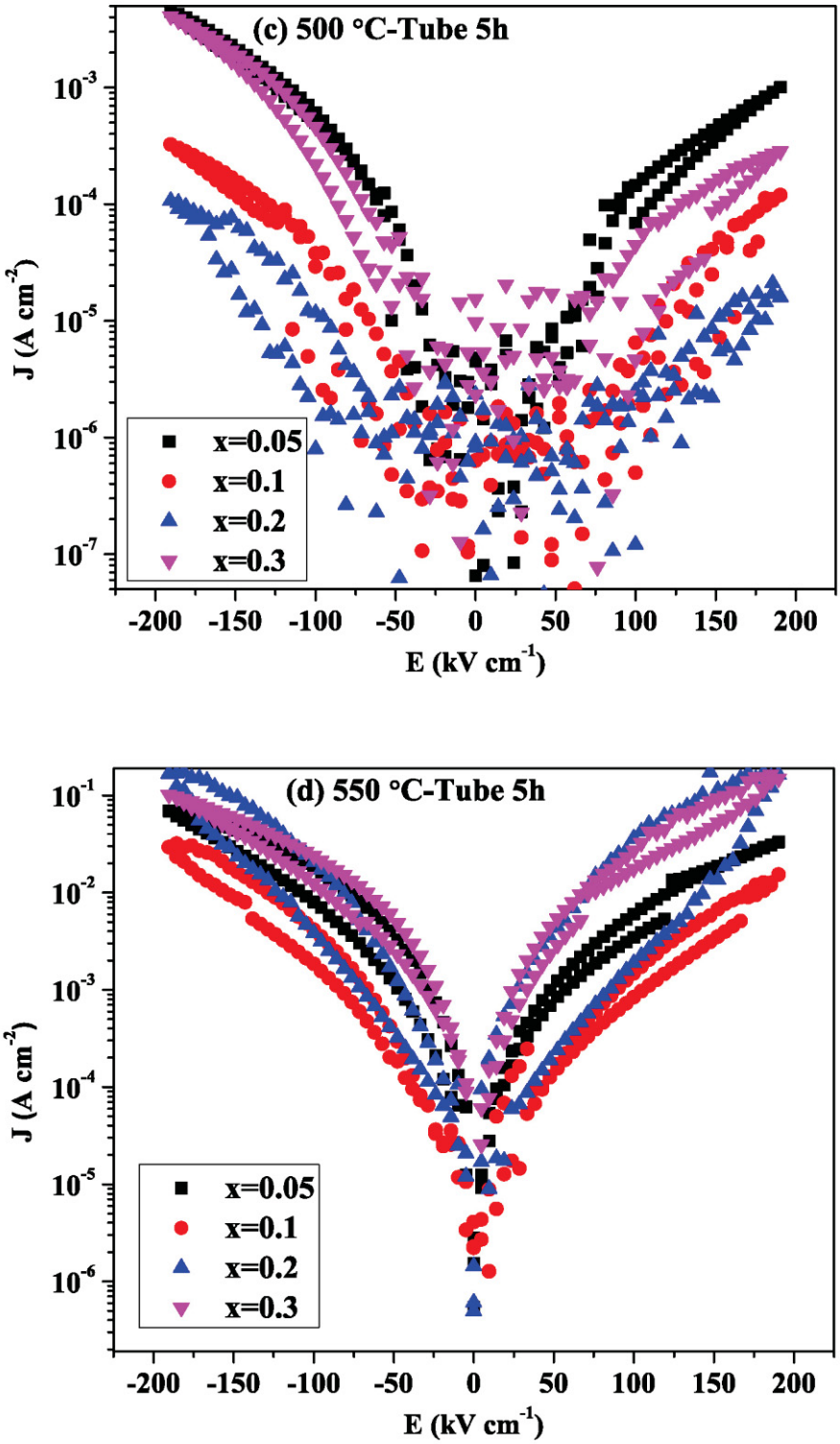

Figure 5.9 *J-E* curves of Au/BFAO/LNO/glass annealed by **(a)** 500 ºC-RTA, **(b)** 550 ºC-RTA, **(c)**500 ºC-Tube 5h, and **(d)** 550 ºC-Tube 5h

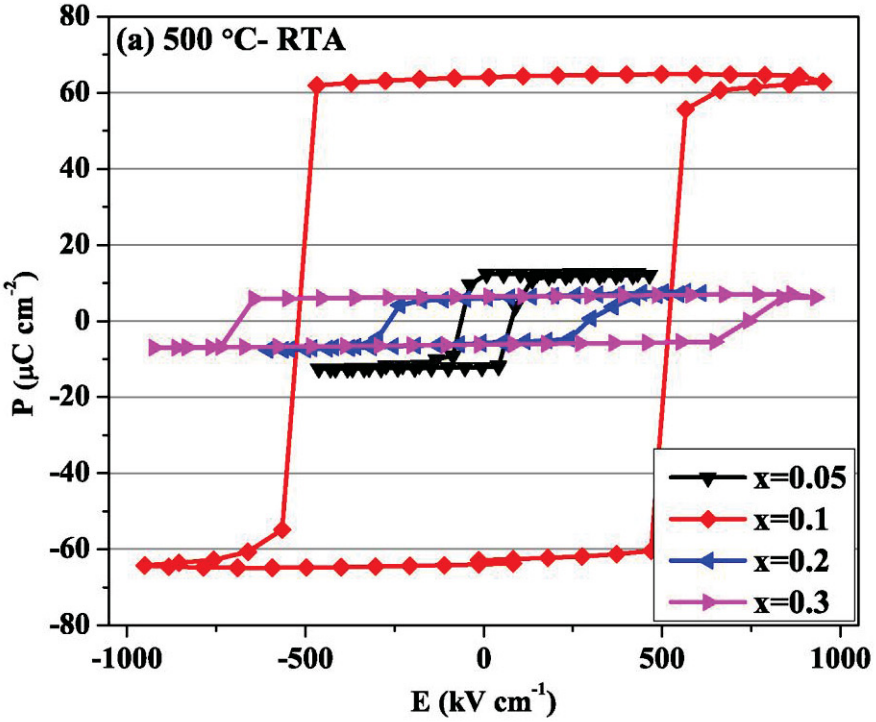
(a) 500 °C- RTA
P (μC cm-2)
E (kV cm-1)
x=0.05
x=0.1
x=0.2
x=0.3

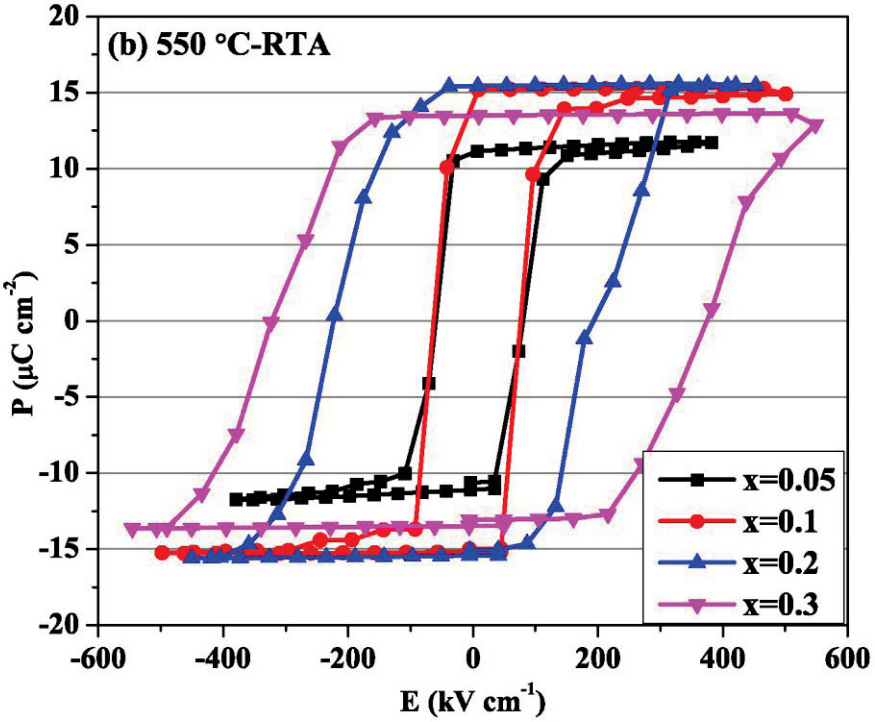
(b) 550 °C-RTA
P (μC cm-2)
E (kV cm-1)
x=0.05
x=0.1
x=0.2
x=0.3

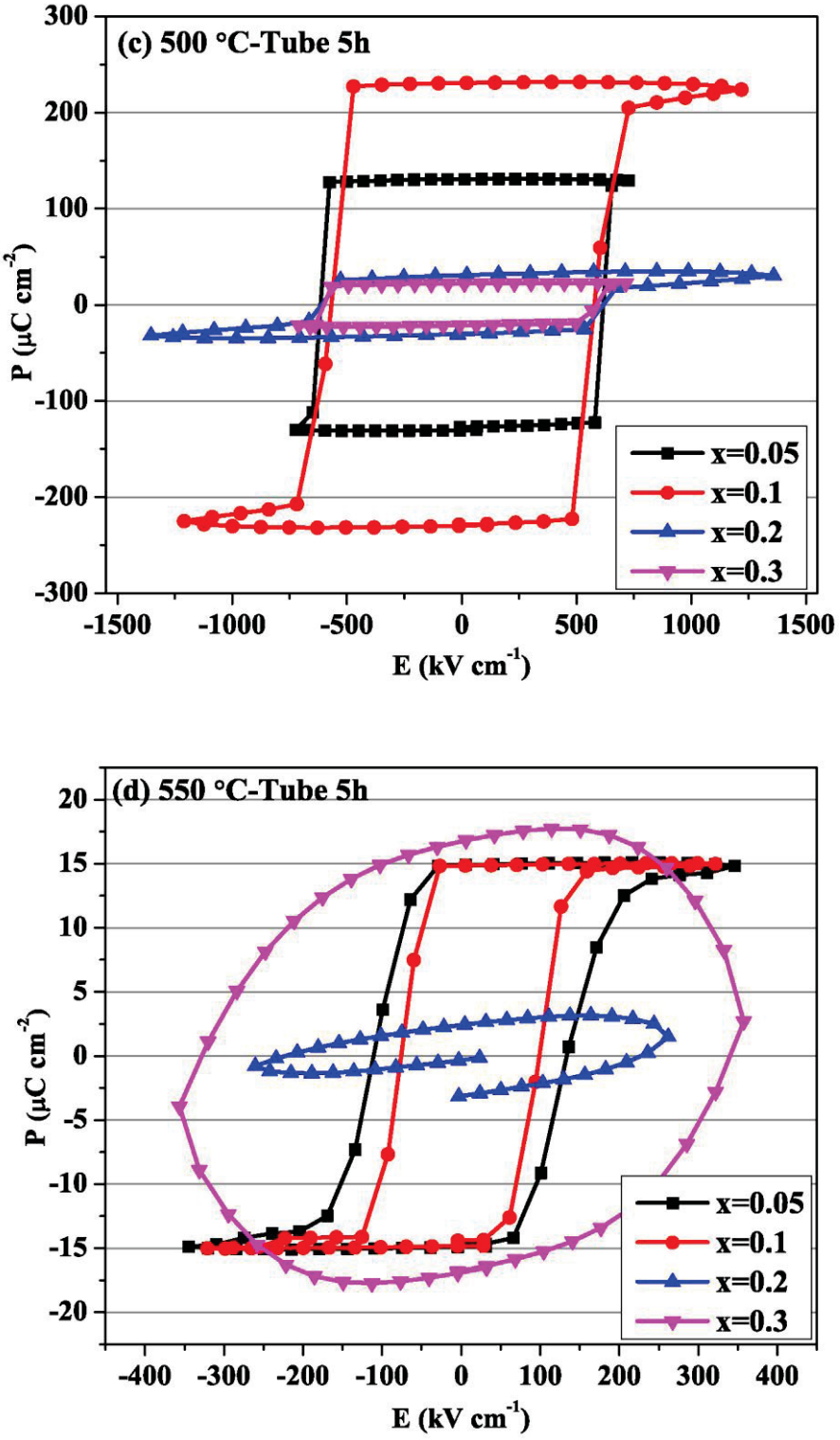

Figure 5.10 *P-E* curves of Au/BFGO/LNO/glass annealed by **(a)** 500 ºC-RTA, **(b)** 550 ºC-RTA, **(c)**500 ºC-Tube 5h, and **(d)** 550 ºC-Tube 5h, measured at room temperature.

The *P-E* hysteresis loops of BFGO grouped by annealing process are shown in Figure 5.10. The 500 ºC- annealed samples keep better polarization behaviour than 550 ºC- annealed samples. The maximum electric field which can be applied on 550 ºC- annealed samples (Figure 5.10(b) and (d)) is around 500 kV cm^{-1}, much smaller than that of the 500 ºC- annealed samples (≥1000 kV cm^{-1}, Figure 5.10(a) and (c)). Moreover, the P_r values of 550 ºC- annealed samples are limited around 15 μC cm^{-2}, which are consistent with the other 550 ºC- annealed samples in our study (i.e. BFO and BFAO). In contrast, the 500 ºC- annealed samples present huge remnant polarization values, an order of magnitude higher than that of 550 ºC- annealed samples. It is surprised that the XRD curves of 500 ºC- and 550 ºC- annealed samples are similar and there is little difference in leakage current, but a huge distance in polarization value is shown. We suggest that it is due to the presence of Bi vacancies coming from evaporation of Bi at high annealing temperature. The presence of vacancies will lead to in-plane strain relaxation, which against the saturated polarization. Moreover, the enhanced polarization after long-time annealing at 500 ºC can be also account for the enhanced crystallinity.

The P_r and E_c values for 500 ºC-Tube 5h annealed samples are listed in Table 5.3. At x=0.1, where *R*3*c* and *Cm* phase co-exist, BF0.9G0.1O keeps the largest P_r value of 230 μC cm^{-2} and the smallest E_c value of 562 kV cm^{-1}.

Table 5.3 P_r and E_c values for BF1-xGxO films (500 ºC-Tube 5h annealed)

x	Detectable phase	P_r (μC cm^{-2})	E_c(kV cm^{-1})
0	*R*3*c*	120	668
0.05	*R*3*c*	130	614
0.1	*R*3*c*+*Cm*	230	562
0.2	*Cm*	30	614
0.3	*Cm*+Impurity	22	614

This value is the highest one ever measured for a ferroelectric and higher than the theoretically predicted values of tetragonal-like $BiFeO_3$ (150 μC cm^{-2}) and *P*4*mm* $BiGaO_3$ (152 μC cm^{-2}). However, the polarization value rapidly decreases to 30 μC cm^{-2} at x=0.2. The pure *Cm* phase shows much smaller P_r value than that of *R*3*c* phase and *R*3*c*-*Cm* mixture. We confirmed that similar results can be obtained with

reproducibility by preparing samples separately using other precursor solutions.

It is interesting that the observed huge polarization has a strong correlation with the coexistence of *R*3*c* and *Cm* phases. $BiFe_{0.9}Ga_{0.1}O_3$ film which exhibits the largest polarization is in the intermediate region for phase transition from *R*3*c* to *Cm* phase, which is a pleomorphic phase boundary (PPB) and similar as morphotropic phase boundary (MPB). As a result of these, we suggest that the lattice instability and the resultant change of polarization switching paths around the PPB between *R*3*c* and *Cm* phase may be responsible for the appearance of the huge polarization. Figure 5.11 shows the spontaneous polarization directions of the rhombohedral (*R*) and monoclinic (M_A and M_B) phases of $BiFeO_3$. It is reported that for single crystalline $BiFeO_3$, the spontaneous polarization is almost independent of in-plane strain. The elastic strain induced by out-of-plane mismatch stress rotates the spontaneous polarization direction. [10] In contrast, in our study, due to the polycrystalline structure, the out-of-plane mismatch stress is too weak to take significant influence on polarization properties. The in-plane tensile stress induced phase transition makes it is possible for the rotation of polarization direction. However, the ongoing detailed study on the correlation between PPB and polarization will be required for clarifying the origin of the observed huge polarization.

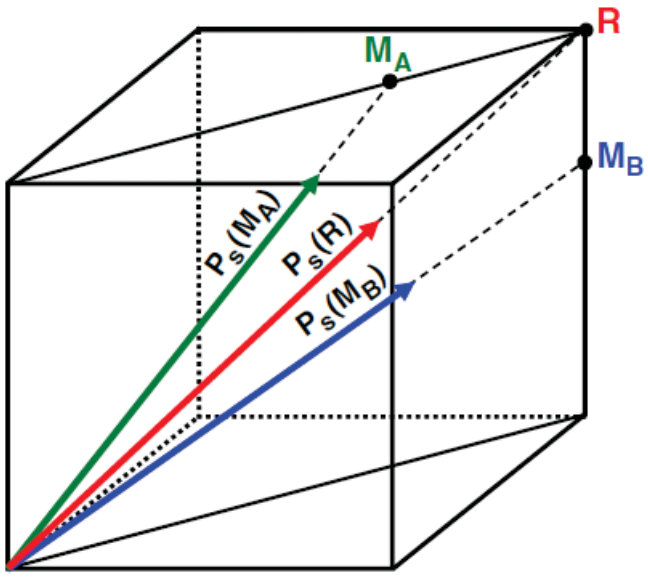

Figure 5.11 The spontaneous polarization directions of the rhombohedral (*R*) and monoclinic (M_A and M_B) phases of $BiFeO_3$.

5.4 Conclusions

$BiFe_{1-x}Ga_xO_3$ thin films with *R*3*c* and *Cm* were simply obtained by the chemical solution deposition (CSD) method. This kind of material was conventionally synthesized only under high-pressure and high-temperature previously. The thin films crystallized in rhombohedral perovskite structure with space group *R*3*c* up to x=0.05 and in tetragonal-like monoclinic structure with space group *Cm* above x=0.2. The coexistence of both phases was observed at x=0.1-0.2. We discover that the film with coexistence of *R*3*c* and *Cm* phases exhibit a huge ferroelectric polarization of 230 μC cm^{-2} after long-time annealing at 500 ºC, which is the highest one ever measured in a ferroelectric. It was suggested that the observed huge polarization arises from the presence of PPB which induces the lattice instability and changes the switching paths of polarization.

References

[1] G. Catalan and J. F. Scott. Physics and applications of bismuth ferrite. Adv. Mater. 21, 2463-2485 (2009).

[2] A. A. Belik, T. Wuernisha, T. Kamiyama, K. Mori, M. Maie, T. Nagai, Y. Matsui, and E. Takayama-Muromachi, High-pressure synthesis, crystal structures, and properties of perovskite-like $BiAlO_3$ and pyroxene-like $BiGaO_3$. Chem. Mater. 18, 133-139 (2006).

[3] A. A. Belik, S. Iikubo, K. Kodama, N. Igawa, S. Shamoto, S. Niitaka, M. Azuma, Y. Shimakawa, M. Takano, F. Izumi, and E. Takayama-Muromachi. Neutron powder diffraction study on the crystal and magnetic structures of $BiCoO_3$. Chem. Mater. 18, 798-803 (2006).

[4] A. A. Belik, S. Y. Stefanovich, B. L. Lazoryak, and E. Takayama-Muromachi. $BiInO_3$: a polar oxide with $GdFeO_3$-type perovskite structure. Chem. Mater. 18, 1964-1968 (2006).

[5] A. A. Belik, D. A. Rusakov, T. Furubayashi, and E. Takayama-Muromachi. $BiGaO_3$-based perovskites: a large family of polar materials. Chem. Mater. 24, 3056-3064 (2012).

[6] P. Baettig, C. F. Schelle, R. LeSar, U. V. Waghmare, and N. A. Spaldin. Theoretical prediction of new high-performance lead-free piezoelectrics. Chem.

Mater. 17, 1376-1380 (2005).

[7] S. K. Singh, H. Ishiwara, and K. Maruyama. Enhanced polarization and reduced leakage current in $BiFeO_3$ thin films fabricated by chemical solution deposition. J. Appl. Phys. 100, 064102 (2006).

[8] P. Hansen, K. Witter, and W. Tolksdorf. Magnetic and magneto-optical properties of bismuth-substituted gadolinium iron garnet films. Phys. Rev. B 27, 4375-4383 (1983).

[9] Z. Hajnal, J. Miró, G. Kiss, F. Réti, P. Deák, R.C. Herndon, and J. M. Kuperberg. Role of oxygen vacancy defect states in the n-type conduction of β-Ga_2O_3. J. Appl. Phys. 86, 3792 (1999).

[10] H. Jiang, S. Baek, D. Ortiz, C. Folkman, R. Das, Y. Chu, P. Shafer, J. Zhang, S. Choudhury, V. Vaithyanathan, Y. Chen, D. Felker, M. Biegalski, M. Rzchowski, X. Pan, D. Schlom, L. Chen, R. Ramesh, and C. Eom. Strain-induced polarization rotation in epitaxial (001) $BiFeO_3$ thin films. Phys. Rev. Lett. 101, 107602 (2008).

Chapter 6

Conclusions

The $BiFeO_3$-based thin films were prepared by simple chemical solution deposition (CSD) method in this study. Based on the research of excess Bi and chemical substitution induced property evolution, we got a clear understanding of the relationship between strain and polarization properties.

In Chapter 2, polycrystalline $BiFeO_3$ thin films with overdosed Bi up to 15 mol% have been prepared. All the films crystallized in *R*3*c* structure after annealing at 550 ºC for 5h by normal furnace. The structure analysis by the out-of-plane and the in-plane XRD showed that the film with 5 mol% excess Bi had the smallest lattice parameters indicative of the low ion vacancies and was strongly strained. Moreover, long-time annealing is benefit for crystallization and building up stress, which will further enhance polarization. The ferroelectric polarization curve of film with 5 mol% excess Bi showed well saturated hysteresis accompanied by the largest saturation polarization of 14.8 μC cm^{-2} after long-time annealing. It was found that the value of saturation polarization is strongly correlated with the crystal deformation induced by in-plane tensile stress. These indicate that the excess Bi greatly influences the *P*-*E* properties of BFO thin films via enhancement of lattice deformation induced by in-plane stress.

$LaNiO_3$ bottom electrodes play an important role in the structure and polarization properties of top BFO films. 650 ºC-annealed LNO layer shows better crystallinity, offering a potential for growing high quality BFO film on it. 500 ºC-Tube 5h annealed B1.1F, which is deposited on 650 ºC-annealed LNO, shows the largest P_r value of 142 μC cm^{-2}, attributed to the high in-plane strain achieved by long-time and low-temperature annealing.

From these two chapters, it is suggested that reduced defects by overdosed Bi or

decreasing annealing temperature, and increased crystallinity by extending annealing time are the efficient methods to enhance in-plane stress, which will further affect the ferroelectric properties of $BiFeO_3$. There is a linear relationship between observed P_r value and in-plane stress induced crystal distortion in our study.

In Chapter 4 and 5, doping of Al and Ga on Fe-site were carried out. $BiFe_{1-x}Al_xO_3$ (BFAO) and $BiFe_{1-x}Ga_xO_3$ (BFGO) thin films were fabricated by CSD method and the phase transition from ground *R*3*c* phase to tetragonally-distorted *Cm* phase was observed in both two systems. In $BiFe_{1-x}Al_xO_3$ system, *R*3*c*, *Cm* and *T* phases appear. The *T* phase is formed under high temperature (900 ºC) and high Al concentration (x=0.2-0.4). While the *Cm* phase is likely to appear in the region of low temperature (500-550 ºC) and high Al concentration (x=0.2-0.4). There is an obvious co-existence region for *R*3*c* and *Cm* phase (x=0.2), while no such region for *T* phase. In $BiFe_{1-x}Ga_xO_3$ system, *R*3*c* and *Cm* are the principle phases, while *T* phase no longer appears. BFGO films crystallize in *R*3*c* phase up to x=0.05 and in *Cm* phase above x=0.2. The coexistence of both phases is observed at x=0.1-0.2. It is found that the polarization can be greatly enhanced around the co-existence region of *R*3*c*-*Cm* phase, with P_r value of 145 μC cm^{-2} for BFAO and 230 μC cm^{-2} for BFGO.

The P_r value of 230 μC cm^{-2} observed in BFGO is the highest value ever been measured in ferroelectric. So far the presence of MPB in PZT-based piezoelectric ceramics is confirmed to be the most important region where very large piezoelectric responds can be obtained. Our results suggest that modification of Fe-site for BFO induces phase instability and provides a possibility for formation of MPB-like region. The appearance of MPB-like region can be achieved at low temperature and normal atmosphere by simple CSD method. It opens a new path to research the lead-free electric devices. Bi is nontoxic in its oxide forms, and $BiFeO_3$-based system is able to be the alternative for PZT-based system.

Symbol List

$R3c$	One of space groups in trigonal crystal system
R	Abbreviation for “Rhombohedral”
$P4mm$	One of space groups in tetragonal crystal system
T	Abbreviation for “Tetragonal”
Cm	One of space groups in monoclinic crystal system
M_A	Space group Cm, with polarization orientation [uuv] ($u<v$)
M_B	Space group Cm, with polarization orientation [uuv] ($u>v$)
M_C	Space group Pm, with polarization orientation [$u0v$]
$Pcca$	One of space groups in orthorhombic crystal system
a, b, c	Lattice constant
α, β	Lattice constant
r	Ionic radius
t	Tolerance factor
P	Polarization
P_s	Spontaneous polarization
P_r	Remnant polarization
$\boldsymbol{E_c}$	Coercive electric field
$\boldsymbol{Tc}$	Curie temperature
d	Interplanar spacing
Δd	Spacing distance between in-plane and out-of-plane, calculated by $\Delta d = (d_{\text{in-plane}} - d_{\text{out-of-plane}})/d_{\text{out-of-plane}}$
J	Current density
E	Applied electric field

Publications

[1] Jingdan Yan, Manabu Gomi, Takeshi Yokota and Huaihe Song. Phase transition and huge ferroelectric polarization observed in $BiFe_{1-x}Ga_xO_3$ thin films. Appl. Phys. Lett.102, 222906 (2013).

[2] Jingdan Yan, Manabu Gomi, Takashi Hattori, Takeshi Yokota and Huaihe Song. Effect of excess Bi on structure and ferroelectric properties of polycrystalline $BiFeO_3$ thin films. Thin Solid Films (Accepted).

[3] Jingdan Yan, Manabu Gomi, Takeshi Yokota and Huaihe Song. Phase transition and enhanced ferroelectric polarization in $BiFe_{1-x}Al_xO_3$ thin films. Phys. Status Solidi-R (Submitted).

[4] Jingdan Yan, Manabu Gomi, Tahashi Hattori, Jing Qiao, and Takeshi Yokota. Phase transition of $BiFe_{1-x}Al_xO_3$ films prepared by chemical solution deposition. J. Jpn. Soc. Powder Powder Metall (ICF11) (Submitted).

[5] Jingdan Yan, Huaihe Song, Huijuan Zhang, Jiayan Yan, Xiaohong Chen, Feng Wang, Huiying Yang, and Manabu Gomi. $Ti_xSn_{1-x}O_3$ solid solution as an anode material in lithium-ion batteries. Electrochim. Acta 72, 186-191 (2012).

Academic Conferences

International Conferences

[1] Jingdan Yan and Manabu Gomi. Chemical solution deposition and photovoltaic properties of $BiFeO_3$ thin films. The 4th International Workshop on Advanced Ceramics (IWAC04), 10-12 December, 2010, Nagoya, Japan.

[2] Jingdan Yan, Manabu Gomi, Takashi Hattori, and Takeshi Yokota. Effect of excess Bi on structure and ferroelectric properties of polycrystalline $BiFeO_3$ thin films. The 2nd International Conference of the Asian Union of Magnetics Societies (ICAUMS 2012), 2-5 October, 2012, Nara, Japan.

[3] Takashi Hattori, Jingdan Yan, Takeshi Yokota, and Manabu Gomi. Sputtered-epitaxy of tetragonal $BiFeO_3$ films on (001) $SrTiO_3$ substrates. The 2nd International Conference of the Asian Union of Magnetics Societies (ICAUMS

2012), 2-5 October, 2012, Nara, Japan.

[4] Jingdan Yan, Manabu Gomi, Tahashi Hattori, Jing Qiao, and Takeshi Yokota. Phase transition of $BiFe_{1-x}Al_xO_3$ films prepared by chemical solution deposition. The 11th International Conference on Ferrites (ICF 11), 15-19 April, 2013, Okinawa, Japan.

Local Conferences

[1] Takashi Hattori, Shindai Hasegawa, Jingdan Yan, Takeshi Yokota, and Manabu Gomi. Sputtered-epitaxy of tetragonal $BiFeO_3$ films and leakage behaviour. Academic Forum on Ceramics Research in Tokai Branch, The Ceramic Society of Japan, 18 December, 2010, Nagoya, Japan.

[2] Jingdan Yan, Manabu Gomi, Kengo Tamiya, and Takeshi Yokota. Contribution of excess Bi on structural and electrical properties of polycrystalline $BiFeO_3$ thin films. Academic Forum on Ceramics Research in Tokai Branch, The Ceramic Society of Japan, 3 December, 2011, Nagoya, Japan.

[3] Takashi Hattori, Goki Ando, Jingdan Yan, Takeshi Yokota, and Manabu Gomi. Sputtered-epitaxy of Mc phase $BiFeO_3$ films on (001) $SrTiO_3$ substrates. Academic Forum on Ceramics Research in Tokai Branch, The Ceramic Society of Japan, 3 December, 2011, Nagoya, Japan.

[4] Kengo Tamiya, Jingdan Yan, Manabu Gomi, and Takeshi Yokota. Photovoltaic and leakage behavior of sputtering $Bi_4Ti_3O_{12}$ thin films on $LaNiO_3$. Academic Forum on Ceramics Research in Tokai Branch, The Ceramic Society of Japan, 3 December, 2011, Nagoya, Japan.

[5] Jingdan Yan, Manabu Gomi, Takashi Hattori, and Takeshi Yokota. Influence of annealing on ferroelectric properties of polycrystalline $BiFeO_3$ thin films. Academic Forum on Ceramics Research in Tokai Branch, The Ceramic Society of Japan, 1 December, 2012, Nagoya, Japan.

[6] J. Qiao, Manabu Gomi, Jingdan Yan, and Takeshi Yokota. Preparation and electrical properties of pure $BiFeO_3$ ceramics by a polymerized complex method. Academic Forum on Ceramics Research in Tokai Branch, The Ceramic Society of Japan, 1 December, 2012, Nagoya, Japan.

[7] Takashi Hattori, Jingdan Yan, Takeshi Yokota, and Manabu Gomi. Preparation and origin of T-$BiFeO_3$ thin films prepared by sputtering method. Academic

Forum on Ceramics Research in Tokai Branch, The Ceramic Society of Japan, 1 December, 2012, Nagoya, Japan.